

Considerations for an In-Process Ultrasonic Phased Array Inspection Method for Narrow Gap Welds

Ewan Nicolson

Department of Electronic and Electrical Engineering

University of Strathclyde

A thesis submitted for the degree of

Doctor of Engineering

April 2024

Copyright

This thesis is the result of the author's original research. It has been composed by the author and has not been previously submitted for examination which has led to the award of a degree.

The copyright of this thesis belongs to the author under the terms of the United Kingdom Copyright Acts as qualified by University of Strathclyde Regulation 3.50. Due acknowledgement must always be made of the use of any material contained in, or derived from, this thesis.

Signed: 

Date: 18/04/2024

Acknowledgements

To my supervisors Charles MacLeod and Ehsan Mohseni, thank you for your continued support and guidance throughout the last three-and-a-half years. The advice, opportunities and flexibility afforded to me throughout the pursuit of this doctorate have been invaluable. I would also like to extend thanks to Dave Lines for his willingness to part with his vast wisdom of ultrasonics, which has been a priceless resource throughout this work.

To all my colleagues – past and present – at the Centre for Ultrasonic Engineering (CUE), thank you for your time and expertise, and for making this such an enjoyable few years.

Furthermore, a huge thanks must go to the multiple supporting organisations that have enabled a close link between this work and industry, through which I haven gained unique insight and experience. I would also like to acknowledge EPSRC for their support of this work, and the FIND-CDT for providing valuable training throughout fulfilment of this doctorate.

To my parents Jane and Don, thank you for instilling in me the work ethic and belief required for this to be possible.

To my fiancée Liv, I am forever grateful for your love, support and remarkable patience. I couldn't have done it without you.

Abstract

The nuclear industry in the UK has seen a resurgence in recent years, joining the race to net-zero energy production through renewable sources. This has led to an increasing demand for the modernisation of manufacturing processes for high-value welded components, such as nuclear pressure vessels and offshore turbine towers.

To ensure the structural integrity of these critical components, Non-Destructive Testing (NDT) is often an essential step in the manufacturing process. Currently, NDT of welds are conducted after the welding process and often off-site, with detected defects requiring rework often resulting in schedule delays. However, by combining the welding and inspection processes at the point of manufacture, flaws may be detected and corrected in situ. This streamlined in-process solution could ensure components are completed on time, while reducing production costs and ensuring a right-first-time product.

Currently, inspection of narrow gap welds is notoriously difficult using traditional ultrasonic phased array methods, which must be addressed before an in-process system can be deployed. This difficulty arises from the vertical nature of Lack-of-Sidewall Fusion (LOSWF) defects in these weld geometries. This work introduces the dual-tandem phased array method, which utilises two phased array probes in a pitch-catch configuration allowing both pulse-echo and through-weld detection. Coupled with Full Matrix Capture (FMC) acquisition and Total Focusing Method (TFM) imaging, it has been shown that vertical notch defects can be detected with high Signal-to-Noise Ratio

(SNR) using this method in a mock-narrow gap weld setup through the use of multi-mode and multi-view imaging.

Additionally, it is shown that this method can be implemented for in-process weld geometries, allowing detection of vertical notch defects in the presence of partial weld geometric reflections. This is achieved through the implementation of adaptive delay law calculation, while imaging using both phase and amplitude based delay-and-sum imaging techniques. This work also proposes an adaptive probe adjustment technique for optimisation of array positioning during in-process inspection.

Furthermore, a data compression technique utilising coded excitation has been developed and demonstrated, allowing single-bit digitisation of ultrasonic data. This has been shown to provide comparable results to standard resolution digitisation when implemented with TFM and Phase Coherence Imaging (PCI) of tip-diffraction from a notch defect, with limited SNR compromise. This has also been demonstrated at low transmit voltages, potentially paving the way for an intrinsically safe and lightweight imaging system. In addition, the ability to acquire single-bit data reduces transfer rates, image processing times and data storage requirements.

The accumulation of this work is intended to provide a path towards the development of an in-process phased array inspection technique for narrow gap welds.

Table of Contents

List of Figures	x
List of Tables	xx
Abbreviations	xxi
1. Introduction.....	1
1.1. Industrial Motivation.....	1
1.2. Research Objectives	7
1.3. Contributions to Knowledge	7
1.4. Thesis Structure.....	8
1.5. Journal Contributions	9
1.6. Conference Contributions.....	10
1.7. Industrial Partnership	12
2. Technical Background.....	14
2.1. Fusion Welding	15
2.1.1. Techniques.....	15
2.1.2. Defects.....	18
2.2. Narrow Gap Welds.....	20
2.2.1. Narrow Gap Welding Techniques.....	21
2.2.2. Advantages of Narrow gap Use.....	22
2.2.3. Disadvantages of Narrow Gap Use	24

2.2.4.	Narrow Gap Applications.....	24
2.3.	Ultrasonic Waves in Solids	25
2.3.1.	Wave Modes.....	26
2.3.2.	Waves at Boundaries	27
2.3.3.	Mechanical Properties	30
2.3.4.	Wave Propagation	34
2.4.	Fundamentals of Ultrasonic Testing.....	35
2.4.1.	Piezoelectric Effect.....	37
2.4.2.	Single Element Ultrasound.....	38
2.4.3.	Time-of-Flight Diffraction	41
2.4.4.	Ultrasonic Phased Array.....	44
2.4.5.	Full Matrix Capture.....	48
2.5.	Advanced Ultrasonic Imaging.....	50
2.5.1.	The Hilbert Transform.....	50
2.5.2.	Amplitude Imaging Methods.....	53
2.5.3.	Phase Imaging Methods	56
2.5.4.	Imaging Modes.....	59
2.5.5.	Delay Law Calculation Techniques	61
2.5.6.	Data Fusion.....	65
2.5.7.	Image Performance Indicators.....	66
2.5.8.	Image Colour Palettes	70
2.5.9.	Imaging GUI.....	71

3. Tandem Phased Array Imaging	75
3.1. Introduction	75
3.2. Experimental Procedure	78
3.2.1. FMC Acquisition.....	80
3.2.2. Mode Selection.....	82
3.2.3. ToF Mapping.....	83
3.2.4. TFM Algorithm	84
3.2.5. Image Mixing	85
3.2.6. Image Sensitivity Calculations.....	88
3.3. Test Samples.....	89
3.4. Probe Centre Separation.....	91
3.4.1. PCS Study.....	92
3.4.2. PCS Error Study	93
3.5. Imaging.....	96
3.5.1. Shear Inspection	96
3.5.2. Pulse-Echo.....	97
3.5.3. Through-Transmission	102
3.5.4. Image Mixing	103
3.6. Further Discussion.....	105
3.6.1. Relative Amplitude.....	105
3.6.2. Notch Sizing.....	108
3.7. Conclusions	112

4. In-Process Narrow Gap Inspection	113
4.1. Introduction	113
4.2. Experimental Procedure	117
4.2.1. FMC Acquisition.....	117
4.2.2. Time of Flight Calculation	118
4.2.3. Imaging.....	120
4.2.4. Data Fusion.....	120
4.3. Test Samples.....	121
4.4. Adaptive PCS	124
4.5. Imaging.....	129
4.5.1. Partial-Weld Imaging	130
4.5.2. Weld Geometry Reflections	133
4.5.3. Mode-Converted Diffraction.....	135
4.6. Conclusion.....	136
5. Single-Bit Coded Excitation for Lightweight Ultrasonic Imaging	138
5.1. Introduction	138
5.2. Coded Excitation	142
5.3. Experimental Procedure	146
5.4. Pulse Compression	149
5.5. Compression SNR Analysis	150
5.6. Imaging.....	155
5.6.1. PCI Imaging	155

5.6.2. TFM Imaging	157
5.6.3. Low Voltage Excitation.....	159
5.7. Conclusion.....	164
6. Summary.....	167
6.1. Conclusions	167
6.2. Suggestions for Future Work	170
6.2.1. Imaging Performance	170
6.2.2. Imaging Efficiency	172
6.2.3. Mechanical Deployment.....	174
6.3. Final Summary	178
7. Appendix A	180
8. Appendix B	182
9. References	186

List of Figures

Figure 1.1: Construction underway of Hinkley Point-C nuclear facility [14]2

Figure 1.2: Initial Rolls-Royce SMR plans for 470MW capacity modular power station [17]3

Figure 2.1: Polysoude TIG torch and weld [39] 17

Figure 2.2: SAW welding, with weld torch surrounded by granular flux [42]..... 18

Figure 2.3: Examples of weld defects.20

Figure 2.4: Narrow gap weld geometry21

Figure 2.5: Approximation of weld area for V- and J-groove welds22

Figure 2.6: Thickness vs. weld area for a typical V-groove angle of 37.5° and a narrow groove angle of 1.5° . Left-hand graph shows zoomed-in view of right graph at low thicknesses to show crossover point.....23

Figure 2.7: Narrow gap pipe girth weld and Polysoude TIG torch [62]25

Figure 2.8: Longitudinal and shear wave mode visualised in MATLAB by displacement of uniform 2D crystal lattice27

Figure 2.9: Transmitted and reflected energy based on impedance mismatch28

Figure 2.10: Refraction of sound through water-steel boundary, with first (blue) and second (red) critical angles indicated30

Figure 2.11: Young’s modulus.....32

Figure 2.12: Shear modulus33

Figure 2.13: Poisson’s Ratio33

Figure 2.14: Single element ultrasonic inspection with (a) no defect, (b) small defect and (c) large defect	40
Figure 2.15: Theoretical A-Scans obtained from inspections scenarios shown in Figure 2.14 for (a) no defect, (b) small defect and (c) large defect	40
Figure 2.16: Orbital TOFD scanner [112].....	41
Figure 2.17: TOFD setup for crack (outlined in red) inspection, showing paths of lateral wave (i), top (ii) and bottom (iii) tip diffraction and backwall (iv) reflection	42
Figure 2.18: Typical TOFD scan, showing tip diffraction responses of bulk crack between lateral wave and backwall.....	43
Figure 2.19: Linear phased array indicating common parameters of element pitch p , width l_x , length l_y and gap Δx	45
Figure 2.20: Beamforming capabilities of the ultrasonic phased array	46
Figure 2.21: Examples of a (a) linear and (b) sector scan.....	48
Figure 2.22: Data matrix obtained through FMC acquisition, with each element A describing a time signal for transmit element i and receive element j	50
Figure 2.23: (a) real, (b) imaginary components and (c) envelope of signal after calculation of Hilbert transform	52
Figure 2.24: TFM imaging (a) without and (b) with the Hilbert transform	53
Figure 2.25: Full aperture focusing of TFM algorithm on a discretised image region.....	54

Figure 2.26: Visualisation of Gaussian pulse based on (a) amplitude, (b) phase and (c) sign.....	58
Figure 2.27: Wave path considerations and terminology	60
Figure 2.28: Wave mode visualisation.....	61
Figure 2.29: Pythagorean method for delay law calculation.....	62
Figure 2.30: ToF calculation through multiple non-planar surfaces with irregular geometry.....	64
Figure 2.31: ToF calculation through changing material properties (note that effects are exaggerated).....	65
Figure 2.32: Noise (red) and signal (blue) regions considered for calculation of SNR.....	67
Figure 2.33: API Values of two 3.0 mm SDH at 35.0 mm (left) and 65.0 mm (right).....	68
Figure 2.34: TFM amplitude fidelity for increasing pixel density.....	70
Figure 2.35: Amplitude and phase colour maps.....	70
Figure 2.36: MATLAB GUI interface showing tool tabs on the right hand side, three-dimensional ultrasonic setup window on the left, and FMC data visualisation along the bottom	72
Figure 2.37: GUI showing TFM image of SDH in standard calibration block using half-matrix capture from data obtained using an Olympus 55SW wedge and 5 MHz probe	73
Figure 3.1: Dual-tandem phased array configuration	77

Figure 3.2: Shear and longitudinal refraction angles at a Rexolite-Steel boundary as a function of incident angle	79
Figure 3.3: Longitudinal and shear refraction angles using 20° Rexolite wedge into steel	79
Figure 3.4: Full matrix obtained from dual tandem FMC, showing four unique views	81
Figure 3.5: Shear self tandem (TT-T) mode, showing skip off backwall on transmission and direct reception.....	83
Figure 3.6: Demonstration of incoherent reflections from each LL-T pulse-echo view in sample NG2. This image is created by summing the left and right pulse-echo views, resulting in reflections from each side of the notch being visible.	87
Figure 3.7: EDM notches in carbon steel samples	90
Figure 3.8: Sample NG2 with dual-array setup, showing EDM notch position	91
Figure 3.9: PCS sensitivity study results for pulse-echo (left), pulse-echo (right) and through transmission	93
Figure 3.10: PCS values used to study PCS error.....	94
Figure 3.11: PCS error effect on pulse-echo image sensitivity applied to 314 mm PCS.....	95
Figure 3.12: PCS error mean-view sensitivity study for L-L through-transmission images	95

Figure 3.13: TFM images of mock narrow-groove samples using self-tandem shear (TT-T) pulse-echo inspection with a shear-transmission optimised wedge.97

Figure 3.14: Sample NG1, 27.5 mm notch depth multi-mode pulse-echo TFM99

Figure 3.15: Sample NG2, 60 mm notch depth multi-mode pulse-echo TFM 100

Figure 3.16: Sample NG3, 92.5 mm notch depth multi-mode pulse-echo TFM 101

Figure 3.17: Narrow-groove sample imaged at 314 mm PCS in through-transmission with mode L-L for samples (left) NG1, (middle) NG2 & (right) NG3..... 103

Figure 3.18: Image mixing in mock narrow gap samples (a) NG1, (b) NG2, and (c) NG3 using diffraction modes L-L, and reflection modes LL-L, LL-T & TT-T 104

Figure 3.19: Relative amplitude study of mock narrow-groove pulse-echo TFM images. Amplitudes are normalised to the maximum amplitude (NG3 left pulse-echo), with maximum image and defect amplitudes shown. Left pulse-echo views are noted by ‘L’ and right pulse-echo views by ‘R’ 106

Figure 3.20: Relative amplitude study of mock narrow-groove L-L TFM images. Amplitudes are normalised to the maximum amplitude (NG3 left pulse-echo TT-T), with maximum image and defect amplitudes shown..... 108

Figure 3.21: Pulse-Echo sizing of notches in each mock narrow-groove sample. Peak-to-peak sizing method used for tip-diffraction indications, and 6 dB drop method for reflections..... 110

Figure 3.22: Through-Transmission sizing of notches in each mock narrow-groove sample using peak-to-peak sizing method using L-L mode 111

Figure 4.1: Rework required for a hot-pass defect detected with traditional cold inspection post-welding (left) and in-process inspection (right)..... 114

Figure 4.2: Example of ToF compensation for a partial weld geometry, for pulse-echo L-L mode (a) compensated and (b) uncompensated for geometry, and for pulse-echo TT-T mode (c) compensated and (d) uncompensated for weld geometry 119

Figure 4.3: Partially filled weld samples with weld fill of 104.0 mm, 70.0 mm and 37.5 mm..... 122

Figure 4.4: EDM notch position and through-thickness depth in mock partial narrow gap samples..... 122

Figure 4.5: Sample PNG4 with dual-array setup, highlighting simulated 70.0 mm weld fill height and 65.0 mm EDM notch height..... 124

Figure 4.6: 1/3 filled weld longitudinal beam crossing for PCS calculations on sample PNG5 125

Figure 4.7: Defect response amplitude and phase coherence for L-L and TL-T modes in PNG2 mixed image 127

Figure 4.8: Defect response amplitude and phase coherence for L-L and TT-T modes in PNG4 mixed image 127

Figure 4.9: Defect response amplitude and phase coherence for L-L and TT-T modes in PNG6 mixed image 127

Figure 4.10: Coupling variation analysis using backwall signal of T-T mode for each PCS in each sample.....	128
Figure 4.11: 1/3 weld fill PCS definition for varying plate thicknesses and fill heights	129
Figure 4.12: Mixed TFM and PCI images of simulated LOSWF in mock partial narrow-groove samples using 1/3 weld fill PCS definition	132
Figure 4.13: Diffractive response amplitude from the weld geometry and notch tips in each mock partial narrow gap sample	134
Figure 4.14: Exaggerated weld cap of partially filled geometry.....	134
Figure 4.15: Pitch-catch TFM images for sample PNG4 using mode (a) L-L, (b) L-T and (c) T-L	136
Figure 5.1: Example of 4 cycle complimentary Golay pair	143
Figure 5.2: Demonstration of sidelobe suppression by the sum of two complimentary Golay functions, resulting in a single main lobe.....	144
Figure 5.3: Experimental setup for data collection, showing the offset of a phased array probe from a rectangular notch (left) and beam profile when the full aperture is focused at the notch centre (right).....	148
Figure 5.4: Demonstration of pulse compression using 12-bit (left) and single-bit (right) receiver quantisation and receive signals from the same dataset. The raw signal is shown in grey, with the resulting compressed A-Scan highlighted in black.....	150
Figure 5.5: SNR Analysis of backwall indication utilising 12-bit and 1-bit receiver quantisation data with 100% duty cycle.....	152

Figure 5.6: SNR Analysis of backwall indication utilising 12-bit and 1-bit receiver quantisation data with 71% duty cycle.....154

Figure 5.7: PCI images processed from single cycle and 16-cycle Golay FMC datasets with 80 V excitation and 48 dB gain. Images from single-cycle 12-bit data (left), 16-cycle 12-bit data (middle) and 16-cycle 1-bit data (right) are shown. The SNR, API, Tx voltage and Rx gain are presented for each image.157

Figure 5.8: TFM images processed from single cycle and 16-cycle Golay FMC datasets with 80 V excitation and 48 dB gain. Images from single-cycle 12-bit data (left), 16-cycle 12-bit data (middle) and 16-cycle 1-bit data (right) are shown. The SNR, API, Tx voltage and Rx gain are presented for each image.159

Figure 5.9: PCI images processed from single cycle and 16-cycle Golay FMC datasets with 10 V excitation and 66 dB gain. Images from single-cycle 12-bit data (left), 16-cycle 12-bit data (middle) and 16-cycle 1-bit data (right) are shown. The SNR, API, Tx voltage and Rx gain are presented for each image.160

Figure 5.10: TFM images processed from single cycle and 16-cycle Golay FMC datasets with 10 V excitation and 66 dB gain. Images from single-cycle 12-bit data (left), 16-cycle 12-bit data (middle) and 16-cycle 1-bit data (right) are shown. The SNR, API, Tx voltage and Rx gain are presented for each image.162

Figure 5.11: SNR Analysis of notch indication in TFM image utilising 12-bit and 1-bit receiver quantisation. This is demonstrated for TFM (top) and PCI(bottom) for both high and low input voltages. 163

Figure 6.1: Example of a C-Scan of a narrow-groove weld, showing defective areas detected using TFM imaging 173

Figure 6.2: Example of a 3D model of a narrow-groove weld, showing defective areas detected using TFM imaging with an amplitude >-6dB 174

Figure 6.3: Tandem phased array setup on a narrow gap weld using two robotic manipulators with dry-coupled high-temperature roller probes..... 176

Figure 6.4: Tandem phased array setup on a narrow gap weld showing force-torque sensors used to ensure consistent coupling during scanning 177

Figure 6.5: Comparison of sector scan image and LL-T TFM image of LOSWF in narrow gap weld using dry-coupled roller probe. 178

Figure 7.1: Zoomed in TFM images in Section 3.5.2, of sample NG1..... 180

Figure 7.2: Zoomed in TFM images in Section 3.5.2, of sample NG2..... 181

Figure 7.3: Zoomed in TFM images in Section 3.5.2, of sample NG3..... 181

Figure 8.1: TFM images from right array transmission only, used to generate mixed images of sample PNG1 in Section 4.5.1..... 182

Figure 8.2: PCI images from right array transmission only, used to generate mixed images of sample PNG1 in Section 4.5.1..... 183

Figure 8.3: TFM images from right array transmission only, used to generate mixed images of sample PNG2 in Section 4.5.1..... 183

Figure 8.4: PCI images from right array transmission only, used to generate
mixed images of sample PNG2 in Section 4.5.1.....184

Figure 8.5: TFM images from right array transmission only, used to generate
mixed images of sample PNG3 in Section 4.5.1.....184

Figure 8.6: PCI images from right array transmission only, used to generate
mixed images of sample PNG3 in Section 4.5.1.....185

List of Tables

Table 3.1: FMC acquisition parameters	82
Table 3.2: Element numbers for each dual-tandem view.....	85
Table 3.3: Carbon steel samples defect positioning.....	90
Table 3.4: Summary of pulse-echo image sensitivity for mock narrow-groove samples	102
Table 4.1: Sample labels and geometry	123
Table 4.2: Summary of mixed images from each notch sample	130
Table 5.1: Quantification of data size reduction using single-bit processing	155
Table 5.2: Quantitative performance of PCI & TFM imaging	163

Abbreviations

ADC	Analogue-to-Digital Converter
AF	Amplitude Fidelity
AIM	Acoustic Influence Map
API	Array Performance Indicator
CFRP	Carbon Fibre Reinforced Polymer
CPU	Central Processing Unit
CUDA	Compute Unified Device Architecture
DAFMC	Dual-Aperture Full Matrix Capture
DC	Direct Current
EB	Electron Beam
EDF	Électricité de France
EDM	Electrical Discharge Machining
FMC	Full Matrix Capture
FMM	Fast Marching Method
FPGA	Field-Programmable Gate Array
FSW	Friction Stir Welding
GMAW	Gas Metal Arc Welding
GPU	Graphical Processing Unit
GTA	Gas Tungsten Arc
GTAW	Gas Tungsten Arc Welding
GUI	Graphical User Interface
HAZ	Heat Affected Zone
HDF5	Hierarchical Data Format version 5
HIC	Hydrogen Induced Cracking
HTHA	High-Temperature Hydrogen Attack
HVM	High-Value Manufacturing
IC	Integrated Circuit
LFW	Linear Friction Welding
LOIRF	Lack-of-Inter Run Fusion
LOSWF	Lack-of-Side Wall Fusion
LW	Longitudinal Wave
MFMC	Multi-Frame Matrix Capture
MIG	Metal Inert Gas
MSFMM	Multi-Stencils Fast Marching Method
NDE	Non-Destructive Evaluation
NDT	Non-Destructive Testing

PA-TOFD	Phased Array Time Of Flight Diffraction
PAUT	Phased Array Ultrasonic Testing
PCF	Phase Coherence Factor
PCI	Phase Coherence Imaging
PCS	Probe-Centre Spacing
PNG	Portable Network Graphic
PRF	Pulse Repetition Frequency
PSF	Point Spread Function
PWI	Plane Wave Imaging
PZT	Lead Zirconate Titanate
RFW	Rotary Friction Welding
RMS	Root-Mean-Squared
RoHS	Restriction of Hazardous Substances
SAFT	Synthetic Aperture Focusing Technique
SAW	Submerged-Arc Welding
SCF	Sign Coherence Factor
SDH	Side-Drilled Hole
SMR	Small Modular Reactor
SNR	Signal-to-Noise Ratio
TFM	Total Focusing Method
TIG	Tungsten Inert Gas
TOF	Time Of Flight
TOFD	Time Of Flight Diffraction
TRL	Transmit-Receive Longitudinal
TVG	Time-Varying Gain
VCF	Vector Coherence Factor
VSA	Virtual Source Aperture
VTFM	Vector Total Focusing Method
WAAM	Wire-Arc Additive Manufacturing
WPS	Weld Procedure Specification

Chapter 1

Introduction

1.1. Industrial Motivation

With increasing pressure to accelerate initiatives to tackle climate change, a radical transformation of the UK energy sector is underway. This revolution seeks to develop and implement a UK wide net zero emission infrastructure by 2050 [1]. With the objective to phase-out fossil fuel energy production over the coming decades, low-carbon generation alternatives such as wind, solar, hydro and nuclear have been proposed as solutions to meet growing energy demands [2]. This transformation is well underway in the UK, with the majority of electricity generation coming from low-carbon sources in 2022 [3], with ambitious plans to remove all fossil fuel energy dependency by 2035 [4].

However, despite zero-emission initiatives being adopted by countries globally, nuclear energy consumption has consistently declined across Europe and North America in the last decade - despite accounting for the majority of the world's generation [5]. In the UK, nuclear energy contributes to 15% of the national electricity supply according to a December 2022 government report [6], in contrast to nearly 30% in 1995 [7].

Additionally, the decommissioning of reactor sites Hunterston-B, Hinkley Point-B and Dungeness-B within the last few years has reduced the current UK nuclear infrastructure to nine active reactors across five sites [8]. Nonetheless, the decommissioning of end-of-life reactors is touted as part of the UK government's plan to triple nuclear energy capacity to 24 GW by 2050, in line with their net-zero policy [9]. This involves the commissioning of new power stations Hinkley Point-C and Sizewell-C [10, 11], with proposals for several Small Modular Reactor (SMR) projects in the future [12]. These will be the first reactors built in the UK for nearly 30 years, since construction of Sizewell-B was completed in 1995 [13].



Figure 1.1: Construction underway of Hinkley Point-C nuclear facility [14]

Despite the recent announcements of planned reactor builds, a 2023 House of Commons committee report has recommended that the UK must further accelerate the transition to low-carbon power alternatives to reach their 2035 target - maximising investment in nuclear and offshore wind sources [15]. Additionally, the UK run SMR competition to

accelerate the development of cutting-edge nuclear technologies is underway, with the ambition of delivering the first operational SMRs by the mid 2030s [16]. With this renewed demand for new and clean power generation infrastructure, a new golden age of nuclear energy generation in the UK has begun.



Figure 1.2: Initial Rolls-Royce SMR plans for 470MW capacity modular power station [17]

With this mandate for expanding nuclear power infrastructure, comes a similar demand for High Value Manufacturing (HVM) processes. Particularly when considering the abundance of heavy gauge steel components required for nuclear and offshore wind power generation, manufacturing that is consistent, reliable and efficient is crucial. This has aligned with the rise of the fourth industrial revolution, commonly termed “Industry 4.0” [18], which has seen a growing preference of digitisation and sensor driven automation over traditional manufacturing processes [19].

One such process that has been targeted for automation is welding, particularly for use in HVM environments. Welding automation utilising robotic manipulators has already accelerated manufacturing on an industrial scale, with the global robotic welding market valued at \$6 billion in 2022, and expected to reach \$30 billion by 2030 [20]. Improving

the accuracy repeatability of welding practices relative to traditional manual welding, the use of automated robotics has a very real potential to revolutionise HVM industries.

A further advantage of welding automation, and one that forms the basis for the work in this thesis, is the opportunity to perform weld integrity checks during manufacture. Non-destructive testing (NDT) is an essential step in heavy manufacturing welding processes to ensure that weld quality is compliant with both internal and regulatory standards. With projections estimating that the global NDT market will exceed \$34 billion by 2030 [21], rising from \$5.6 billion in 2012 [22], it is clear that the NDT is a rapidly growing industry, ripe for innovation.

There are numerous inspection and monitoring methods employed under the umbrella of NDT. This includes the use of eddy current, ultrasound, visual testing, liquid penetrant testing, radiography and magnetic particle testing, with only radiography and ultrasound allow the volume of a component to be tested. Ultrasound is often the most practical volumetric inspection tool, as radiography requires strict control of radiation sources and contained inspection environments.

Flaws generated during welding can be detected before leaving the manufacturing environment thanks to ultrasonic sensors. If exceeding a defined size or volume, these may require the component to be rewelded to remove a flaw. If left undetected, stresses experienced over a component's lifetime can lead to flaw growth, reducing the components effectiveness and sometimes leading to catastrophic failure. In most heavy manufacturing industries, NDT is periodically performed throughout the component's lifetime to monitor known and new flaws, ensuring continued assurance of weld quality.

However, ultrasonic weld inspection standards [23, 24] have typically insisted that inspection occurs post-weld, such that the welding and inspection processes are entirely separate. This is often done manually by skilled NDT technicians, who report flaw indications based on outlined acceptance criteria. This requires the part to have completely cooled, which in the case of large components can take days, to ensure cooling defects such as Hydrogen Induced Cracking (HIC) have time to form. Detected defects which require repair can derail production timelines if extensive rework or scrapping of the component is required. Additionally, this can necessitate the excavation of large volumes of the weld, and require reheating of components to perform repairs.

With the emergence of Industry 4.0, the weld inspection process is one which could benefit from a sensor-driven approach. By replacing the separate linear process of welding and inspection with an automated in-process inspection technique, weld flaws could be detected in real-time during deposition. This would enable the possibility to halt the welding process to repair flaws as they occur, ensuring that components are defect-free at the point of completion. Ultimately, this could enable a right-first-time approach to welding in heavy manufacturing industries.

There are a number of advantages to implementing this process change, the greatest and most obvious being schedule certainty, as there would be reduced rework and disruption to the welding process. In turn, this further knock-on effects to wider infrastructure projects due to delayed parts could be mitigated. Furthermore, repairing flaws during initial welding removes the requirement for cyclical heating processes, reducing

component stresses and limiting energy input. This would help contribute to efficient, reliable production lines with conservative energy and consumable usage.

The use of a robotic inspection system would be required due to proximity to the weld, which in itself provides its own advantages. The capture of consistent spatially encoded data could be invaluable by allowing future revision and processing of data. Additionally new insight could be gained into welding process performance over time, allowing for an ultrasonic sensor-driven process monitoring system, or training of statistical and machine learning models. Furthermore, three-dimensional models and digital twins could be developed to provide further interpretable insight into welding performances in an intuitive format.

Such an in-process approach would be particularly beneficial for large gauge welding processes. These are typically prepared with narrow bevels, hence termed ‘narrow gap’ welds. This type of welding is commonly chosen for the joining of thick-section components due to structural benefits and a reduction in welding volume. These welds are seen in abundance throughout the nuclear energy sector for high-integrity critical components in reactor pressure vessels, as well in offshore wind turbines, shipbuilding and oil & gas platforms.

By detecting potential defects early in the welding process, components can be repaired with little disruption. Particularly within large modular infrastructure projects such as reactor builds, an in-process inspection technique could help to ensure project timelines remain deliverable. Coupled with the growing demand for heavy nuclear components, an in-process narrow gap welding technique could provide significant reductions to lead-

times and overall production costs, and contribute to the acceleration of the nuclear and wider carbon-free energy industry in the UK.

1.2. Research Objectives

Narrow gap welding is notoriously difficult to inspect using standard ultrasonic and phased array techniques. Several challenges must be considered to implement a reliable in-process inspection technique. The objectives of this research are outlined as follows:

- Investigate methods for improving ultrasonic inspection performance in thick section narrow-groove welds.
- Develop an ultrasonic phased array inspection technique capable of detecting and imaging Lack-of-Sidewall Fusion (LOSWF) defects in narrow gap welds.
- Design imaging techniques capable of characterising and sizing LOSWF defects in narrow gap welds.
- Consider geometric effects of partial narrow gap weld geometries and their effect on inspection performance.
- Research novel excitation techniques for ultrasonic data compression.

1.3. Contributions to Knowledge

Knowledge contributions produced as a result of the work of this engineering doctorate are outlined below:

- Development of a novel dual phased array inspection system exploiting benefits from multiple current ultrasonic inspection techniques.

- Application of advanced ultrasonic data acquisition and imaging algorithms to the dual-array inspection system, showing improved LOSWF defect detection and imaging in narrow gap welds.
- Investigation of the dual-array setup for use as a narrow gap in-process inspection technique, building on high temperature inspection work to validate inspection performance in the presence of unfilled weld geometries.
- Application of advanced ultrasonic data acquisition imaging techniques for data compression and processing performance improvements.

1.4. Thesis Structure

Chapter 2 introduces relevant theory as a fundamental basis of understanding for the work outlined in the remainder of this thesis. This includes a brief introduction to the context and theory behind common welding practices, followed by an overview of narrow gap welding practices, advantages, limitations and common applications. The basic theory behind the propagation of sound waves in solid media is then introduced, followed by the application of this theory to the practice of ultrasonic testing. Elementary single-element ultrasonic techniques are presented, followed by the advancement of this technique to the ultrasonic phased array. Advanced ultrasonic imaging techniques are explained, as well as some additional technical information required for the understanding of the work in this thesis.

Chapter 3 introduces a novel dual-array ultrasonic inspection system for narrow gap weld inspection, with images presented and analysed based on experimental testing.

Chapter 4 builds on this work by developing the dual-array system for in-process narrow gap weld inspection, by considering the effects of partial weld geometries on the system performance. Furthermore, both amplitude and phase imaging techniques are demonstrated for defect detection and imaging.

Chapter 5 explores a technique for compressing large ultrasonic datasets at the point of acquisition by combining coded excitation and single-bit phase imaging, enabling a lightweight imaging system. This also highlights the ability to recover data resolution through data compression, allowing advanced imaging algorithms to be successfully applied to single-bit resolution ultrasonic data.

Finally, Chapter 6 summarises the work outlined in previous chapters of this thesis, and presents suggestions for future work to continue the development of an in-process narrow gap inspection system.

1.5. Journal Contributions

Lead-author journal publications produced during the fulfilment of this engineering doctorate are outlined below:

- **E. Nicolson**, E. Mohseni, Sumana, D. Lines, G. Pierce, C.N. Macleod, “Dual-tandem phased array method for imaging of near-vertical defects in narrow gap welds”, *NDT & E International*, 135(102808), 2023
- **E. Nicolson**, E. Mohseni, D. Lines, K.M.M. Tant, G. Pierce, C.N. Macleod, “Towards an in-process ultrasonic phased array inspection method for narrow gap welds”, *NDT & E International*, 144(103074), 2024

- **E. Nicolson**, E. Mohseni, D. Lines, C.N. Macleod, “Single-bit coded excitation for lightweight phase coherence imaging”, *IEEE Transactions on Ultrasonics, Ferroelectrics and Frequency Control*, In Press

Co-author journal publications produced are outlined below:

- E. A. Foster, G. Bolton, R. Bernard, M. McInnes, S. McKnight, **E. Nicolson**, C. Loukas, M. Vasilev, D. Lines, E. Mohseni, A. Gachagan, G. Pierce, C. N. Macleod, “Automated real-time Eddy current array inspection of nuclear assets”, *Sensors*, 22(16), 2022
- E. A. Foster, N. E. Sweeney, **E. Nicolson**, J. Singh, M. K. Rizwan, D. Lines, G. Pierce, E. Mohseni, A. Gachagan, K. M. M Tant, C. N. MacLeod, ‘Thermal compensation of ultrasonic transmit and receive data for steel welded plates at the point of manufacture’, *NDT & E International*, 137(102812), 2023

Co-author conference paper contributions are outlined below:

- N.E. Sweeney, D. Lines, **E. Nicolson**, C. Loukas, S. Pierce, S. Parke, C.N. Macleod, “Towards real-time quantitative monitoring and control of weld pool dimensions using phased array ultrasonics”, *ASNT Research Symposium 2023*

1.6. Conference Contributions

Lead-author conference contributions produced throughout work for this engineering doctorate are outlined below:

- **E. Nicolson**, E. Mohseni, D. Lines, G. Pierce, C.N. Macleod, “Dual-tandem phased array inspection for imaging near-vertical defects in narrow gap welds”, *QNDE 2022*
- **E. Nicolson**, E. Mohseni, D. Lines, G. Pierce, C.N. Macleod, “Dual-tandem phased array inspection method for imaging near-vertical defects in narrow gap welds”, *BINDT 2022*
- **E. Nicolson**, E. Mohseni, Sumana, D. Lines, G. Pierce, C.N. Macleod, “Dual-tandem phased array inspection for imaging near-vertical defects in narrow gap welds”, *ANRC Nuclear Showcase 2023*
- **E. Nicolson**, E. Mohseni, K.M.M. Tant, D. Lines, G. Pierce, C.N. Macleod, “Phased array inspection of narrow gap weld LOSWF defects for in-process weld inspection”, *QNDE 2023*
- **E. Nicolson**, D. Lines, C.N. Macleod, “Single-bit coded excitation for lightweight phase coherence imaging”, *BINDT 2023*

Co-author conference contributions produced throughout work for this engineering doctorate are outlined below:

- N.E. Sweeney, C.N. Macleod, **E. Nicolson**, D. Lines, S. Parke, G. Pierce, “Towards real-time ultrasound driven inspection and control of GTA welding processes for high-value manufacturing”, *QNDE 2022*
- Y. Javadi, B. Mills, P. Pourrahimian Leilabadi, **E. Nicolson**, S. Lotfian, R. Zimmermann, F. Abad, A. Mehmanparast, C.N. Macleod, G. Pierce, D. Lines, F.

Brennan, J. Mehnen, A. Gachagan, “Phased array ultrasonic testing of offshore wind bolted flange connections”, *QNDE 2023*

- A. Hifi, R.K. Wathavana Vithanage, S. McKnight, A. Poole, C. Loukas, **E. Nicolson**, E. Allan, C.N. Macleod, G. Pierce, T. O’Hare, “Flexible robotics for automated non-destructive testing” *QNDE 2023*
- R. Pyle, C.N. Macleod, K.M.M. Tant, N.E. Sweeney, J. Ludlam, **E. Nicolson**, S. McKnight, D. Lines, “Machine learning for real-time inversion of locally anisotropic weld properties using in-process layer by layer ultrasonic array measurements”, *IEEE IUS 2023*
- R. Pyle, C.N. Macleod, K.M.M. Tant, N.E. Sweeney, J. Ludlam, **E. Nicolson**, “Machine learning for real-time inversion of locally anisotropic weld properties using in-process ultrasonic array measurements”, *BINDT 2023*

1.7. Industrial Partnership

The work throughout this Engineering Doctorate has been supported by multiple industrial organisations, with a focus on advanced Non-Destructive Evaluation (NDE) activities for narrow gap weld inspection. These organisations include:

- Rolls Royce Submarines Ltd
- Babcock International Group
- Altrad Babcock (formerly Doosan Babcock)

Working with these organisations has enabled consistent engagement and collaboration with industry. This has included the development of industrial demonstrators to

highlight the work of this doctorate, as well as gaining key insight and knowledge from industry experts.

Additionally, the opportunity to attend multiple site visits has allowed deployment of on-site inspections. These visits were invaluable in propelling this work from the lab environment into industrial settings, shaping this research for current and future challenges.

This work was supported by EPSRC Centre for Doctoral Training in Future Innovation in Non-Destructive evaluation (FIND) under EPSRC Grant No. EP/S023275/1.

Chapter 2

Technical Background

This chapter will seek to introduce the key technical background as a fundamental basis of understanding for the work outlined in the remainder of this thesis. This is split into five sections, each dealing with a key fundamental field of this work.

Section 2.1 will introduce the process of fusion welding, including techniques and commonly seen flaws. Section 2.2 will specifically focus on the fusion welding of narrow gap welds, outlining techniques and the considerations required when approaching the process.

Section 2.3 will aim to introduce the physics and theory behind the behaviour of ultrasonic waves in solid as a fundamental basis for all ultrasonic testing considerations in this work.

Section 2.4 seeks to introduce basic ultrasonic testing principles, including theory surrounding the piezoelectric effect and basic single-element testing, as well as introducing some more advanced phased array techniques.

Section 2.5 will take a closer look at how advanced imaging techniques can be applied to ultrasonic phased array testing. This includes data processing, imaging methods, mode setup and delay law calculations.

2.1. Fusion Welding

Welding is a fundamental process in almost all manufacturing industries – from energy and defence, to automotive and aerospace. The art of joining individual components to assemble larger structures, devices or vehicles, is made possible by the control of mechanical, chemical and physical forces to fuse materials together.

Fusion welding is a subset of this process, describing the joining metals of similar composition by relying on melting [25]. This bonds two components together on an atomic level, creating an inherently strong fusion between deposited material and the two components [26].

2.1.1. Techniques

The process of heating and melting for fusion can be achieved by a number of methods. One example is friction welding, which requires no external heat input, and generates heat through mechanical friction alone [27]. This can be achieved through fixed techniques such as Rotary and Linear Friction Welding (RFW and LFW) [28, 29], or by using a separate rotating tool to generate friction and heat along the seam of two materials, such as Friction Stir Welding (FSW) [30]. External heat sources can also be required, including through the use of high-powered lasers [31], Electron Beam (EB)

welding [32], and induction [33]. However, perhaps the most common of these is the use of an electrical arc [34].

Arc welding works on the basis of energy transfer from electrical to heat. This process is explained physically by Joule's first law, which describes the generation of heat by the passage of a current through an electrical conductor [35]. The heat generated Q by passing a current I through a material resistance R over a time t is given by the following expression.

$$Q = I^2 R t \quad (2.1)$$

In practice, this heat transfer is enabled through the creation of a potential difference between an electrode and the desired weld specimen. This creates sufficient energy to eject valence electrons and ionise the surrounding gas, creating a plasma that is free to conduct current. This heat is sufficient to melt the specimen and generates a pool of molten metal, which when hardened joins the desired materials on a molecular level.

In processes such as Tungsten-Inert Gas (TIG) welding – sometimes referred to as Gas Tungsten Arc Welding (GTAW) – a non-consumable tungsten electrode is shielded by a non-reactive (inert) gas to prevent degradation of the electrode during heating [36]. A filler metal is supplied separately into the weld pool to fill the weld joint. TIG can also be used without a filler in a process called autogenous welding, where the filler is created by melting the parent material. Other inert gas processes such as Metal-Inert Gas (MIG) welding – sometimes referred to as Gas Metal Arc Welding (GMAW) - use

consumable wire electrodes, which also acts as the filler material and is fed into the weld pool [37, 38].

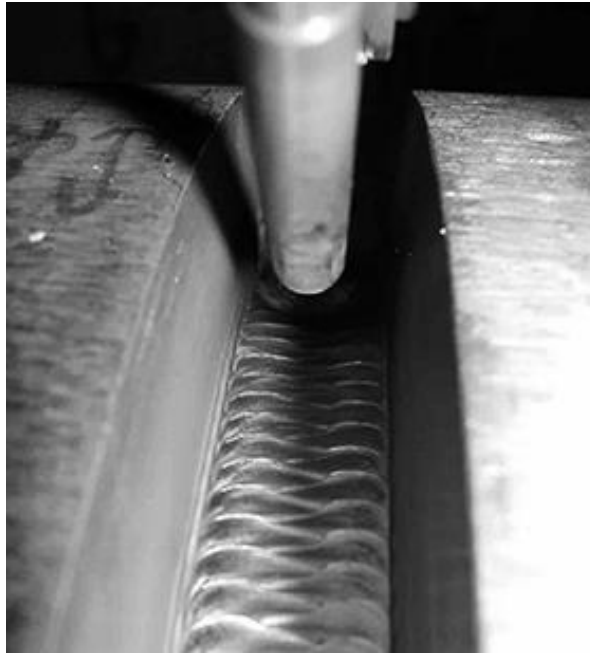


Figure 2.1: Polysoude TIG torch and weld [39]

Submerged Arc Welding (SAW) is a further arc welding process, which uses a continuously fed wire electrode surrounded by a granular flux [40]. The flux acts instead of the inert gas seen in TIG and MIG, to provide shape and stability to the arc, as well as avoid atmospheric contamination [41]. This flux is continuously fed around the wire filler, some of which is melted by the arc onto the freshly deposited weld. This melted flux is termed slag, which protects the weld pool as it solidifies.

Much higher currents are used in submerged arc welding, allowing higher deposition rates and fewer required passes per unit volume. This lends itself to narrow groove welding, where the weld can be filled much more quickly than standard TIG welding.



Figure 2.2: SAW welding, with weld torch surrounded by granular flux [42]

In all arc welding techniques, a number of variables can be altered to ensure the weldment is deposited correctly with sufficient penetration. These include the voltage applied across the electrode, the value and polarity of the welding current, the diameter and speed of the deposited wire, the welding speed, and the composition of gas or flux used. Finding the correct balance between these parameters is the basis of numerous research fields in itself, and is crucial to the quality and integrity of the final weld.

2.1.2. Defects

Due to the immense temperatures experienced during fusion welding, a Heat Affected Zone (HAZ) is created – a non-melted region around a weld that has undergone material changes due to its proximity to high temperature [43]. This zone can be prone to cracking due to the presence of Hydrogen deposited during welding, called High

Temperature Hydrogen Attack (HTHA) [44]. Over time and stress, these can cause component failure. Cold Hydrogen Induced Cracking (HIC) has also been observed once the weld has cooled, caused by moisture, dust, or residual stress from the welding procedure [45].

However, hydrogen cracking is not the only potentially critical weld defects created during fabrication. These include lack of fusion, lack of penetration, cracking, undercut, porosity and inclusions, visually demonstrated in Figure 2.3.

Lack of fusion defects can occur due to deficiencies in the welding process itself, causing the filler material to improperly fuse to the adjacent parent material. Causes include low weld current, incorrect electrode tilt or incorrect joint preparation [46]. This leaves an air pocket in the weld, which can grow in size under constant or cyclical stresses experienced over the component's lifetime. A Lack-of-Sidewall Fusion (LOSWF) arises when improper fusion occurs between the welded region and the parent material, and typically appears along the weld bevel. Lack-of-Inter-Run Fusion (LOIRF) can occur where adjacent weld passes do not properly fuse, and an air pocket appears along the inter-weld pass boundary.

Porosity describes the entrapment of gasses during weld pool solidification, causing pores to appear in the weld material. These are typically small in diameter, and are therefore often difficult to detect with ultrasonic methods. Porosity is typically caused by loss of the inert gas shield or lack of flux, the presence of moisture in or around the electrode, an unclean welding area, or a large arc length [47].

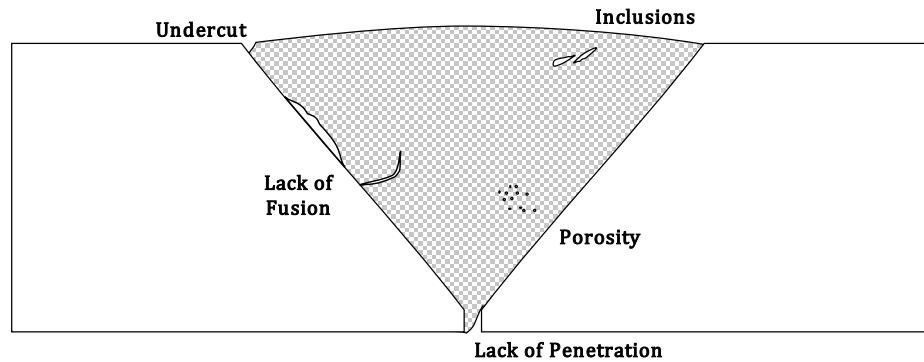


Figure 2.3: Examples of weld defects.

In order to ensure no such defects are present in a weld, NDT methods such as ultrasonic testing and radiography can be used to detect and localise defective regions within the weld volume.

2.2. Narrow Gap Welds

Narrow gap (or narrow groove) weld geometries are often preferred when approaching thick-section components for a number of reasons. Typically a J-groove geometry, narrow gap welds possess acute bevel angles, ranging from 1° to 20° [48]. These are typically used for components with large thicknesses in the range of 16 mm to 200 mm. The J-groove consists of a root, with a radius leading to the bevel to create the characteristic J shape, an example of which is displayed in Figure 2.4.

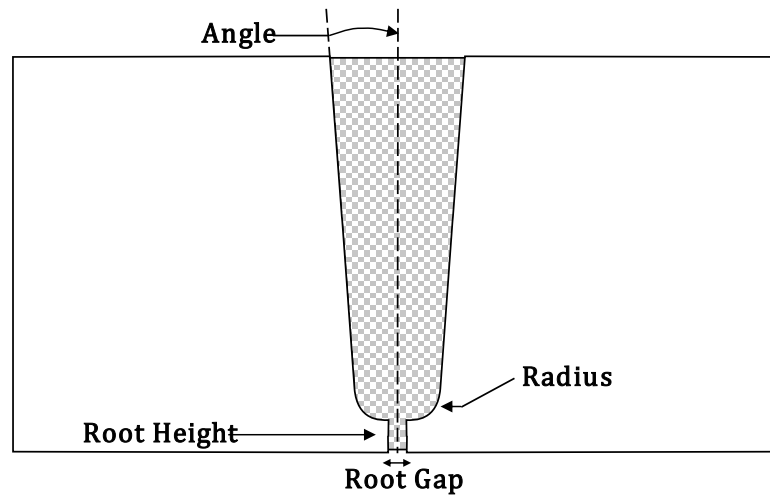


Figure 2.4: Narrow gap weld geometry

This section will explain the advantages of narrow gap use, and how this differs from traditional V-groove welding. Furthermore, the disadvantages and practical uses of this welding process will be discussed.

2.2.1. Narrow Gap Welding Techniques

Narrow groove geometries have been utilised for a variety of welding techniques when approaching thick section components. Typically, arc processes such as TIG or SAW welding are used. These often utilise specialised welding torches to navigate the narrow groove, and require skilled operators to ensure suitable welding parameters and positioning tolerances [49, 50].

The use of non-arc processes such as laser [51, 52] and EB [53] welding has gained traction as a method for thick section narrow groove welds. Both promise a number of benefits, including reduced access requirements and welding times, and limited HAZ [54]. However, in the case of EB welding, a vacuum is required to ensure interactions

between electrons and air molecules do not effect the beam direction or energy. This requires either a vacuum chamber capable of encapsulating the entire component, or a local vacuum system. Although laser welding does not require a vacuum, it does require relatively high tolerances in both machining and placement of the component, which can be expensive particularly for large sections.

2.2.2. Advantages of Narrow gap Use

There are numerous advantages to selecting a narrow gap geometry when approaching specific welding scenarios. The first and most obvious advantage is the reduction in weld volume required to complete the weld. To quantify this, an approximate cross-sectional area can be calculated by assuming a V- and J-groove weld geometry shown in Figure 2.5.

The calculation for the V-groove area A_V can be made given a height h , root gap g_V and angle θ_V using equation (2.2). For a J-groove with an angle θ_J and root gap g_J , the radius r_J of the bevel must be considered. The expression for the area A_J is shown in (2.3).

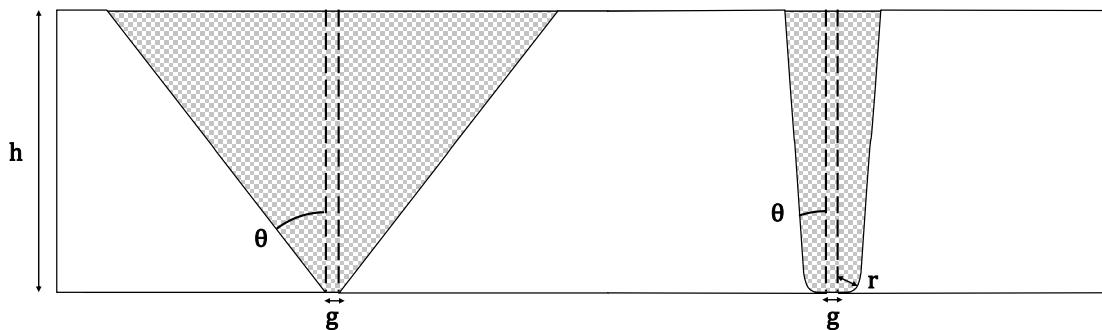


Figure 2.5: Approximation of weld area for V- and J-groove welds

$$A_V = 2h^2 (\tan(\theta_V) + g_V) \quad (2.2)$$

$$A_J = g_J r_J + \frac{\pi r_J^2}{2} + (g_J + 2r_J)(h - r_J) + 2(h - r_J)^2 \tan(\theta_J) \quad (2.3)$$

Considering a typical V-groove angle of 37.5° and a narrow gap angle of 1.5° with a 6 mm radius, there is a clear difference in weld area as shown in Figure 2.6. For large thicknesses, narrow gap welds boast an 85% reduction in weld volume, however for lower thicknesses (2 to 8 mm), the V-groove has the lowest weld volume.

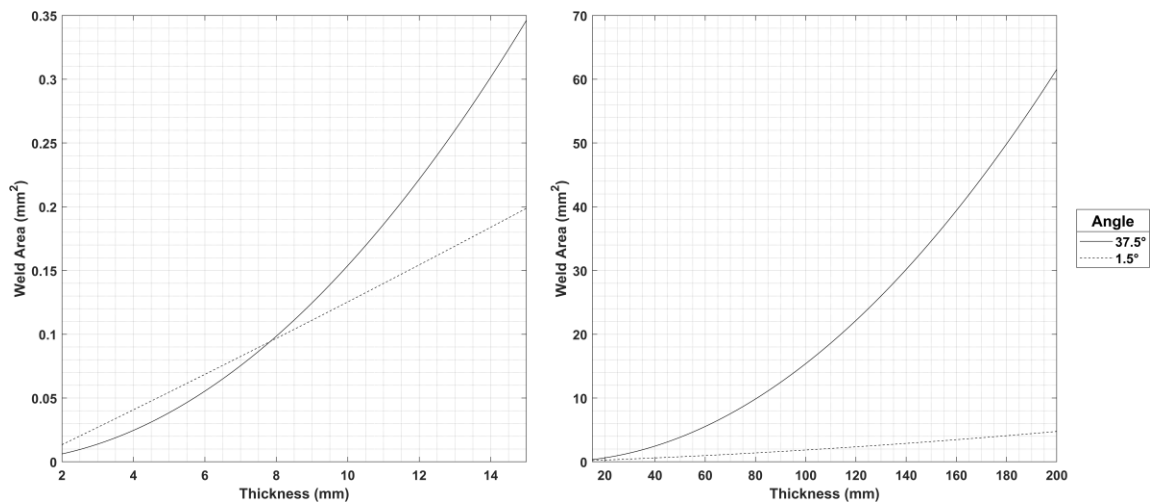


Figure 2.6: Thickness vs. weld area for a typical V-groove angle of 37.5° and a narrow groove angle of 1.5° . Left-hand graph shows zoomed-in view of right graph at low thicknesses to show crossover point

The reduced volume at large thicknesses enables faster, more efficient welding processes. Less deposited volume means that welding time is also reduced, along with the filler material required. Furthermore, reduced labour costs and arc time per weld has additional financial benefits. Finally, the heat input required is much less, as both the time for heating and the volume required to be heated are less than for a typical V-groove. This is also environmentally beneficial as energy use is reduced.

A further benefit of the narrow gap weld for thick section components is the increased weld quality [55], largely due to reduced thermal stresses and reduced weld volume. This results in reduced fracture and weld distortion rates [56]. Additionally, as grooves are near-parallel stress on the root and hot passes are reduced due to the near-uniform weld width along its thickness.

2.2.3. Disadvantages of Narrow Gap Use

Despite the manufacturing and economic benefits of narrow gap welds, they do exhibit some disadvantages that must be considered. The first of these is the machining of the joint pre-welding. This can often be an expensive and timely process, as the J-geometry requires more complex machining considerations when compared to V-grooves.

Additionally, poor accessibility during welding due to the nature of its narrow groove geometry results in difficult access to the weld – particularly at the root and close to the bevel. For this reason, welding can be difficult and therefore prone to more defects, such as LOSWF. Detecting and characterising these LOSWF defects can be difficult, and is a challenge facing many manufacturing industries.

2.2.4. Narrow Gap Applications

As narrow gap geometries are often preferred when thick section high quality welds are required, they are typically used within heavy manufacturing and power generation industries.

Particularly within the nuclear energy industry, narrow gap welds play an important structural role, from the joining of pressure vessel nozzles [57-60] to rotatable plugs

used for fuel handling in reactors [61]. These are chosen due to the heavy gauge steel required to ensure structural integrity under the high pressures and temperatures faced across nuclear fission infrastructure.

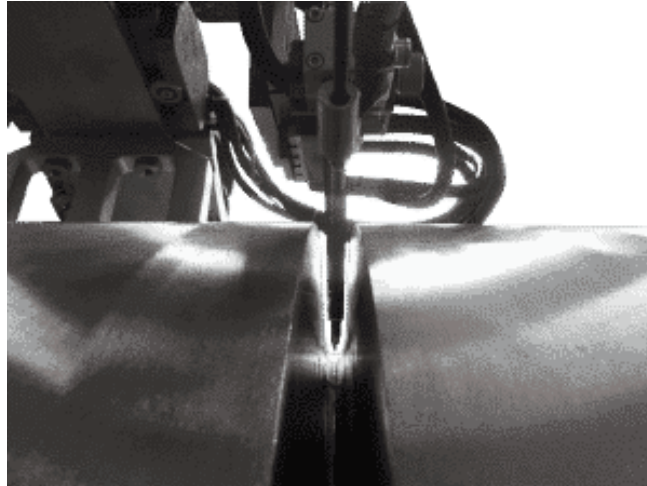


Figure 2.7: Narrow gap pipe girth weld and Polysoude TIG torch [62]

Additionally, the use of narrow gap welding is found in the Oil and Gas industry, for offshore pipeline and platform construction [63-65]. Again, these must withstand external conditions such as stresses caused by under-seabed conditions, cyclical stresses experienced by shifting platforms and ocean currents, and internal conditions from highly-pressurised pipes. Narrow gap welds are also found throughout the wider energy sector turbine blades, boiler tubes and heat exchangers, and more broadly in ship hulls and heavy machinery.

2.3. Ultrasonic Waves in Solids

Sound is a term given to the vibration of molecules due to pressure differences. In a solid medium, an applied external force can displace molecules from equilibrium,

altering the local density and changing regional pressure. As the molecules tend back to equilibrium, kinetic energy from the initial displacement is transferred throughout the medium. This molecular energy transfer is typically considered a wave, describing the changing displacement or pressure of particles across time.

Sound waves with a frequency greater than 20 kHz are deemed to be ‘ultrasonic’ waves [66]. These waves have numerous applications across industry and science for a number of reasons. This is in part due to their slow velocity relative to electromagnetic waves which allows easier control and manipulation, and their ability to penetrate most materials with relatively inexpensive sources. Applications range from medical to industrial. Ultrasound is even found in nature for communication and echolocation [67-69].

However, for most industrial applications such as welding and component inspection, propagation of ultrasound in solids is most common. This section will discuss the basic fundamentals of the behaviour of ultrasonic waves in solid materials.

2.3.1. Wave Modes

When considering bulk ultrasonic waves, it often aids simplicity to assume an infinite medium. In such a material, waves typically travel as either one of two wave types [70]. The first is the longitudinal wave which alters the density of a lattice parallel to the direction of wave travel.

The second is the shear (or transverse) wave, which distort the shape of a lattice without altering its density, and particle motion is perpendicular to the travelling direction.

Figure 2.8 shows the propagation of longitudinal and shear waves schematically. Longitudinal waves tend to exhibit higher velocities than shear waves, and can propagate through solids, liquids and gasses. In contrast shear waves are unable to propagate through materials with low shear stiffness, and therefore cannot travel through gasses and low viscosity liquids.

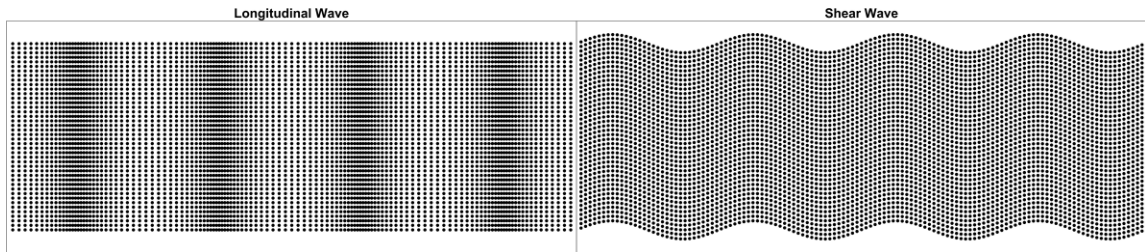


Figure 2.8: Longitudinal and shear wave mode visualised in MATLAB by displacement of uniform 2D crystal lattice

The choice of wave propagation type is often termed the wave ‘mode’, and for bulk waves are limited to shear and longitudinal. A number of other wave types are observed, particularly when considering those along the boundary of two materials. These include Rayleigh waves [71], Lamb waves [72] and Love waves [73], which are irrelevant to the work outlined in this thesis. The ‘creep wave’ (or high-angle longitudinal wave) is often considered it’s own wave type, and is not considered a true surface wave. It is seen in specific ultrasonic techniques, and will be discussed later in this chapter.

2.3.2. Waves at Boundaries

The acoustic impedance Z of an isotropic material is defined as the product of its velocity c and density ρ , as described in (2.4). To understand the propagation of sound across an impedance change (or boundary), it is often necessary to assume lossless

media with perfect energy transfer between molecules. The percentage of incident energy transmitted E_T and reflected E_R for such a case are described in equations (2.5) and (2.6) respectively, for a wave incident on a perpendicular boundary between two impedances Z_1 and Z_2 [74].

$$Z = \rho c \quad (2.4)$$

$$E_T = \frac{4Z_1Z_2}{(Z_1 + Z_2)^2} \quad (2.5)$$

$$E_R = \left(\frac{Z_1 - Z_2}{Z_1 + Z_2}\right)^2 \quad (2.6)$$

This relationship shows that for a large variation in impedances at a boundary, a greater percentage of incident energy is reflected than transmitted. This relationship is visualised in Figure 2.9, for impedance ratio Z_2/Z_1 against transmitted and reflected energy. Peak transmission occurs when $Z_2 = Z_1$, decreasing as the mismatch increases. This relationship is the fundamental basis of using ultrasonic waves for material inspection, which is discussed later in this chapter.

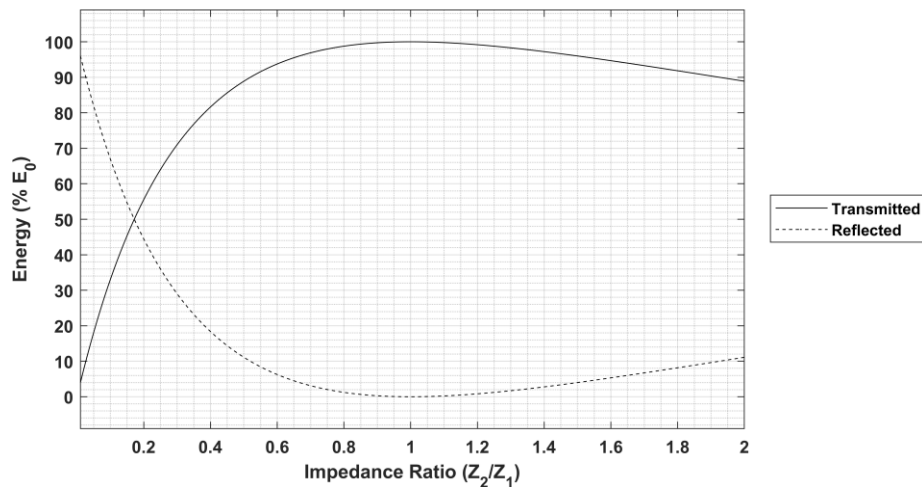


Figure 2.9: Transmitted and reflected energy based on impedance mismatch

When incident on a boundary at a non-normal angle, there are several conditions to consider regarding reflection, refraction and mode conversion.

For a sound wave incident on a boundary between two materials of different impedances at a non-zero incident angle, the reflected and refracted angles for both longitudinal and shear modes can be described by the expression in equation (2.7). For an angle θ and velocity c , the first subscript describes the wave mode associated and the second the material in which the behaviour is described.

$$\frac{\sin(\theta_{L1})}{c_{L1}} = \frac{\sin(\theta_{L2})}{c_{L2}} = \frac{\sin(\theta_{T1})}{c_{T1}} = \frac{\sin(\theta_{T2})}{c_{T2}} \quad (2.7)$$

There are often two critical angles associated with sound waves at a boundary as described above – one for each wave mode. The first critical angle describes the incidence at which the longitudinal wave refracts at a 90° angle to the boundary normal. In this case, only a surface wave is produced alongside the reflected waves and mode converted shear wave. Similarly, at the second critical angle occurs at the point where no sound energy is refracted, and is either reflected or generates a surface wave. These conditions can be described by the following expression, where c_2 is the longitudinal or shear velocity of the second material, based on calculation of the first or second critical angle respectively. The incident velocity c_I is the longitudinal velocity of the incident material.

$$\theta_1 = \sin^{-1}\left(\frac{c_I}{c_2}\right) \quad (2.8)$$

For a water ($c_L = 1481 \text{ ms}^{-1}$ [75]) to steel ($c_L = 5940 \text{ ms}^{-1}$ and $c_T = 3220 \text{ ms}^{-1}$ [76]) boundary, the refraction behaviour of an incident sound wave at varying angles is depicted graphically in Figure 2.10. The first critical angle, after which no longitudinal wave energy is transmitted, and the second critical angle, after which no shear wave velocity is transmitted, are 14.50° and 27.45° respectively.

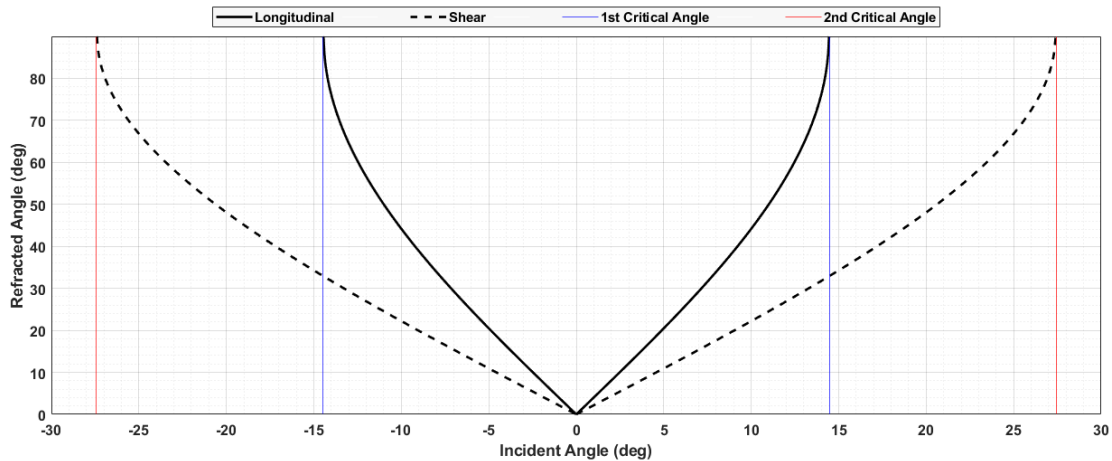


Figure 2.10: Refraction of sound through water-steel boundary, with first (blue) and second (red) critical angles indicated

High angle longitudinal waves exhibit unique behaviour, such that they are separately termed ‘creep waves’. These travel almost parallel to the boundary of a material, and are seen in a number of ultrasonic testing applications.

2.3.3. Mechanical Properties

The behaviour of sound propagation in solid materials is dictated by a number of mechanical (or elastic) properties. These values relate the proportionality of displacement of a material given applied forces, in term of stress σ and strain ε .

Stress is defined as the force F applied per unit area of a cross section A , and strain defined as the displacement Δl of a material of length l [77].

$$\sigma = \frac{F}{A} \quad (2.9)$$

$$\varepsilon = \frac{\Delta l}{l} \quad (2.10)$$

For isotropic materials, elastic constants are independent of direction and considered uniform. Conversely, anisotropic materials have positionally and directionally dependent elastic properties. In reality, all metallic materials possess some degree of anisotropy due to asymmetric molecular lattice arrangements. The extent of this anisotropy can be dictated by lattice structure and forming processes, with certain alloys and metals exhibiting higher or lower levels. In this work, materials with relatively low anisotropy such as carbon steel are assumed to be isotropic unless stated otherwise.

The elastic constants required for consideration of sound propagation in solid materials are briefly described in the following sections.

2.3.3.1. Young's Modulus

Young's modulus E describes the relationship between stress σ_{xx} and strain ε_{xx} of a material along a single axis x by the following definition, given that there is zero stress in all other spatial dimensions [78].

$$E = \frac{\sigma_{xx}}{\varepsilon_{xx}} = \frac{F_x l_x}{A_x \Delta l_x} \quad (2.11)$$

This considers an applied force F_x to a perpendicular cross section A_x , causing a displacement Δl_x of the material along the force axis x for a given length l_x . Figure 2.11 shows the relationship between these values visually.

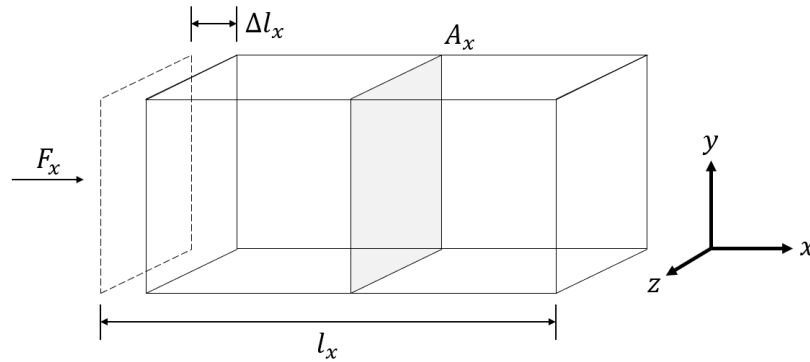


Figure 2.11: Young's modulus

2.3.3.2. Shear Modulus

The Shear Modulus G describes the relationship between shear stress σ_{xy} and shear strain ε_{xy} of a material, given by the following definition [78].

$$G = \frac{\sigma_{xy}}{\varepsilon_{xy}} = \frac{F_x l_y}{A_y \Delta l_x} \quad (2.12)$$

This considers a force applied F_x to a parallel cross section A_y , causing a displacement Δl_x of the material along the force axis x for a given length l_y . Figure 2.12 shows the relationship between these values visually.

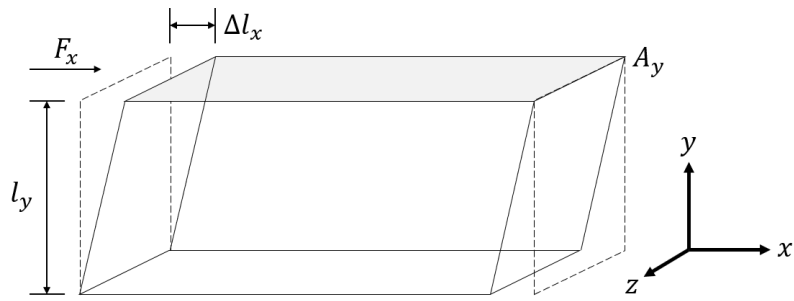


Figure 2.12: Shear modulus

2.3.3.3. Poisson's Ratio

Poisson's ratio ν describes the strain ϵ_{yy} in y caused by perpendicular loading ϵ_{xx} in x , as shown in the following expression [78].

$$\nu = -\frac{\epsilon_{yy}}{\epsilon_{xx}} = \frac{l_x \Delta l_y}{l_y \Delta l_x} \quad (2.13)$$

This considers the displacement Δl_y of a given length l_y given an axial displacement Δl_x of side length l_x . Figure 2.13 shows the relationship between these values visually.

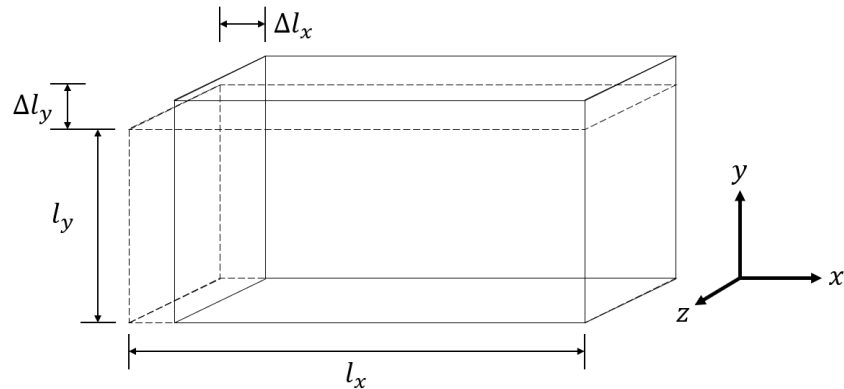


Figure 2.13: Poisson's Ratio

Assuming an isotropic material, the Young's and Shear moduli are related using Poisson's ratio by the following expression.

$$E = 2G(1 + \nu) \quad (2.14)$$

2.3.4. Wave Propagation

Along with the density of a material ρ , the elastic constants can be used to calculate velocities of longitudinal c_L and shear c_T waves assuming isotropy. Using equation (2.14), both velocities can be defined using only the material density, Young's modulus and Poisson's ratio.

$$c_L = \sqrt{\frac{E(1 - \nu)}{\rho(1 + \nu)(1 - 2\nu)}} \quad (2.15)$$

$$c_T = \sqrt{\frac{G}{\rho}} = \sqrt{\frac{E}{2\rho(1 + \nu)}} \quad (2.16)$$

The wave equation for a three-dimensional solid is derived from Newton's second law of motion. Assuming an isotropic elastic material, the equation describing a field \mathbf{u} and material velocity c is shown below.

$$\left(\nabla^2 - \frac{1}{c^2} \frac{\partial^2}{\partial t^2} \right) \mathbf{u}(x, y, z, t) = 0 \quad (2.17)$$

$$\text{Where } \nabla^2 = \frac{\partial^2}{\partial x^2} + \frac{\partial^2}{\partial y^2} + \frac{\partial^2}{\partial z^2} \quad (2.18)$$

This can be defined separately for both longitudinal and shear waves. The wave equations for both longitudinal and shear waves can then be defined as follows [70].

$$\left(\frac{\partial^2}{\partial x^2} - \frac{1}{c_L^2} \frac{\partial^2}{\partial t^2} \right) u_x = 0 \quad (2.19)$$

$$\left(\frac{\partial^2}{\partial y^2} - \frac{1}{c_T^2} \frac{\partial^2}{\partial t^2} \right) u_y = 0 \quad (2.20)$$

$$\left(\frac{\partial^2}{\partial z^2} - \frac{1}{c_T^2} \frac{\partial^2}{\partial t^2}\right) u_z = 0 \quad (2.21)$$

2.4. Fundamentals of Ultrasonic Testing

The ability to check the integrity of a material non-destructively is a crucial process across a number of industrial and medical industries. This has been approached using a number of different techniques, utilising electrical, radiological and mechanical methods. The use of radiology and magnetic resonance methods [79] are commonplace for medical imaging, with eddy current [80], liquid penetrant [81], thermographic [82], radiographic [83] and magnetic particle testing [74] all utilised for industrial asset inspection. However, one of the most diverse and practical inspection methods across both medical imaging and industrial NDT is ultrasound. The transmission of vibrational waves through a medium has applications ranging from safe pregnancy screenings [84], to in-process weld [85-87] and Wire + Arc Additive Manufacturing (WAAM) inspection [88-90]. Particularly in NDT fields, where regular inspections of large components are required, ultrasound provides a solution for fast automated scanning.

Ultrasonics has been the subject of research for a number of applications since World War I, with ultrasonic material inspection first proposed in the 1930s [91, 92]. In 1942, the first ultrasonic NDT method was introduced, when a patent was granted for a method of “*Supersonic Inspection*” to University of Michigan professor Floyd A. Firestone [93]. This device was named the Supersonic Reflectoscope, which sent short pulses into a sample through a 1 μ s, 500 V excitation of a quartz crystal for the detection of flaws in

metal components [94]. Devices for thickness measurements [95] and angled beam inspections [96] were introduced shortly afterwards.

Later (in the 1950s), procedures were introduced by the American Society for testing and Materials (ASTM) for ultrasonic butt weld inspection, terminology and reference block standardisation [92]. These technologies and standards were the basis for the ultrasonic testing devices and procedures we use today.

The migration of the phased array technology from radar and sonar into medical fields occurred in the 1960s for fast scanning diagnosis [97]. Despite initial research in the 1950s [98], phased array technology only reached widespread industrial inspection applications in the 1980s, using modified medical probes for crack detection in welded steel samples [99].

Nowadays, ultrasonic phased arrays are the subject of advanced research and deployment for use in NDT [100]. This includes machine-learning assisted and automated inspection of delamination in Carbon-Fibre Reinforced Plastics (CFRP) [101, 102], to laser-induced ultrasonic phased arrays [103, 104], and material microstructure characterisation using deep learning [105].

The following section will outline the principles of ultrasonic testing, from the physical laws behind transmission and reception of high frequency sound waves, to the use of single element and phased array technology for flaw detection.

2.4.1. Piezoelectric Effect

The piezoelectric effect, first demonstrated in the late 19th century by Pierre and Jacques Curie [106], has been fundamental to the manufacture and design of the ultrasonic probes for medical and NDT applications. The effect describes the behaviour of piezoelectric materials that experience a mechanical stress when subjected to an externally applied electric field [107].

The effect arises due to the intrinsic link between elastic and electric properties in piezoelectric materials, by the volume density of electric dipoles. This dipole density is referred to as the polarisation. When experiencing no external forces, the molecules within piezoelectric materials are electrically neutral. However, when experiencing an external force, molecules are compacted and an overall polarisation is formed by the resulting Coulomb force of aligned electric dipoles. The formation of an electric field allows the conductivity of free electric charge, and a voltage is produced relative to the strength of the field. On the removal of the external force, the piezoelectric material returns to an unpolarised state and the electric field weakens to a negligible magnitude. The inverse to this is also true - where an electric field is generated under the external mechanical compression due to changing external pressures [91].

This is the principle of the piezoelectric effect, and is exploited in ultrasonic transducers to both transmit and detect pressure waves. The most common transducer piezo is the ceramic lead zirconate titanate (or PZT) [74, 107]. However, despite exemption by the Restriction of Hazardous Substances Directive (RoHS), a collective effort has been made in recent years to research and manufacture lead-free alternatives [108].

2.4.2. Single Element Ultrasound

The most basic form of ultrasonic NDT inspection is the use of single element transducers. These utilise a single piezoelectric element for both transmission and reception of ultrasonic waves. This is typically done in contact with a specimen, with the aid of a thin layer of liquid coupling to maximise energy transfer from transducer to specimen by removing air gaps. This can be water, oil or glycerine, as long as the material is elastic in nature [109]. Alternatively, immersion techniques improve coupling by submerging both probe and specimen in water.

Single-element transducers can also be used with an angled delay line, called a wedge. These allow sound to be propagated at an angle relative to the surface of a component, and is typically used for inspection of welded components where inspection cannot be done on the rough weld cap [24].

As mentioned earlier in the chapter, reflection of ultrasound energy is proportional to the impedance change Z across a boundary (equation (2.6)). This allows the presence of defects in materials to be observed by the reflection of ultrasonic waves.

Considering the case of the transmission of ultrasound by a transducer into a steel specimen ($Z \approx 47$ MRayls) containing an air-filled defect (air $Z \approx 0.0004$ MRayls), we can expect close to 100% of the energy to be reflected ($> 99.9\%$). A portion of this reflected energy will return back to the transducer and the presence of the defect can be known.

This detection process may utilise two transducers – one transmitting and one receiving ultrasonic signals – or by a single transducer handling both transmission and reception. The first case with two transducers is often termed ‘pitch-catch’, while the most common is the single transducer case termed ‘pulse-echo’. In either case, the data detected by the transducer is displayed on a time series plot called an ‘A-scan’. An example of three inspection scenarios with single element transducers in pulse-echo mode are shown in Figure 2.14, with the corresponding expected A-scans displayed in Figure 2.15.

Figure 2.14(a) shows the case where no defect is present in a specimen, and the transmitted wave is reflected from the backwall to the transducer uninterrupted. The expected A-scan obtained shows a single response at a time corresponding to the travel time of the wave in the specimen, as shown in Figure 2.15(a).

For the case of a defect present, the size will dictate the behaviour of the signal received. Figure 2.14(b) shows the case of a transducer above a small defect. In this case, some energy is reflected by the transducer, but as the defect is smaller than the beam width, a portion of energy is not reflected and continues to the backwall. The A-scan obtained shows two responses – one from the backwall and a smaller one from the defect as shown in Figure 2.15(b). The backwall response will also be reduced in amplitude relative to the no defect case due to the reduction in energy reaching the backwall by the presence of a defect.

The case of a large elongated defect is shown in Figure 2.14(c), where the defect is large enough to cover the full transducer beam width and reflected the majority of energy

back to the transducer at that point. Figure 2.15(c) shows that the A-scan contains a single response, recognisable as a defect due to the shift in time of the response relative to the backwall response.

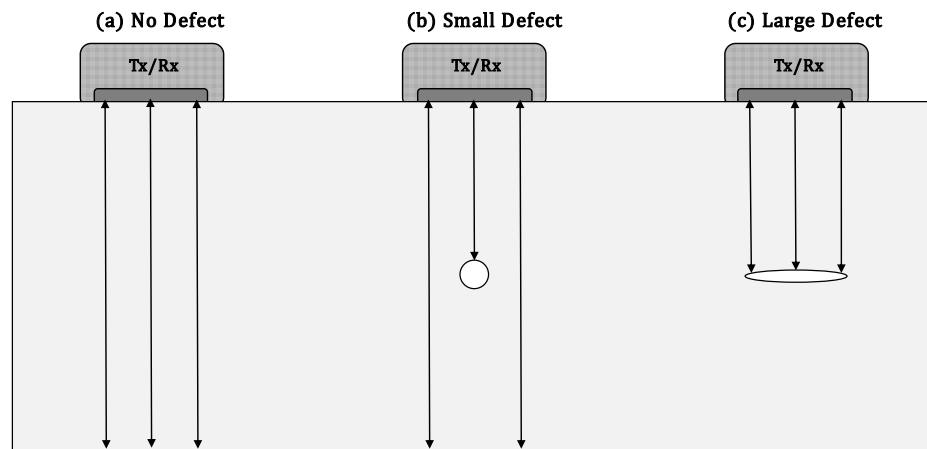


Figure 2.14: Single element ultrasonic inspection with (a) no defect, (b) small defect and (c) large defect

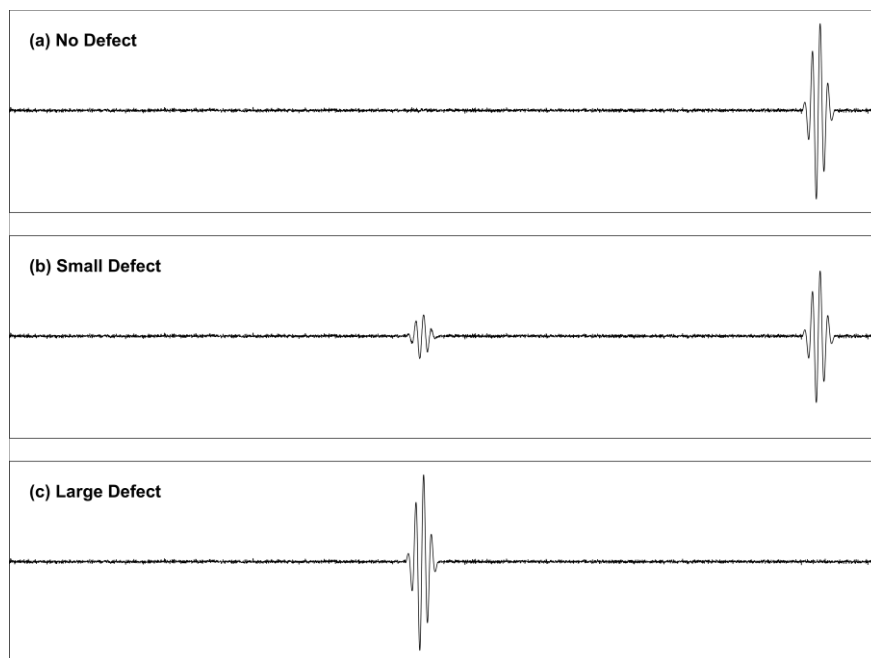


Figure 2.15: Theoretical A-Scans obtained from inspections scenarios shown in Figure 2.14 for (a) no defect, (b) small defect and (c) large defect

This is the most basic form of ultrasonic testing, and requires a skilled operator to interpret signals for detection and characterisation of defects.

2.4.3. Time-of-Flight Diffraction

Time-of-Flight Diffraction (TOFD) is a fundamental ultrasonic inspection technique, first demonstrated in 1975 [110]. It utilises two angled single-element probes placed on opposite sides of an inspection area, as shown in Figure 2.16 and Figure 2.17. These are configured in a transmit-receive (or pitch-catch) mode, where one probe transmits energy in the form of ultrasound and the other probe receives responses. The distance between the probes is called Probe Centre Spacing (PCS), and is specific to the inspection thickness and angle of probe used [111].



Figure 2.16: Orbital TOFD scanner [112]

TOFD is designed to provide high sensitivity to diffractive effects experienced when a wavefront is incident on defects acting as a point source. For a typical inspection involving a crack, four main responses are expected. The first is the Lateral Wave (LW), which is a creep wave travelling between the exit points of the transmit and receive probes. This has the shortest possible Time-of-Flight (ToF) and is the first response observed by the receive probe. If the surface is rough, or is ‘broken’ by a trench, the LW will disappear as the surface wave is scattered or reflected by obstacles.

A second common response is that of the backwall reflection. This, is often high amplitude, and therefore create a dead zone around the response location where potential defects will be masked. However, there are potentially ways around these dead zones, such as considering mode-converted waves which have been shown to mitigate defect masking [113, 114]. Additionally, the LW can be useful for calibration purposes [111].

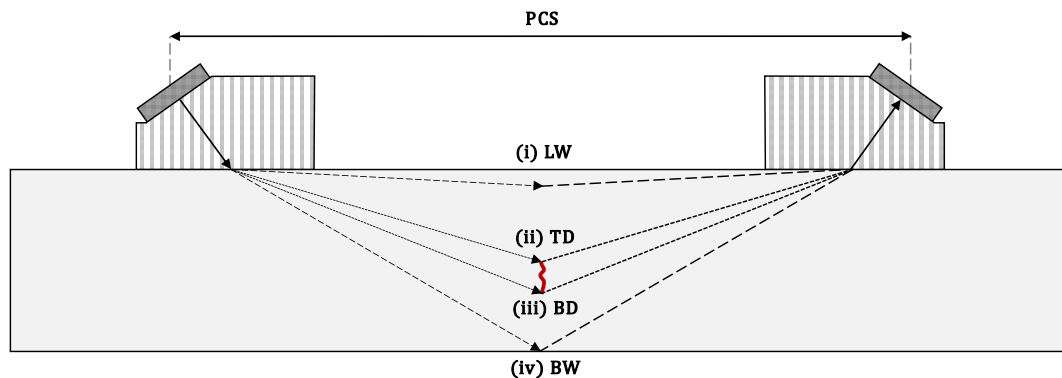


Figure 2.17: TOFD setup for crack (outlined in red) inspection, showing paths of lateral wave (i), top (ii) and bottom (iii) tip diffraction and backwall (iv) reflection

Tip diffraction responses from a crack present in the bulk of the material will appear between the LW and backwall responses in time. Given both top and bottom tips can be resolved, the size of the crack can be determined by the ToF of each tip response. An

example of an expected response from a TOFD setup detecting a bulk crack is shown in Figure 2.18.

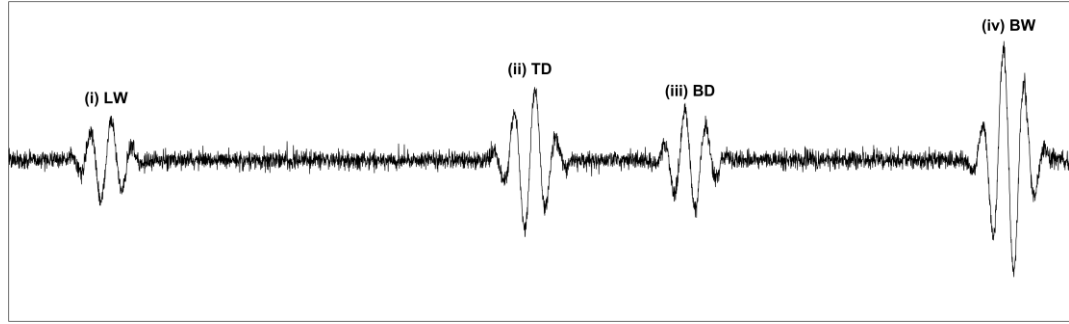


Figure 2.18: Typical TOFD scan, showing tip diffraction responses of bulk crack between lateral wave and backwall

As the relationship between ToF and depth is not linear, it can be difficult to interpret the size of a defect from a TOFD scan. Given a PCS of S and a ToF of τ_T , the depth d of an indication can be calculated using (2.22), assuming an isotropic medium with longitudinal velocity c_L .

$$d = \sqrt{\left(\frac{c_L \tau_T}{2}\right)^2 - \frac{S^2}{4}} \quad (2.22)$$

However, this assumes no wedge delay. In order to compensate for the wedge travel time at both ends, the ToF can be replaced by the time in the medium t , defined by the total ToF τ_T and time in the wedge τ_W .

$$t = \tau_T - 2\tau_W \quad (2.23)$$

Calculating the depth value of each of the tip diffraction indications of a crack in this manner can provide a value for its through-wall height.

TOFD is well standardised and utilised across industry for crack detection [111]. Considerations include PCS, wedge angle, frequency and transducer size based upon the specimen thickness. The PCS is defined by the position of beam intersection as a fraction of the specimen depth. Multiple TOFD scans are often required for large thicknesses, each utilising a different PCS and probe angle [111]. For this reason, TOFD requires a skilled certified operator.

2.4.4. Ultrasonic Phased Array

Nowadays, phased Array Ultrasonic Testing (PAUT) is often the ultrasonic method of choice for NDT across numerous industries. Phased array transducers combine a number of piezoelectric elements into a single transducer housing, with the ability to excite elements individually. PAUT has demonstrated great flexibility and adaptability relative to traditional single element inspection techniques, by allowing beam focussing and steering to be performed quickly and consistently.

Phased array transducers are manufactured in a variety of formats, including two-dimensional matrix and Transmit-Receive Longitudinal (TRL) arrays. However, the most common is the one-dimensional, or linear phased array, which contains a number of transmitting elements set along a single linear axis.

Several parameters are used to describe a phased array probe. The element pitch p describes the distance from the centre of one element to that of an adjacent element. This can be described by the summation of the element width l_x along the array axis and the gap between adjacent elements Δx . The length of the element l_y is often called the

elevation, and dictates the energy transmitted by firing a single element. These parameters are noted visually in Figure 2.19.

The choice of pitch size can be crucial to the performance of the phased array probe. It is common practice to specify that the element pitch is no greater than a wavelength – ideally less than a half wavelength - in order to suppress grating lobes [115, 116]. These grating lobes direct energy away from the main ultrasonic beam, and can cause unwanted reflections and interference during inspection that can reduce Signal-to-Noise Ratio (SNR) and introduce artefacts. This means that the pitch of a desired phased array probe has an inversely proportional relationship with the probe frequency.

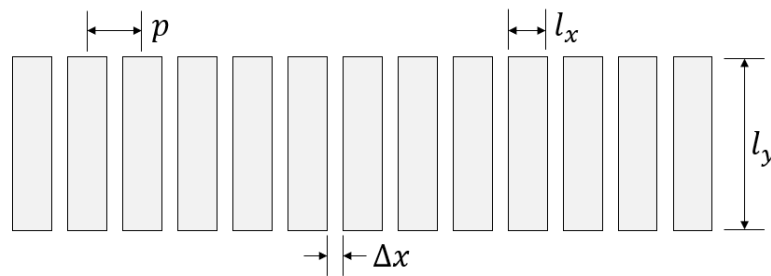


Figure 2.19: Linear phased array indicating common parameters of element pitch p , width l_x , length l_y and gap Δx

The steering and focusing capabilities of the phased array has set it apart from other conventional techniques. This is achieved by controlling the delay, voltage and pulse width of individual element excitation. Additionally, excitation of sets of elements allows electronic scanning across the full array using a reduced aperture. Traditional single element scanning techniques such as the Synthetic Aperture Focusing Technique (SAFT) often required high precision and long inspections [117]. The phased array

allows this process to be completed several times per second without the need for physical manipulation of the probe.

Manipulation of the phased array beam can be conducted by using 2 or more elements at once. Applying delays between excitation of each element can change both the direction and shape of the beam by constructive interference of phase delayed waves.

An unfocused plane wave can be transmitted by applying no delay to the elements, such that they are fired simultaneously as shown in Figure 2.20(a). Furthermore, steering of the ultrasonic beam can be done by applying a linear delay across transmitting elements as shown in Figure 2.20(b). Figure 2.20(c) highlights the focusing capabilities of the array, in this case focusing directly underneath the aperture centre by applying symmetric delay laws. Steering and focusing can be combined to focus at a point not underneath the aperture, as shown in Figure 2.20(d).

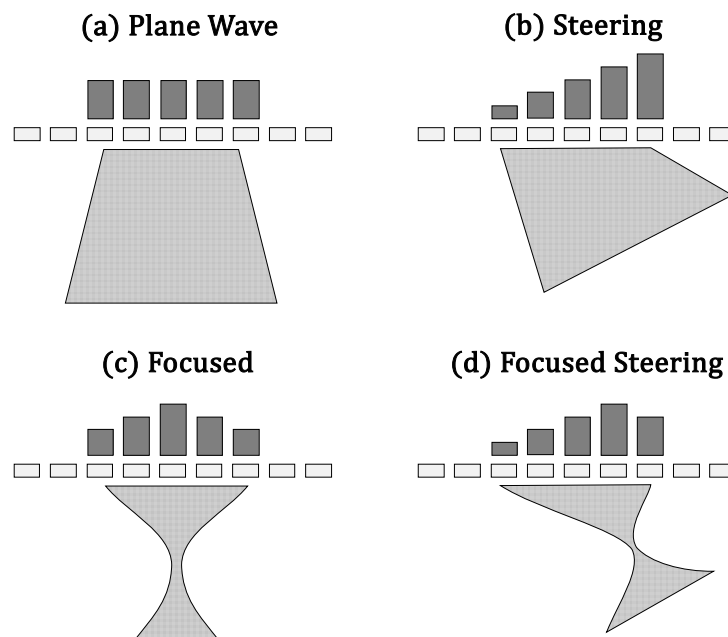


Figure 2.20: Beamforming capabilities of the ultrasonic phased array

In addition to reducing inspection time, the phased array has enabled the use of ultrasonic imaging techniques, starting with the B-scan. This stacks several A-scans together to form a single image.

B-scans can be represented in a number of ways, depending on the scan-type used to obtain the A-scan data. The most simple is the electronic scan, where an image is formed by the linear scanning of an element or elements across the array. These can be focused and steered, but are often used to observe a region of interest underneath the array, as shown in Figure 2.21(a). Here, a 64-element array was used in contact with a type B steel calibration block, to image Side Drilled Holes (SDH) while scanning with a 16-element focused aperture.

The second B-scan type is the sector scan, which often utilises the full array aperture to transmit at a range of angles. These are often used with the aid of a physical angled delay line, called a wedge. These aid the steering of the ultrasonic beam by placing the array at an angle relative to the surface of a specimen. The B-scan for such a scan is often represented on a fan or radar type plot corresponding to the angle of each transmitted A-scan, as shown in Figure 2.21(b). In this case, a 64-element array with a 55° shear wedge was used to fire at angles ranging from 10° to 75° to image SDHs of an ASTM E2491 phased array assessment block (1018 steel) [118].

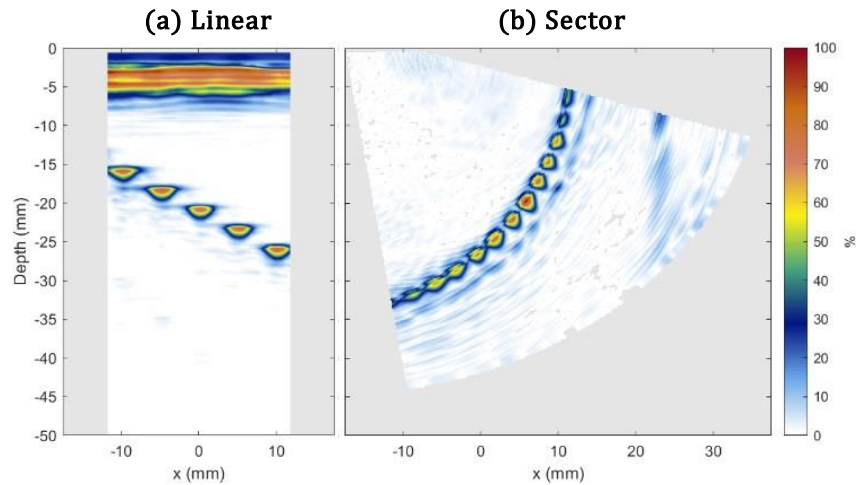


Figure 2.21: Examples of a (a) linear and (b) sector scan

By capturing B-scan data at regular intervals across a sample, a C-can image can be generated. This is a plan view of the scan, and allows large volumes of data to be visualised quickly and practically.

TOFD has also been considered for use with phased array probes rather than single-element [119, 120]. Phased Array TOFD (PA-TOFD) would allow multiple transmission angle scans to be conducted simultaneously, with PCS adjustment by selecting an array sub-aperture for each angle transmission. This could reduce the number of physical scans required while allowing for the addition of focused TOFD and improving overall sensitivity, however, this has not been widely researched or adopted.

2.4.5. Full Matrix Capture

The advancement of phased array technology has also allowed for the acquisition of a time signal from every transmit-receive pair in an array [121]. This is achieved through

Full Matrix Capture [122], and allows the post processing of ultrasonic data using a number of imaging algorithms.

FMC requires the iterative firing of single elements, while receiving across all elements in the array. Given an array with N elements, N^2 A-scans are obtained in the FMC dataset for a single frame. This possesses the advantage of flexibility over conventional PAUT, as most (except when considering a non-linear regime) PAUT imaging techniques can be synthetically generated from post-processing FMC data. However, acquisition and data transfer rates are slower, and processing can often be computationally intensive.

The data matrix obtained from FMC acquisition can be visualised as in Figure 2.22, for an N element array. Each grid point represents an A-scan $A_{tx,rx}$, for a transmitting element tx and receiving element rx .

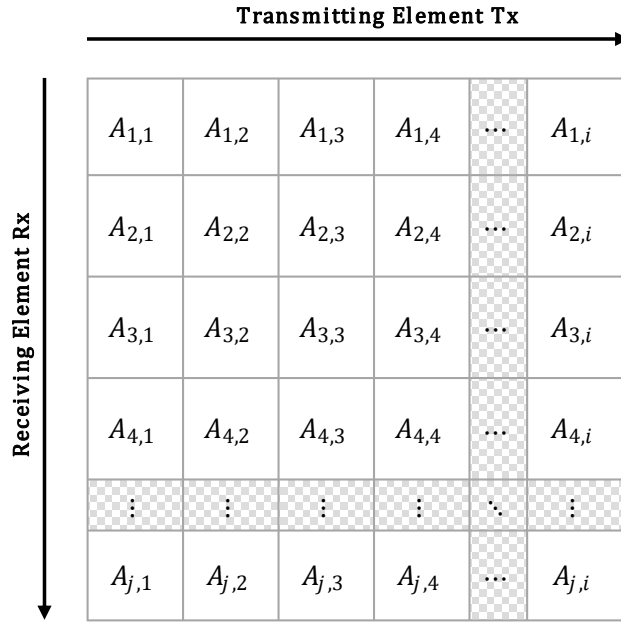


Figure 2.22: Data matrix obtained through FMC acquisition, with each element A describing a time signal for transmit element i and receive element j

2.5. Advanced Ultrasonic Imaging

Various methods exist outside conventional PAUT for imaging using FMC data, each possessing unique advantages [123, 124]. This section will outline the theory and process behind various imaging algorithms that can be applied to FMC data, in addition to delay law calculation methods and data representation techniques.

2.5.1. The Hilbert Transform

An unwritten requirement for any ultrasonic imaging algorithm is the use of the Hilbert transform. This transform is a singular integral which can operate on a function of a real variable to generate an analytic signal. The discrete Hilbert transform [125, 126] allows this to be calculated for a discrete time series, such as an ultrasonic A-scan.

Considering a real discrete input sine function $a(t)$ defined in equation (2.24), the Hilbert transform $\mathcal{H}[a(t)]$ introduces a $\frac{\pi}{2}$ radian phase-shift for all frequency components of $a(t)$, as shown in (2.25).

$$a(t) = \cos(2\pi ft) \quad (2.24)$$

$$\mathcal{H}[a(t)] = i\cos\left(2\pi ft - \frac{\pi}{2}\right) = i\sin(2\pi ft) \quad (2.25)$$

This result is a complex value $\hat{u}(t)$ with a real component equal to $a(t)$ and an imaginary component equal to its Hilbert transform, demonstrated in (2.26).

$$\hat{u}(t) = a(t) + i\mathcal{H}[a(t)] = e^{i\cos(2\pi ft)} \quad (2.26)$$

This complex value is the analytic signal, and is defined as having no negative frequency components. However, for the purposes of imaging with ultrasound, it allows a signal envelope $|\hat{u}(t)|$ to be obtained.

$$|\hat{u}(t)| = \sqrt{a(t)^2 + \mathcal{H}[a(t)]^2} \quad (2.27)$$

The effect of this envelope is demonstrated in Figure 2.23 for an arbitrary Fourier series, resulting in a smooth signal envelope independent of instantaneous phase.

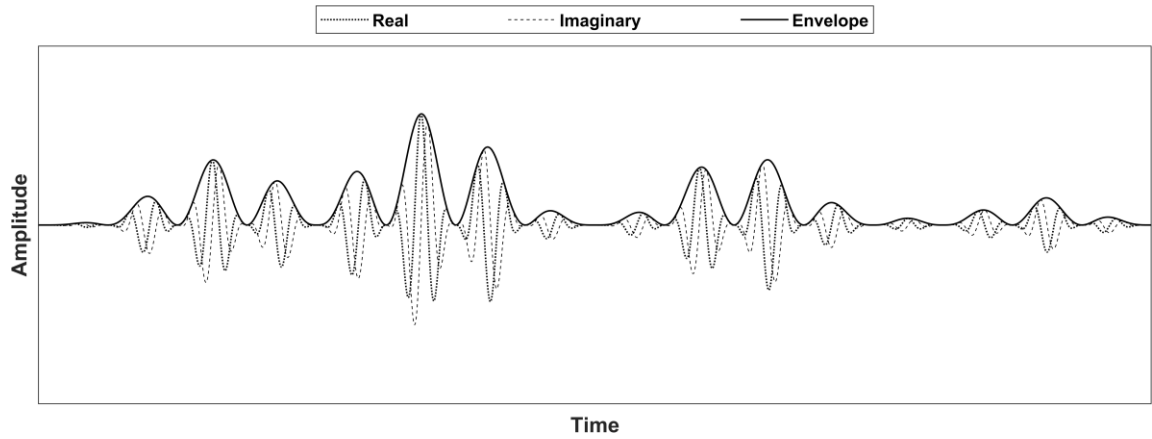


Figure 2.23: (a) real, (b) imaginary components and (c) envelope of signal after calculation of Hilbert transform

Therefore, the Hilbert transform is particularly useful when processing ultrasonic data for imaging. Figure 2.24 shows an image of a SDH generated using the Total Focusing Method, both with and without computing the Hilbert transform. The analytic signal generated from the Hilbert function allows a smooth depiction of the response. This reduces interpretation errors, as the intermittent response of the non-analytic signal image may be mistaken for or mischaracterised as a multi-faceted crack or porosity. For image generation throughout this work, the Hilbert transform is computed as standard unless stated otherwise.

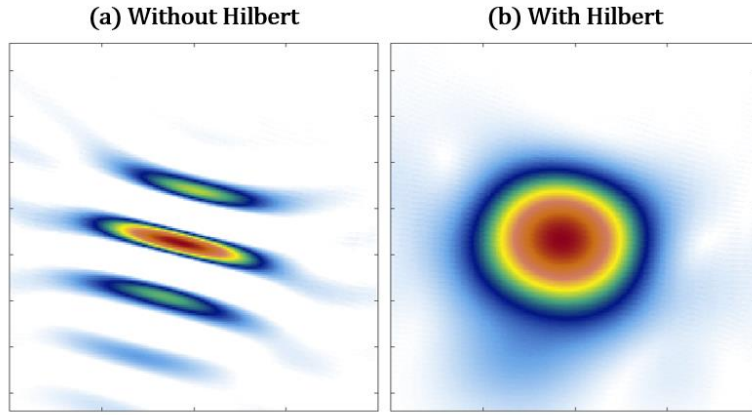


Figure 2.24: TFM imaging (a) without and (b) with the Hilbert transform

In practice, it is necessary to compute the signal envelope after the imaging process is complete, such that phase information is retained during focusing. This means that a complex analytic image is formed during image processing, containing real and imaginary components I_{real} and I_{imag} respectively. The magnitude of this image then computes the signal envelope image $I(x, z)$, as defined in (2.28).

$$I(x, z) = \sqrt{I_{real}(x, z)^2 + I_{imag}(x, z)^2} \quad (2.28)$$

2.5.2. Amplitude Imaging Methods

There are a number of amplitude based imaging techniques for post-processing of FMC data, including the wavenumber algorithm [127], time reversal [128] and Virtual Source Aperture (VSA) [129]. However, it is the Total Focusing Method (TFM) [122, 130] that is considered the ‘gold standard’ of FMC imaging techniques. This performs a synthetic-focusing of the full array aperture at every point in a discretised region of interest, resulting is a fully focussed image in transmission and reception – hence the title of

‘total focusing’. An example of this full aperture focusing for a narrow gap weld inspection is shown in Figure 2.25.

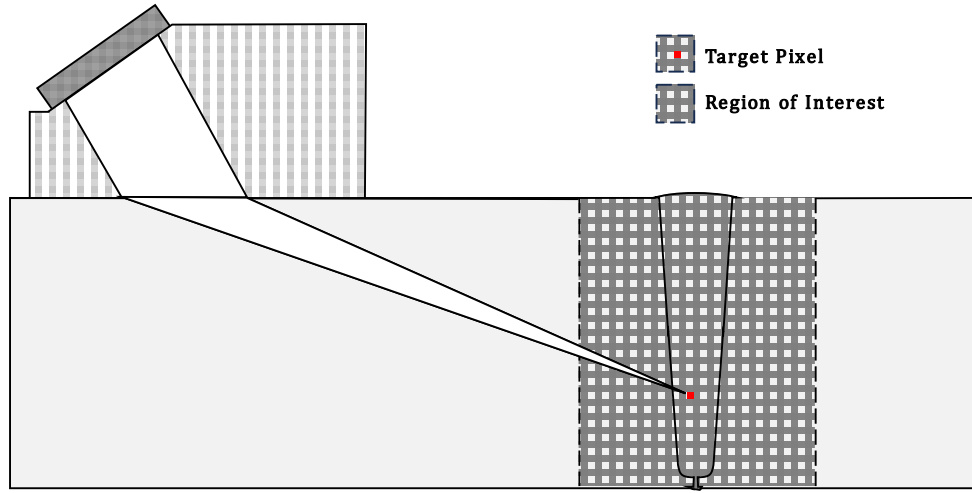


Figure 2.25: Full aperture focusing of TFM algorithm on a discretised image region

The processing involved in the TFM algorithm is much greater than with standard PAUT techniques. This is in part due to the extensive synthetic focusing involved, but also due to the large quantities of computational memory and data manipulation required. The following expression describes the TFM algorithm for an FMC dataset for which the Hilbert transform $\hat{u}(t)$ has been computed. Considering a transmitting element tx and receiving element rx , the image value at (x, z) is the amplitude value of their corresponding A-scan $\hat{u}_{tx,rx}(t)$ at a time equal to the sum of travel times τ_{tx} and τ_{rx} from the image point to the transmitting and receiving elements respectively. The total image is formed by the sum of each element pair for N_{tx} transmitting and N_{rx} receiving elements, at each point in the image.

$$I_{TFM}(x, z) = \sum_{tx=1}^{N_{tx}} \sum_{rx=1}^{N_{rx}} \hat{u}_{tx,rx}(\tau_{tx}(x, z) + \tau_{rx}(x, z)) \quad (2.29)$$

For a 64-element array, there are 64^2 A-scans to be indexed based upon travel times at every image point. For a modest 100 x 100 pixel image, nearly 41 million individual computations are required to form a single image. However, despite the increased computation required, TFM has several advantages over traditional PAUT techniques. The most obvious benefit is the ability to focus at every discrete point in an image, which has shown to radically improve resolution relative to traditional imaging methods [122]. Additionally, improved spatial resolution, geometric and wave speed correction ability, and reduced dead zones give TFM an advantage over PAUT.

Calculation of the travel times required for image generation need only be generated once pre-inspection. Various methods exist for doing this, which are discussed later in this chapter. Advanced travel time calculation has enabled the introduction of the Multi-Mode TFM (MM-TFM) [131-133], utilising consideration of boundary reflections and mode conversions to expand image quality and field of view. Vector TFM (VTFM) also considers reflector orientation as well as travel time to improve defect orientation determination [134].

Commercially, TFM has begun to make its way into phased array controllers, including Olympus' OmniScan™ X3 64 [135], Sonatest's Veo³ [136], and Zetec's TOPAZ® 64 [137]. Furthermore, advancements in international testing standards [138] have led to the adoption of TFM as a standardised inspection technique in industrial processes.

2.5.3. Phase Imaging Methods

Amplitude-based methods do not negate the phase of a received signal. However, Phase Coherence Imaging (PCI), also considers the phase coherence of returned signals. This combines the advantages of phased array with that of TOFD. Despite no official standard currently existing, purely phase driven imaging has grown in prominence - particularly for crack-detection and monitoring [139, 140].

There have been several NDT methods proposed for the computation of a phase-based image. Initially, phase-weighted TFM imaging was introduced with the Sign Coherence Factor (SCF) and Phase Coherence Factor (PCF) by Camacho *et al* [141], followed by the Vector Coherence Factor (VCF) by Cruza *et al* [142]. The SCF is the most computationally efficient method, as the coherence factor is computed based on the sign as an approximation of the phase. The formation of a TFM image weighted by the SCF is defined in (2.31).

More generally, PCI has begun to reference purely phase-based imaging. The amplitude free nature of PCI reduces the effect of attenuation on imaging performance, and has been shown to increase sensitivity to diffractive effects, relative to amplitude-based algorithms [139]. This improves flaw sizing, where amplitude drop methods can provide unreliable results. PCI calculation has also been shown to allow reduced data transfer and processing times, due to the ability to binarize data using a single bit sample method [143].

An example of the amplitude and phase of simulated A-Scans containing Gaussian pulses with added random noise is shown in Figure 2.26(a) and (b) respectively. The phase coherence of the pulses is clear to see on the right of the figure, with the random noise exhibiting no coherence across the A-Scans. Over large A-Scan datasets such as FMC, the phase contributions of the random noise will sum to zero, whereas the coherent pulse phase will sum to a maximum. This is the principle of the PCI algorithm.

Figure 2.26(c) shows that phase coherence is conserved when considering only the sign of the A-Scan, rather than the full phase value. In this work, a sign-based PCI algorithm is used. This reduces required computation by eliminating the need to calculate the phase value, and increases the algorithm speed with negligible compromise in image quality.

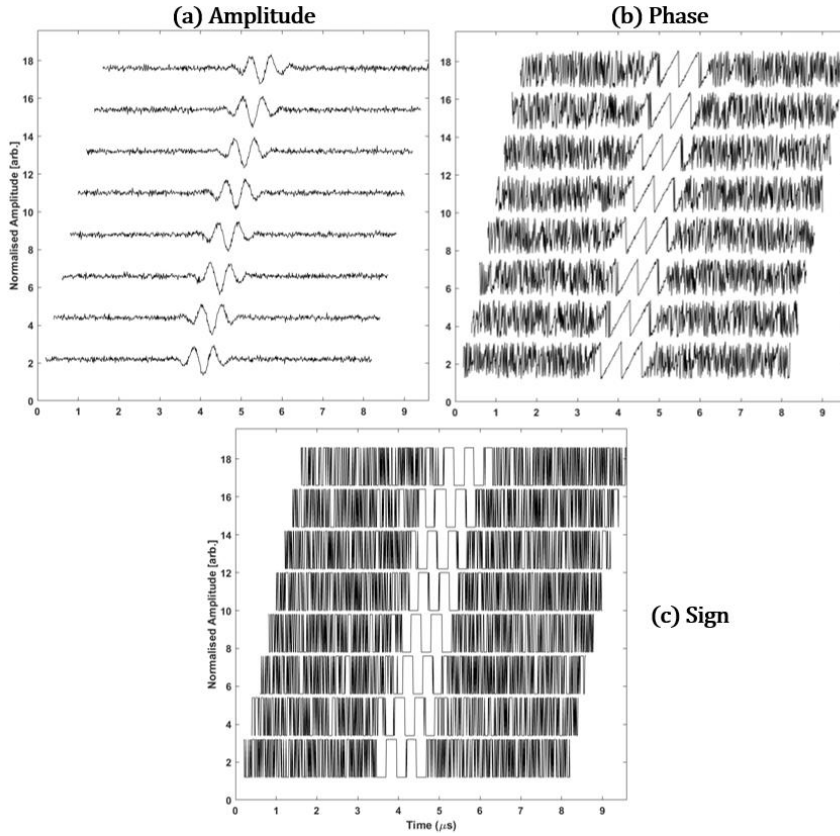


Figure 2.26: Visualisation of Gaussian pulse based on (a) amplitude, (b) phase and (c) sign

The PCI algorithm considers the sign of a sample in the FMC dataset $\hat{u}_{tx,rx}(t)$, which is replaced by a binary value $s_{tx,rx}(t)$ describing the amplitude sign. Equation (2.30) demonstrates that the resulting image is processed similarly to TFM, where each pixel's value is the sum of the binary coherence values of each transmit-receive element pair. Signals from reflectors will demonstrate phase coherence at a given pixel (x, z) , and approach a full coherence value of M or $-M$, given M A-scans used to form the image. Randomly distributed noise will be incoherent across the dataset and approach zero.

$$I_{PCI}(x, z) = \sum_{tx=1}^{N_{tx}} \sum_{rx=1}^{N_{rx}} s_{tx,rx}(\tau_{tx}(x, z) + \tau_{rx}(x, z)) \quad (2.30)$$

$$I_{SCF}(x, z) = I_{TFM}(x, z) \cdot I_{PCI}(x, z) \quad (2.31)$$

The PCI benefits from large element numbers, such that the resolution of coherence between coherent and incoherent signals is increased. Furthermore, heightened sensitivity to diffractive effects can benefit the detection of LOSWF defects in both pulse-echo and through-transmission views.

2.5.4. Imaging Modes

The wave mode – whether longitudinal or shear - of an image is an important aspect to consider both before and during an inspection. The mode choice will influence the path travelled by the wave, and eventually the angle at which it interacts with a region of interest. The direct longitudinal mode is the most commonly used for contact inspections, as the longitudinal wave travels fastest and is therefore often the first and most distinct single observed.

Many weld inspections consider shear waves, primarily as they have a larger refraction window (see section 2.3.2 on waves at boundaries) for angled inspection. Furthermore, they have a smaller wavelength due to reduced velocity, and therefore often provide better resolution of small defects.

Backwall skips and mode conversions can also be taken into account. A wave mode that considers no skips or mode conversion is called a direct mode, and travels from the sample entry point directly to the area of interest. A half-skip mode considers a wave that reflects once off the backwall before entering the region of interest. Finally, a full

skip mode wave would reflect twice – once off the backwall and once off the front wall – before reaching its target. These are shown visually in Figure 2.27.

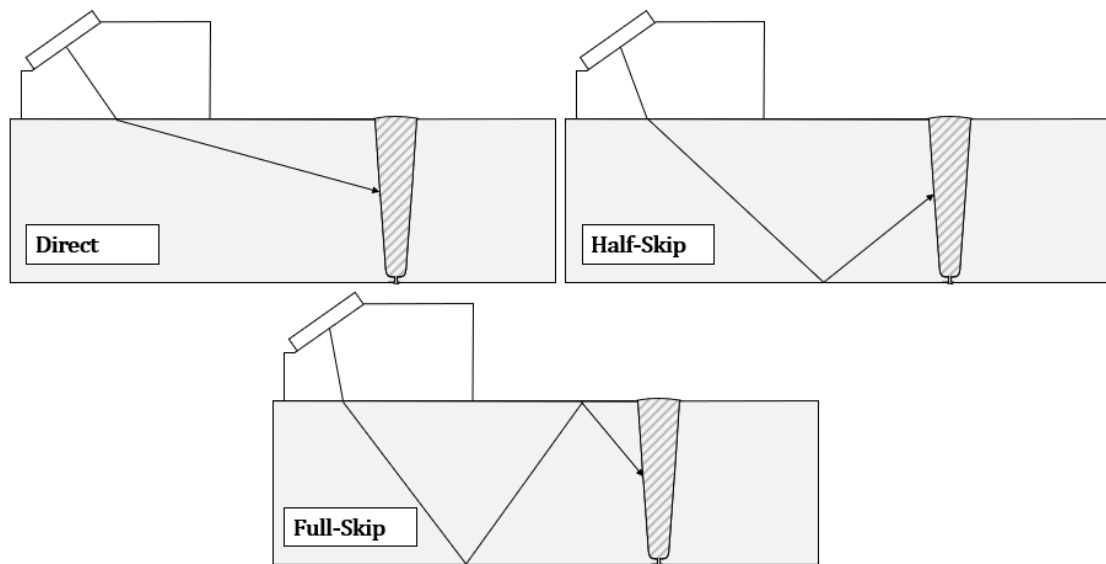


Figure 2.27: Wave path considerations and terminology

In addition to the reflective path of a wave, mode conversions can be considered. This is done by splitting the path into ‘legs’. For instance, a wave which is transmitted longitudinally into the sample, and mode converted to a shear wave from the backwall before reaching its target, would be given the descriptor ‘LT’. A number of first and second order wave modes are shown in Figure 2.28.

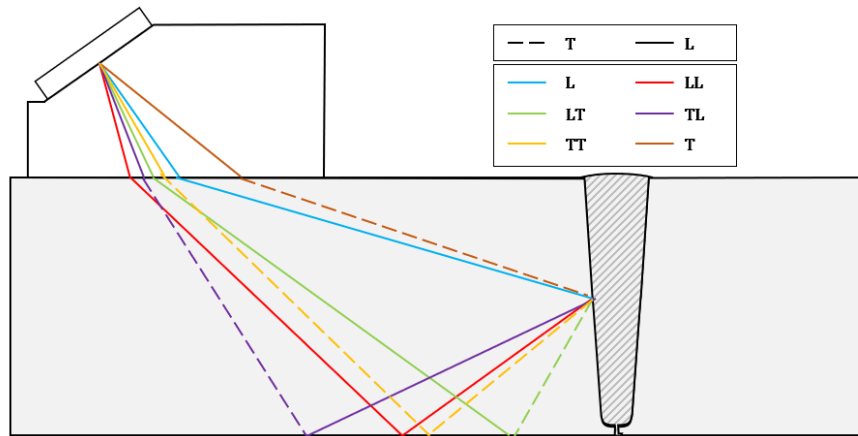


Figure 2.28: Wave mode visualisation

Each of these descriptors is defined for transmission and reception – that is the paths before and after encountering a potential defect in the region of interest. An example of a longitudinal half-skip inspection would be described as ‘LL-LL’, with a dash to separate transmission and reception. This is also sometimes seen with the dash replaced by a ‘d’ (e.g. LLdLL).

There is a clear importance for accurate wave mode selection, given the orientation of a potential defect. A number of quantitative measures have been proposed to determine the best mode pre-inspection. One such commercial method is the Acoustic Influence Map (AIM) introduced by Evident (formerly Olympus) [144], which uses a semi-analytical model to generate sensitivity maps for a given region and defect using TFM.

2.5.5. Delay Law Calculation Techniques

Due to the extensive post-processing focusing required in advanced ultrasonic imaging algorithms, the calculation of delay laws can be a computationally intensive process. This is typically done in accordance with Fermat’s principle, which states that the path

taken by a ray between two points is the path with the shortest ToF [145]. In order to perform post-FMC focusing, this ToF must be calculated for every element pair in the acquired dataset.

2.5.5.1. Pythagorean

The simplest form of delay law calculation is by using the Pythagorean theorem. This is typically the preferred method when considering the simplest forms of inspection, with an array in contact with a homogenous isotropic specimen.

Figure 2.29 shows a linear array in contact with a specimen, with transmitting element Tx and receiving element Rx . For a focal point at (x, z) , the ToF value $\tau_{tx,rx}$ is defined as the sum of the transmit and receive legs, given a longitudinal velocity c_L as in (2.32). This is repeated for each transmit-receive element pair to generate a full matrix of ToF values.

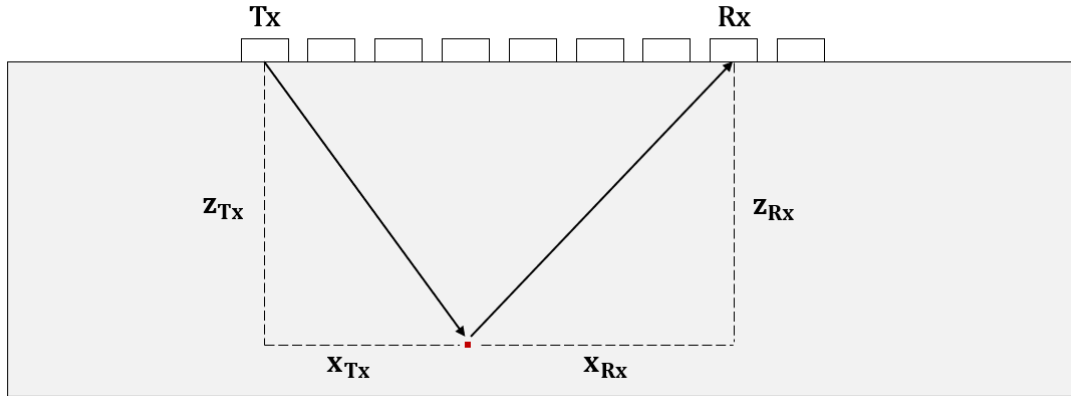


Figure 2.29: Pythagorean method for delay law calculation

$$\tau_{tx,rx} = \frac{\sqrt{x_{tx}^2 + z_{tx}^2} + \sqrt{x_{rx}^2 + z_{rx}^2}}{c_L} \quad (2.32)$$

This method assumes homogeneity and isotropy, and may result in a loss of focus when this assumption is not sufficient. Furthermore, when considering multi-layer media, refraction effects are not taken into account using this method.

2.5.5.2. Eikonal Methods

For multi-layered media, a different ToF calculation solution is required. This can be achieved through a generalised root finding method [146, 147], although these can only practically consider layers of isotropic homogenous materials. For the inhomogeneous case, path finding methods such as A* [148] and Dijkstra [149] algorithms can be used.

Another such method is the Multi-Stencils Fast Marching Method (MSFMM) [150], which is implemented in this work. This is an adaption of traditional Fast Marching Method (FMM) [151] path finding algorithms for computationally solving both the non-linear Eikonal equation and wider static Hamilton-Jacobi equations. The MSFMM has shown to reduce errors relative to traditional FMM methods [152] by considering all nearest neighbours of a discrete point . Given a known transmitter $t_{x,y}$ within a discretised velocity field $V(x, y)$ describing the domain $I(x, y)$, the minimum travel time $\Delta\tau$ to the point $(x_i, y_i) \in I$ can be found using an upwind finite difference scheme shown in (2.33).

$$|\Delta\tau(x_i, y_i, t_{x,y})| = \frac{1}{V(x_i, y_i)} \quad (2.33)$$

The MSFMM can be and has been used with ultrasonic NDT methods for the calculation of travel-times in both isotropic [153-155] and anisotropic [156, 157] materials. Due to the efficiency of the MSFMM, and the ability to compute multiple elements in parallel,

its use for the calculation of ToF maps for use with advanced ultrasonic phased array techniques is clear. Irregular geometries and non-planar interfaces can be easily modelled, and accurate path finding calculated. An example of such a geometry is shown in Figure 2.30.

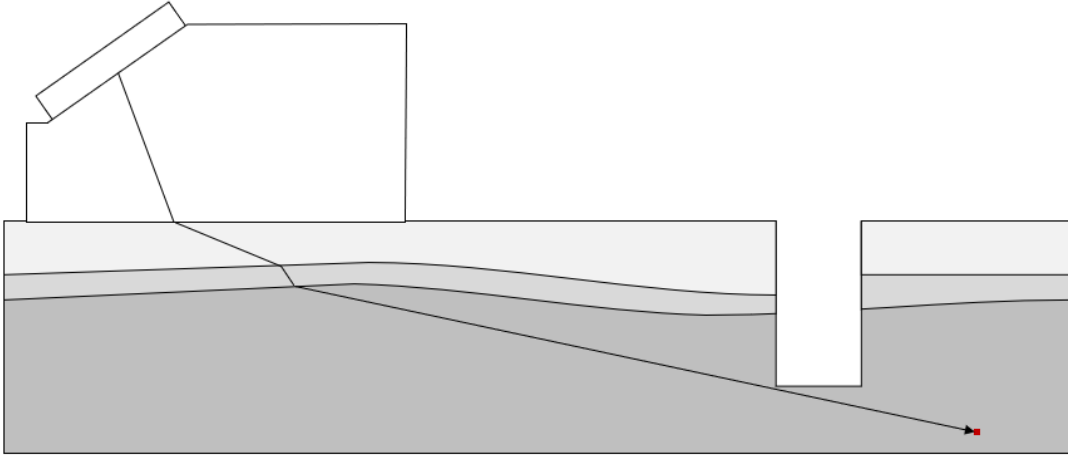


Figure 2.30: ToF calculation through multiple non-planar surfaces with irregular geometry

Furthermore, as only the velocity field $V(x, y)$ and source positions $t_{x,y}$ are required, the MSFMM can be easily adapted to consider materials with changing material properties, whether due to microstructure or temperature variations, as shown in Figure 2.31.

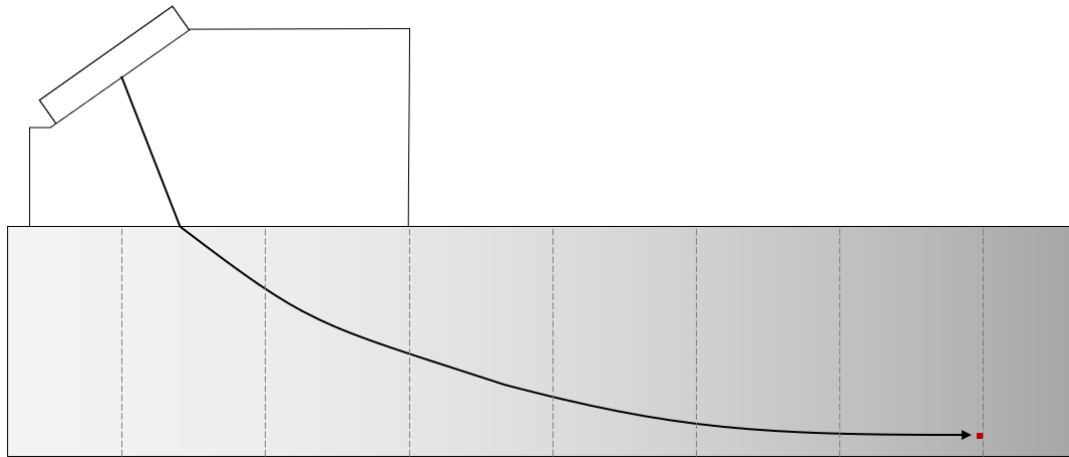


Figure 2.31: ToF calculation through changing material properties (note that effects are exaggerated)

2.5.6. Data Fusion

Data fusion is an important aspect to consider for reducing operator decision-making time, particularly with the generation of large number of images. Reducing large datasets into a single image can reduce analysis time and mitigate the risk of overlooking or misrepresenting data.

Improving the representation of data for this purpose is already fundamental to phased array inspection. The B-scan is an example of fusing A-scan data together to display data in a simpler and more interpretable way. Similarly, the C-scan collates several ultrasonic B-scans or cross-section images into a representative view of a full scan based on time gates.

However, the process of data fusion is typically considered as the method of superimposing multiple datasets, rather than the ‘stacking’ method seen in the B- and C-scan. Examples of such techniques include the fusion of ultrasonic B-scans with Eddy

current data [158, 159] and displaying several MM-TFM images in a single representation [160].

A number of methods can be applied to achieve this fusion, such as a matched filter approach for fusion of multi-mode TFM images in characterising crack-like defects [160, 161]. This has been shown to remove the requirement for prior defect knowledge, while providing statistical analysis of mixed modes to produce a single image showing the full extent of a defect. Fusion has also been approached from a machine learning perspective, with the goal to improve performance and accuracy of multi-mode immersion imaging [162].

2.5.7. Image Performance Indicators

To quantify the quality of a given ultrasonic image, a number of parameters have been proposed and utilised. These include SNR and the Array Performance Indicator (API). These are particularly useful for research purposes, in order to compare and benchmark advancements in imaging algorithms or ultrasonic equipment against standard practices, and in industrial inspection settings for equipment and amplitude calibration procedures.

2.5.7.1. Signal-to-Noise Ratio

SNR is perhaps the simplest and most commonly used metric for determining the quality of an ultrasonic signal or image. This is typically represented in a logarithmic format, in decibels (dB). For a voltage V_s induced by scatter from a reference reflector or defect, the SNR is calculated as shown in (2.34), for a noise voltage V_n [128].

$$SNR = 20 \log_{10} \left(\frac{V_s}{V_n} \right) \quad (2.34)$$

Selection of the noise voltage value can be done using a number of methods. However, this is typically done by considering the Root-Mean-Square (RMS) of a signal portion $S(\Delta t)$ corresponding to a reflector-free region, as shown in Figure 2.32.

$$V_n = \sqrt{\langle S(\Delta t) \rangle^2} \quad (2.35)$$

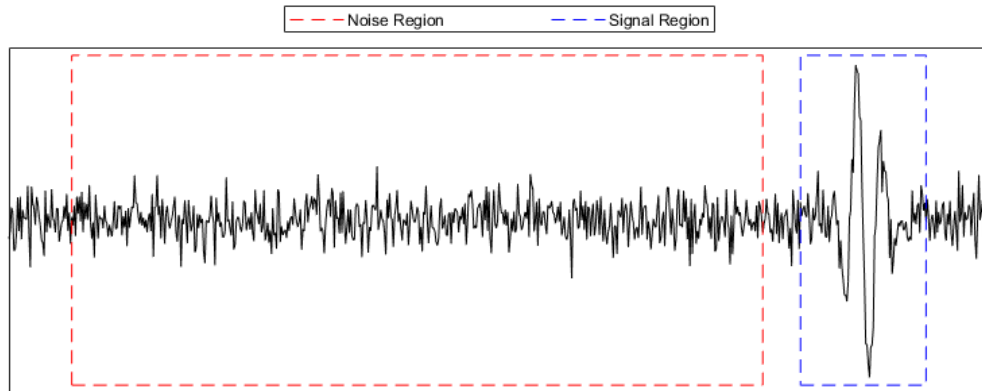


Figure 2.32: Noise (red) and signal (blue) regions considered for calculation of SNR

Standard calibration of equipment prior to inspection often requires the noise of a signal to be quantified in this manner. For example, the SNR is used to check the dynamic range of ultrasonic instrumentation at maximum gain relative to standard criteria [163]. Furthermore, ultrasonic probe calibration requires the calculation of the SNR of a reference reflector, to ensure sensitivity variation between elements does not exceed ± 3 dB (for standard linear array) [164].

2.5.7.2. Array Performance Indicator

The API [122] is an indicator useful for comparing the Point Spread Function (PSF) of different ultrasonic imaging methods. This quantifies the imaging performance based on

the ability of the system to resolve a point-like scatterer. A low API value indicates that the indication approaches a single point, while a larger API indicates spreading of the scatterer response and generally a reduced imaging performance. The dimensionless indicator considers both the wavelength of ultrasound in the medium λ , and the area A_{-6dB} at which the point scatterer response is greater than -6dB.

$$API = \frac{A_{-6}}{\lambda} \quad (2.36)$$

An example of the use of API is shown in Figure 2.33, for two 3.0 mm SDHs at different depths. TFM images generated from an array placed directly above each hole is shown. The deeper SDH has a larger PSF, as can be seen by lateral spreading. Therefore, the shallower SDH has the lower API due to its lower spread function.

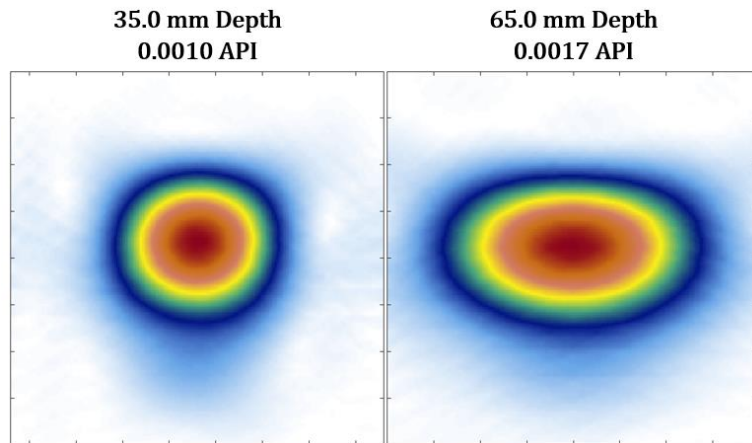


Figure 2.33: API Values of two 3.0 mm SDH at 35.0 mm (left) and 65.0 mm (right)

2.5.7.3. Amplitude Fidelity

The Amplitude Fidelity (AF) is a measure of the maximum amplitude variation due to image grid resolution [165]. This is analogous to sample frequency for time traces, and

must be sufficient to resolve the maximum amplitude of a signal in the image. Furthermore, due to the nature of TFM focusing, too coarse a grid could lead to the cancellation of values from A-scan points with an opposite phase, which can lead to inaccurate sizing or missing a defect entirely.

A TFM image of a SDH reflector with various image grid densities are shown in Figure 2.34, with low pixel density values exhibiting poor resolution and amplitude fidelity. Calculation of the amplitude fidelity AF for a grid density Δx is given by the maximum sampled amplitude of the TFM image A_{max} , and the true maximum value of a reflector A_{true} , equal to the maximum value observed on an infinitely fine grid.

$$AF(\Delta x) = 20 \log_{10} \left(\frac{A_{true}}{A_{max}} \right) \quad (2.37)$$

As the grid density is increased, it should be expected that the maximum sampled amplitude should increase towards the true amplitude value. This means that the AF value will approach zero for increasing grid density. Of course, the true value cannot be known, as an infinitely fine grid is not feasible. Therefore the value is estimated based on an oversampled and then finely interpolated TFM image [165]. For the four TFM images in Figure 2.34, the AF is calculated using a true value based on a TFM grid calculated at a density of 500 pixels per wavelength.

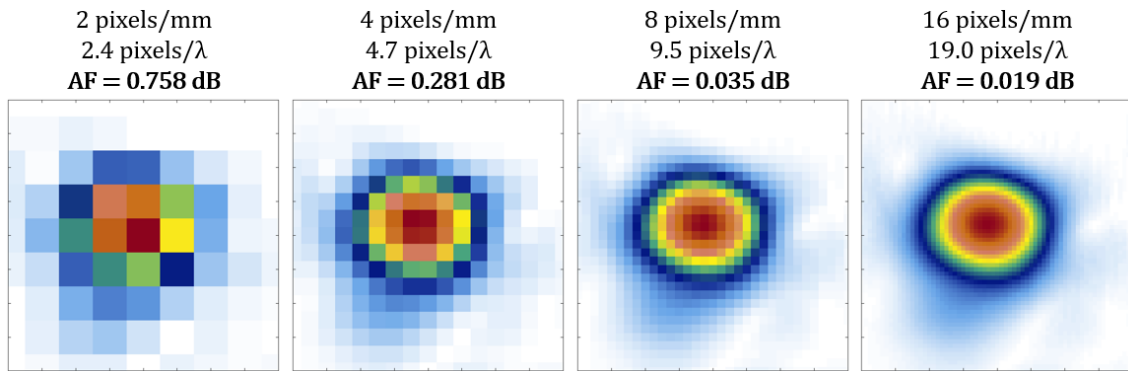


Figure 2.34: TFM amplitude fidelity for increasing pixel density

TFM inspections require the grid density to be calibrated, based upon SDH reference reflectors at three points along the image region [138]. It is important to strike the balance between sufficient AF and oversampling, as this can drastically reduce the imaging rate of TFM inspection. Typically, the pixel size is selected to be around a quarter of the acoustic wavelength used, as beyond this point the image received no additional beneficial information.

2.5.8. Image Colour Palettes

The visual representation of an image is vital to the representation and interpretation of potential defects. In this work, two colour palettes are used – one for amplitude-based imaging such as TFM and SCF, and one for phase-based imaging such as PCI. These are displayed in Figure 2.35.

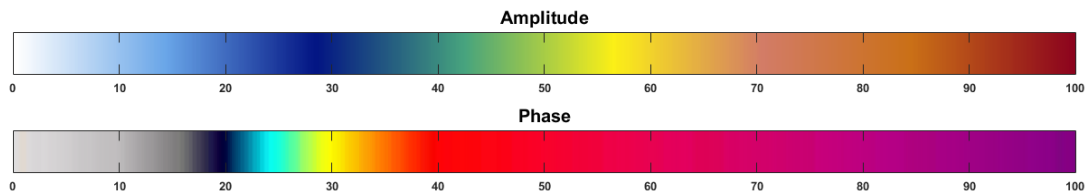


Figure 2.35: Amplitude and phase colour maps

The amplitude palette is designed to distinguish high-amplitude values from low-amplitude values, around a 6 dB (~50%) threshold. Alternatively, the phase palette accentuates high coherence values above 30%. The amplitude and phase colour palettes are based upon that used by the Evident OmniScan X3 64 [135] phased array controller, in the interest of consistency and familiarity with current commercial and industrial products.

2.5.9. Imaging GUI

In order to perform the imaging techniques discussed in this Chapter, a graphical user interface (GUI) for general advanced imaging of FMC datasets was designed. This was constructed in MATLAB, and encompasses the definition and positioning of ultrasonic probes, filtering and processing of FMC data, ToF calculations using the FMM, imaging using TFM, and subsequent imaging analysis. The interface is shown in Figure 2.36, presenting a three-dimensional representation of the ultrasonic setup.

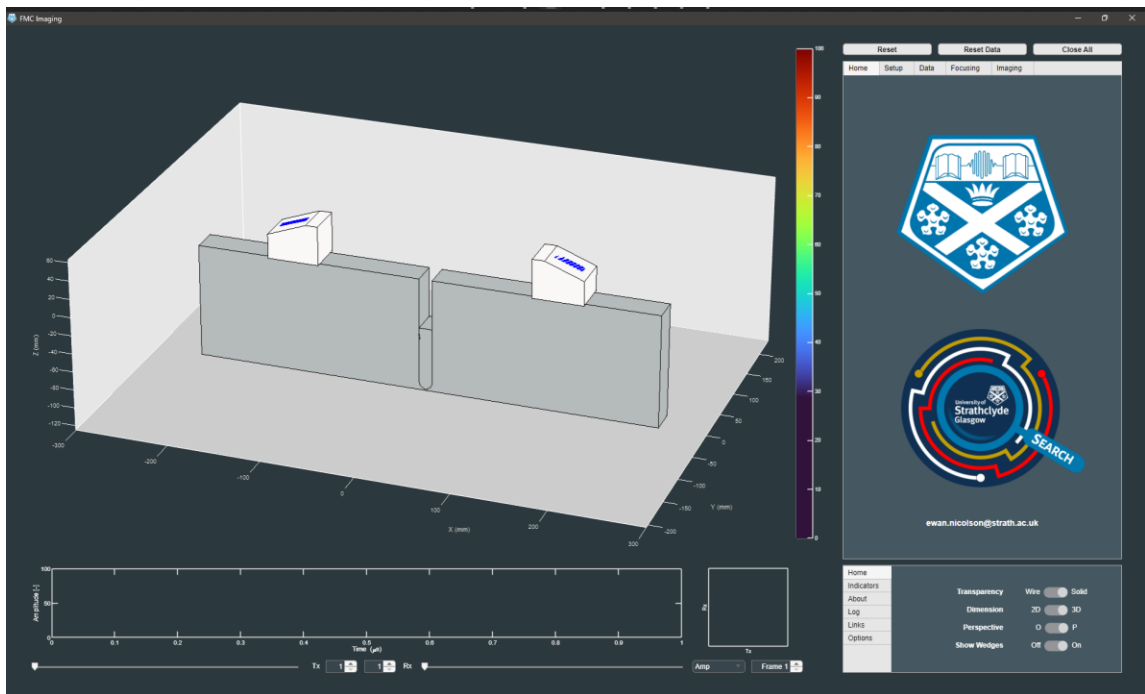


Figure 2.36: MATLAB GUI interface showing tool tabs on the right hand side, three-dimensional ultrasonic setup window on the left, and FMC data visualisation along the bottom

The tabs to the top-right of the interface separate the image generation process into four stages. The first of these is the image “Setup”, in which the array, wedge and couplant used can be defined through loading of configuration (*.CFG) files. Furthermore, test piece geometry and material can be defined, as well as probe positioning, known notches or holes, and weld geometry.

The “Data” tab allows the loading of FMC data from a number of file formats, including standardised *.MFMC files, as well as custom *.PNG, *.MAT and *.TXT files. The subsequent filtering and processing of this data can also be done, with customisable frequency windowing, integrity checks and visualisation. In the case of datasets acquired using coded excitation, pulse compression is also handled. This will be relevant for the work outlined in Chapter 5.

The “Focusing” tabs handles the calculation of ToF data, based on the information defined in the setup tab and a desired grid density. ToF maps can be calculated for a list of defined modes using either a Bisection, MSFMM, or Pythagorean method depending on complexity. Velocity maps required for MSFMM calculation can be loaded based on temperature gradient or microstructure maps.

The final “Imaging” tab handles the generation of images of the defined inputs. The data used to generate the image can be defined, such that SAFT, half-matrix capture, sparse data and sliding window techniques can be applied. The algorithm required can be selected and run using CPU or GPU processing. Once the image is generated, a variety of analysis tools, such as sensitivity calculations, performance indicator calculation and normalisation alterations can be performed.

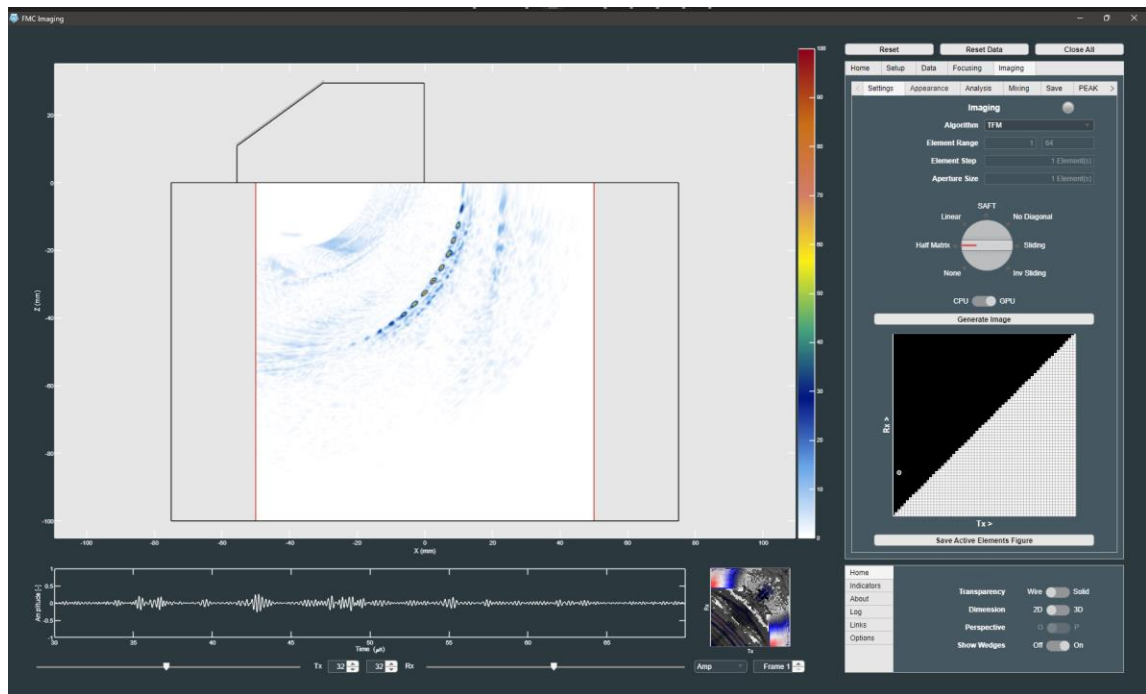


Figure 2.37: GUI showing TFM image of SDH in standard calibration block using half-matrix capture from data obtained using an Olympus 55SW wedge and 5 MHz probe

The GUI was designed in order to provide a consistent imaging process for dependable analytical comparisons between multiple datasets, as well as improving ease of use. The repetition of complex processes such as ToF calculation and data loading are removed, as is often seen with script-based imaging processes, allowing efficient data analysis. This was used to generate images and provide analysis in all work presented in this thesis, and has proven a valuable tool throughout the completion of this engineering doctorate.

Chapter 3

Tandem Phased Array Imaging

3.1. Introduction

Inspection practices for typical V-groove welds are well practiced and standardised. This is typically done with PAUT methods, due to the ability to steer and focus with a defined probe offset. British standards for ultrasonic weld inspection [166] require the incident beam of the probe to interact with the bevel within 6° of the bevel normal. This can typically be achieved using a sectorial scan, or shear half-skip (e.g. TT-TT) TFM. By solely considering shear waves in transmission and reception, an effective reflection can be obtained from a potential LOSWF defect positioned on the weld bevel.

However, when considering narrow gap grooves, an inspection setup is not as straightforward and defined. Due to the near parallel bevels, LOSWF flaws manifest at near-vertical angles, and complicate the inspection procedure required to observe a consistent sensitivity for LOSWF detection. Traditional phased array methods can show improvement using the self-tandem 3T (TT-T) TFM image mode. The use of multi-mode self-tandem imaging has also been shown to be effective using FMC and TFM [167]. However, this relies on achieving a favourable reflected angle from the LOSWF

flaw and can require several scan positions to cover the full weld thickness – particularly in thick-section components. The requirement for a maximum beam deviation of 6° on the bevel also becomes impractical and would require large probe offset distances to satisfy.

As the prominence of narrow gap welding increases, the desire to develop an efficient and reliable inspection method for the testing of narrow gap welded components is in high demand. The work in this chapter will attempt to address this issue by proposing a dual-tandem phased array inspection method. This method introduces a second, opposite facing array on the other side of the weld, designed to alleviate the difficulty in the detection of near-vertical defects. The addition of a second probe not only ensures a consistent detection sensitivity from each weld side, but also introduces the ability to perform through-weld detection. By separating the transmission and reception across two probes, sensitivity to geometric effects - such as diffraction - can be increased, improving the likelihood of detection and reducing sizing errors associated with near-vertical defects. In addition to this, a wedge design balancing the transmission of both longitudinal and shear modes would allow the full benefit of multi-mode TFM to be exploited. Such a wedge would allow longitudinal through-transmission imaging, utilising diffraction effects, while maintaining the ability to perform multi-mode pulse-echo imaging.

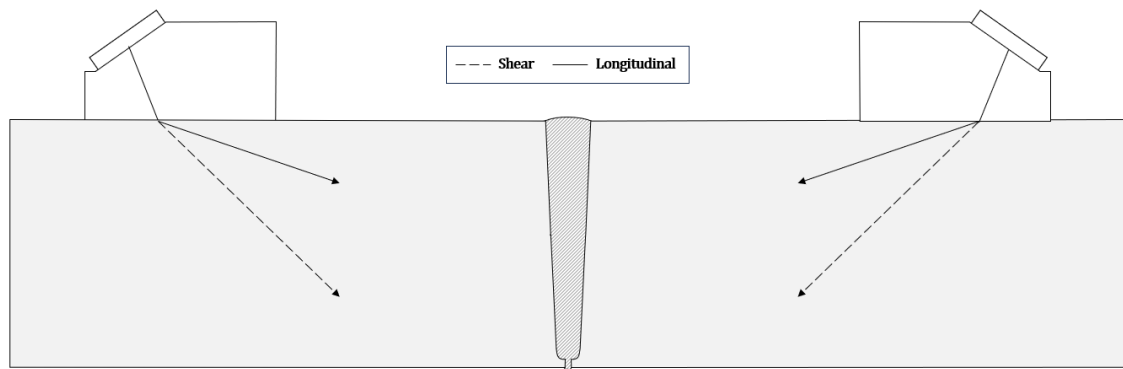


Figure 3.1: Dual-tandem phased array configuration

In recent years, the ability to combine welding and NDT processes at the point of manufacture has grown in demand. An in-process inspection approach enables flaws to be detected and corrected between weld passes, reducing rework, increasing manufacturing throughput, and schedule certainty. However, when considering in-process ultrasonic inspection, several key challenges - including partially-filled geometries, high temperature gradients and process interference - limit deployment. While traditional phased array techniques using high-temperature wheel probes [87, 168] have shown promise in traditional open V-groove weld inspection, such approaches have not yet been considered for narrow-groove welding practices. Therefore, there is a requirement for the design of narrow-groove weld inspection processes for both fully-filled cold welds and partially-filled welds inspected in-process.

In this chapter, the dual-tandem method is introduced and demonstrated as a method for the detection and inspection of near-vertical defects in cold thick section components mimicking fully-filled narrow gap welds. Notches created using an Electrical Discharge Machining (EDM) process were placed within the samples to simulate the positioning expected from a LOSWF defect in a 2° narrow J-groove weld. It will be shown that this

method can provide high sensitivity imaging of near-vertical flaws using multi-mode pulse-echo TFM and longitudinal trough-transmission imaging. Furthermore, the possibility of image mixing will be explored, in order to visualise the full geometric extent of a defect in the two-dimensional image plane.

3.2. Experimental Procedure

The process of determining the presence and geometry of a given defect begins with the acquisition of the full-matrix dataset. However, to acquire an FMC dataset in which transmitted energy is optimised to cover the full weld area, the probe positioning relative to the weld must be considered. Once one or more FMC frames are collected, the data can be processed, and ToF maps calculated, to form the necessary images to assess the presence and extent of potential flaws. This requires consideration of known weld geometries, to determine the correct imaging mode to select to maximise flaw sensitivity. Once images have been obtained, they can be observed separately, or ‘mixed’ to condense the information gathered.

In order to ensure the transmission and reception of both shear and longitudinal modes in a single acquisition, a numerical analysis of Snell’s law was conducted to identify an optimised wedge angle for the probe assembly. This considered the ability of the assembly to transmit and receive longitudinal and shear modes in a single acquisition. The refraction angle of the resulting shear and longitudinal modes versus wedge angle were computed and displayed in Figure 3.2.

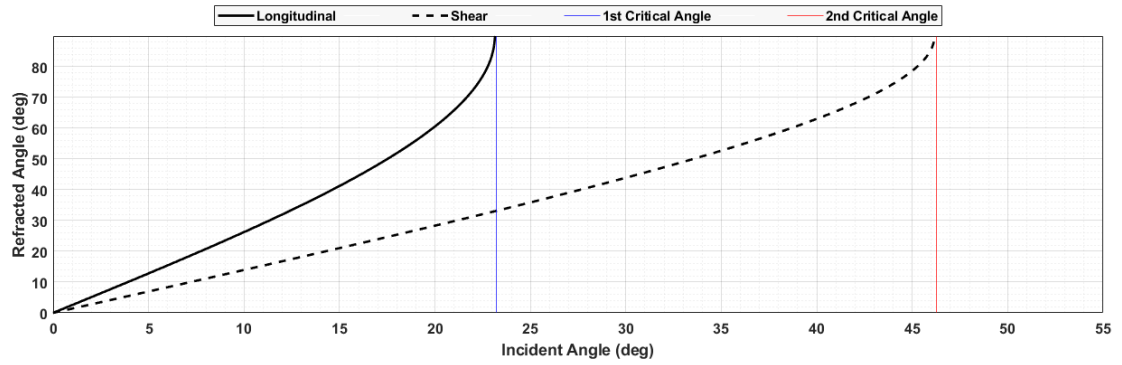


Figure 3.2: Shear and longitudinal refraction angles at a Rexolite-Steel boundary as a function of incident angle

From this study, a wedge angle of 20° was determined to provide a balance between increasing the longitudinal refraction angle towards the first critical angle and limiting the shear refraction angle. This provided refraction angles of 60° and 28° relative to the surface normal for longitudinal and shear waves respectively, across a Rexolite ($v_L^R = 2330 \text{ ms}^{-1}$ [169]) wedge to carbon steel ($v_L^S = 5940 \text{ ms}^{-1}$, $v_T^S = 3220 \text{ ms}^{-1}$ [76]) interface.

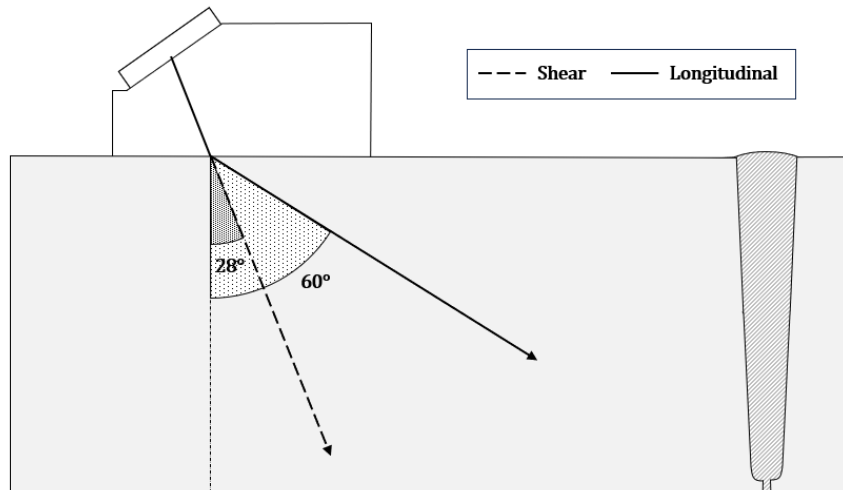


Figure 3.3: Longitudinal and shear refraction angles using 20° Rexolite wedge into steel

The equipment used throughout the work in this chapter is therefore as follows:

- 5 MHz 64-element Olympus A32 arrays (0.50 mm pitch, 0.42 mm element width, 10.0 mm elevation)
- 60LW Rexolite Olympus A32 wedges (20° angle)
- PEAK-NDT MicroPulse 6 128/256 channel array controller

The 5 MHz probe used here is representative of a standard weld inspection phased array, however, only a 0.5 mm pitch array was available. Ideally, an increased pitch would be beneficial - a greater element width would improve energy transmission, and a larger inter-element spacing would improve beam coverage.

This section will introduce the background required for the work in this chapter, starting with the acquisition process, then ToF map calculation, adapted TFM imaging algorithm, multi-view and multi-mode image mixing, and finally an image sensitivity calculation method.

3.2.1. FMC Acquisition

With the inclusion of two phased array probes, the FMC acquisition process increases in complexity. Considering the two individual arrays as a single aperture, the full matrix dataset can be obtained at a size 4x greater than that for a single probe. For two arrays of N elements each, a dataset of $4N^2$ A-scans is obtained.

This Dual Aperture FMC (DAFMC) dataset can be split into four sub-datasets of size N^2 , each of which will be referred to as an individual ‘view’ available to the system. An example of the full matrix dataset obtained can be seen in Figure 3.4. This assumes that elements 1 to N belong to the left array, and elements $N + 1$ to $2N$ to the right array.

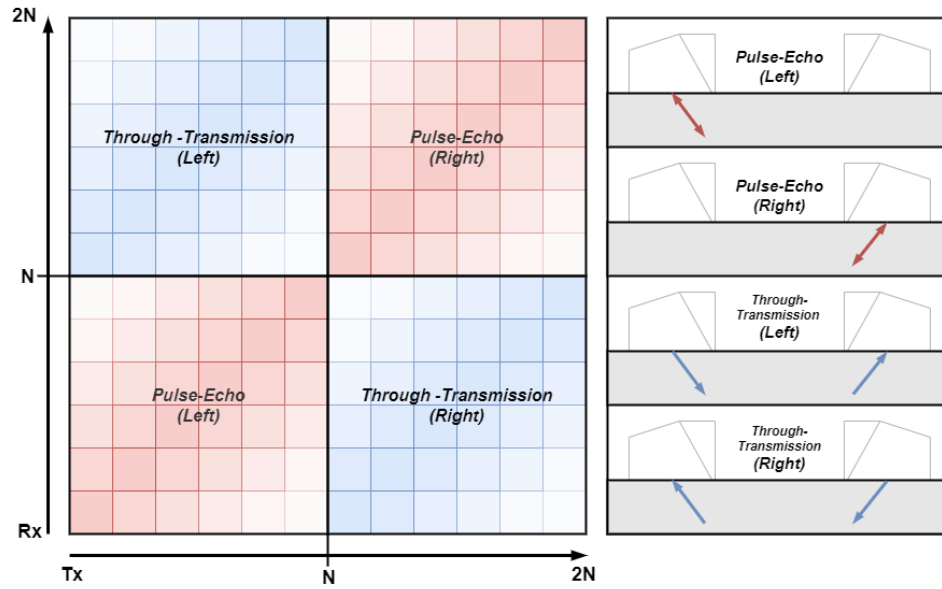


Figure 3.4: Full matrix obtained from dual tandem FMC, showing four unique views

This means that from a single acquisition, a full dataset containing the two pulse-echo and two through-transmission views can be collected, to be analysed with post-processing imaging techniques.

Throughout this work, consistent scan parameters were used in the DAFMC acquisition process. These are detailed in Table 3.1. The data acquisition was conducted using software designed in National Instruments LabVIEW [170], to interface with the PEAK NDT array controller. Data was saved in a HDF5 Multi-Frame Matrix Capture (MFMC) file format [171], and subsequently processed in MATLAB-based imaging software [172].

Table 3.1: FMC acquisition parameters

	Unit	Value
PRF	<i>kHz</i>	<i>1</i>
Sample Frequency	<i>MHz</i>	<i>25</i>
Excitation	<i>V</i>	<i>200</i>
Gain	<i>dB</i>	<i>60</i>
Time Window	<i>μs</i>	<i>64 - 224</i>

3.2.2. Mode Selection

Six imaging modes were chosen with a mix of mode converted and non-mode converted imaging modes, to allow an understanding of the imaging performance of various modes in both pulse-echo and through-transmission views.

Six pulse-echo modes were selected, including the direct longitudinal mode (L-L) and five self-tandem modes. For through-transmission imaging, only the direct longitudinal mode was used. Of the eight possible self-tandem modes, these five were chosen to provide a variety of mode conversion and propagation angles. As the focus of this work is the enabling and improving of diffraction sensitivity to near-vertical defects, five of the six modes were chosen with a longitudinal mode incident or reflection/diffracted from a defect. A final shear self-tandem (TT-T mode) inspection was also selected to provide comparison to the standard shear self-tandem weld inspection technique. This is described visually in Figure 3.5.

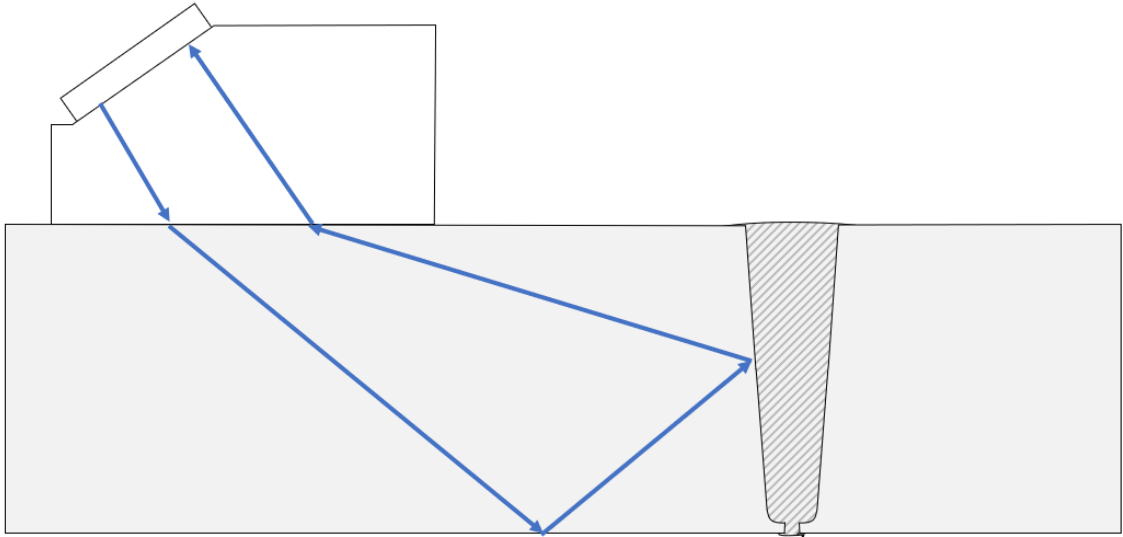


Figure 3.5: Shear self tandem (TT-T) mode, showing skip off backwall on transmission and direct reception

3.2.3. ToF Mapping

To accurately extract the correct amplitude values at each pixel in the discretised image region, a ToF value must be calculated for each array element in the system, and for each image mode. The result is a four dimensional array, of size $X \times Z \times N_T \times M$, where X and Z are the pixel counts along the x- and z-dimensions of the image domain, N_T is the total number of source elements in the system, and M is the number of image modes selected.

As introduced in Section 2.5.5, there are several path finding algorithms for ToF calculation for post-FMC acquisition processing. In this chapter, the MSFMM is used due to the flexibility and efficiency of the algorithm to use with parallel computing solutions [173].

The output of the MSFMM algorithm is a numerical array containing a ToF map for each view - pulse-echo and through-transmission from each side - for every element pair, for each mode. The ToF values generated by a single execution of this algorithm need only be run once and can be used to produce TFM images for any number of FMC frames which possess the same geometric setup, given that material properties can be assumed to remain consistent across each frame.

3.2.4. TFM Algorithm

The algorithm for TFM imaging is largely unchanged from the standard algorithm when approaching the dual tandem method. However, what requires consideration are the DAFMC data and ToF values used to form the image. Views and modes are computed separately. For a DAFMC dataset, computed for three modes, the result is the formation of 12 individual TFM images.

The view considered is defined by the element vectors N_{tx} and N_{rx} . This assumes that N is a vector containing element numbers 1 to N_T , where N_T is the total number of active elements within the system. In this case, two 64-element arrays are used, and as such $N_T = 128$. The element vector required for each view in this case is outlined in the following table.

Table 3.2: Element numbers for each dual-tandem view

	Direction	N_{tx}	N_{rx}
Pulse-Echo	Left	1 - 64	1 - 64
	Right	65 - 128	65 - 128
Through-Transmission	Left	1 - 64	65 - 128
	Right	65 - 128	1 - 64

The TFM algorithm was processed on a Graphics Processing Unit (GPU) using the MATLAB GPU Coder [172, 174]. This creates optimised CUDA C++ code from a MATLAB function. This allowed imaging processing times to be reduced, with an average processing time of approximately one second per 120 mm x 30 mm (600 x 125 pixel with 0.2 mm pixel resolution) TFM frame, using an NVIDIA Quadro T2000 graphics card.

3.2.5. Image Mixing

To condense the number of images produced for analysis, views and modes can be mixed based on the information obtained to produce a single image. This is approached by first categorising images into three groups; (1) images which do not contribute to a defect response, (2) images which display a defect diffraction response, and (3) images which display a defect reflection response. In turn, two mixed images can be created: a diffraction response image I_D and a reflection response image I_R .

Diffraction effects across multiple images will be spatially consistent, so are suitable to mix by a product method. By taking the product of each pixel across multiple images, we can exploit this positional coherence, while suppressing incoherent noise regions. A clear indication of the defect height, by way of top and bottom tip indications, should

therefore be observed. This is achieved using the expression in (3.1) for N images, where I^d is a given TFM image which contributes to diffraction effects.

$$I_D = \prod_n^N I_n^d \quad (3.1)$$

Reflection indications, unlike diffraction effects, are not necessarily spatially consistent across multiple images. This is due to the non-negligible width (1.0 mm) of the notch, as shown in Figure 3.6. Therefore, a combined reflection image I_R is defined as the pixel-by-pixel sum of reflection contributing TFM images as defined in (3.2), for reflection contributing images I^r . Similarly to the diffraction image, this should give us an indication of the width of the defect in the inspection plane.

$$I_R = \sum_n^N I_n^r \quad (3.2)$$

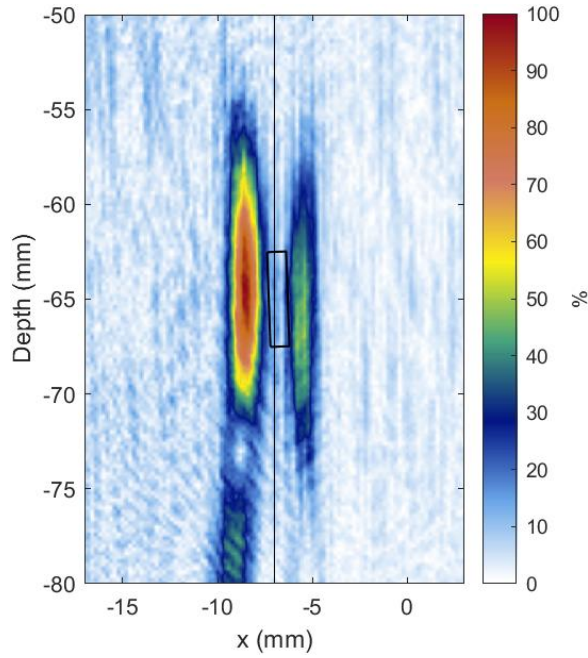


Figure 3.6: Demonstration of incoherent reflections from each LL-T pulse-echo view in sample NG2. This image is created by summing the left and right pulse-echo views, resulting in reflections from each side of the notch being visible.

The result of this is two images, each theoretically displaying the extent of the defect in each dimension in the image plane. By adding the two mixed images, a mixed image which shows the full extent of the defect can be created. This final mixed image I_T , defined in (3.3), is the sum of the two linearly normalised images for diffraction and reflection responses.

$$I_T = \hat{I}_D + \hat{I}_R \quad (3.3)$$

Normalisation to the maximum image pixel value before summation allows the relative amplitudes to be ignored, as diffraction effects are typically much lower in amplitude than reflected responses, and results in a superimposed image.

In this work, this process is done manually by observing each of the image modes and subsequently determining their relevant category. However, this requires prior knowledge of the defect location and geometry, as well as the human interpretation of images. As discussed in Section 2.5.6, there are several statistically informed methods proposed for data fusion which are not explored in this work.

3.2.6. Image Sensitivity Calculations

As discussed in Section 2.5.7.1, the sensitivity of a given TFM image is quantified by its Signal-to-Noise Ratio (SNR). This value is defined as the logarithmic ratio of maximum amplitude $A_{max}(\mathbf{I})$ and the Root Mean Square (RMS) of the noise level $A_{noise}(\mathbf{I})$ of the image domain \mathbf{I} , as expressed in (3.4) [128].

$$SNR = 20 \log_{10} \left(\frac{A_{max}(\mathbf{I})}{\sqrt{\langle A_{noise}(\mathbf{I})^2 \rangle}} \right) \quad (3.4)$$

However, the generalisation of this value, by considering the maximum amplitude of the image, may not give an accurate reflection of the image sensitivity. For instance, artefacts such as wedge and backwall reflections may provide the highest amplitude and therefore falsify the apparent sensitivity of an image.

In this work, where the position and extent of flaws are known well, the SNR value is calculated based upon a defined region around the flaw. The maximum image amplitude is replaced with the maximum amplitude defined within this region \mathbf{r} surrounding the known defect, ensuring that only defect indications are considered. Furthermore, the noise level can be defined in (3.5) as the RMS of the image noise solely excluding the defect indication $A_{noise}(\mathbf{I}_n)$, where $\mathbf{I}_n = \{\mathbf{I}_n \in \mathbf{I}, \sim(\mathbf{I}_n \in \{\mathbf{r}\})\}$.

$$SNR = 20 \log_{10} \left(\frac{A_{max}(\mathbf{r})}{\sqrt{\langle A_{noise}(\mathbf{I}_n)^2 \rangle}} \right) \quad (3.5)$$

This method will be used to quantify the relative sensitivity between images. To retain an accurate relative sensitivity, comparisons can only be made where the image domain and defect regions are of the same area and pixel resolution.

3.3. Test Samples

Three carbon steel samples were created to test the dual-tandem phased array setup, all with dimensions of 120 mm x 500 mm x 35 mm. These were designed to be representative of the thick section components used in the manufacture of pressure vessels. Each sample was cut from the same steel block, and as such consistent elastic properties were observed. The longitudinal velocity was determined to be 5940 ms⁻¹ by considering backwall reflections through the sample z-thickness, with the shear velocity approximated at 3220 ms⁻¹.

Each sample contained one EDM notch of dimensions 5.0 mm by 1.0 mm machined 10 mm into the sample face, along a mock narrow-groove weld face at a 2° rotation to the Z-axis, and placed at depths of 27.5 mm, 60.0 mm and 92.5 mm along the z-axis respectively, to positionally and geometrically represent expected LOSWF flaws throughout the full thickness of a narrow-groove weld. The three samples used in this work are shown in Figure 3.7, presented in the X-Z image plane. The details of the EDM notch defects in the samples are shown in Table 3.3, in terms of x-position, z-position and rotation, relative to the sample vertical.

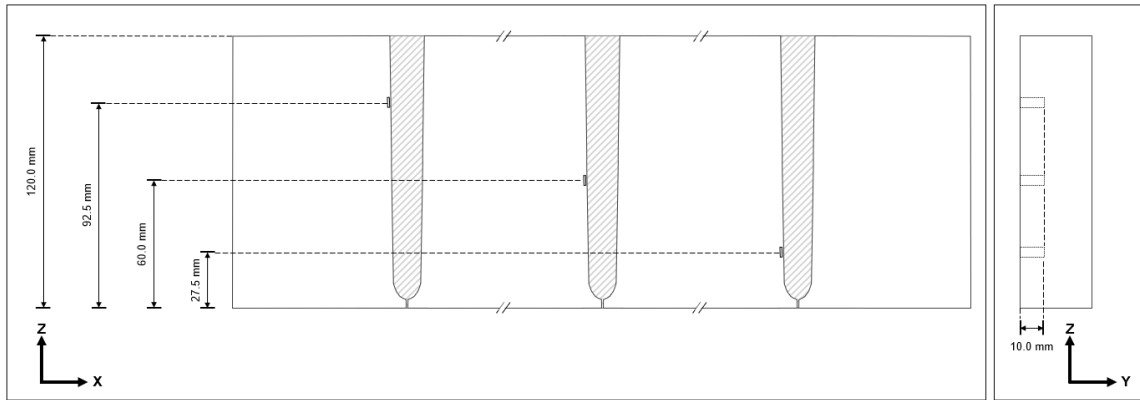


Figure 3.7: EDM notches in carbon steel samples

Table 3.3: Carbon steel samples defect positioning

Ref. Name	Defect		
	X (mm)	Z (mm)	θ (°)
NG1	-7.9	27.5	2.0
NG2	-6.8	60.0	2.0
NG3	-5.6	92.5	2.0

It should be noted that due to the 1.0 mm width of the notches used in this work, there will be a portion of energy reflected from the top surface. This is indistinguishable from diffraction, as the width of the notch is below a single wavelength. Ideally this would be around half of the wavelength to minimise the reflected components. However, machining limitations meant that 1.0 mm was the smallest notch width available.

A photo showing sample NG2 is shown in Figure 3.8. This also demonstrates the two array and wedge system.

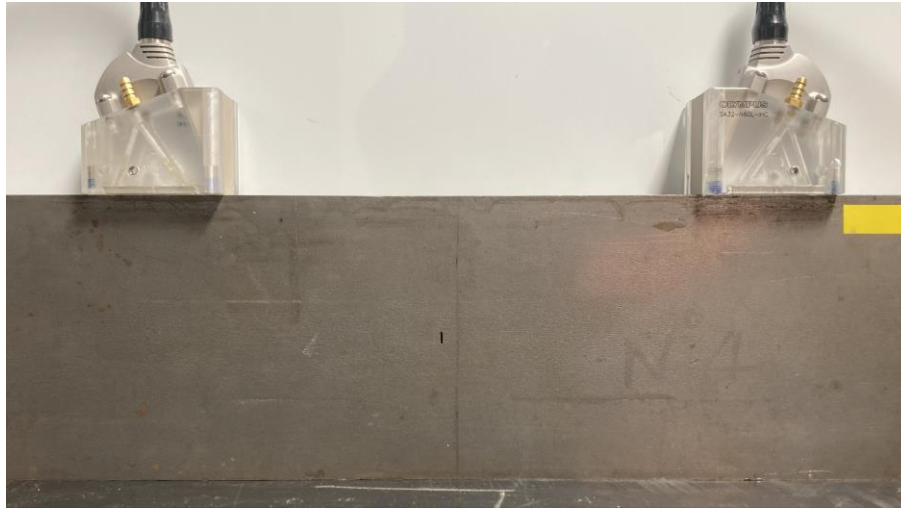


Figure 3.8: Sample NG2 with dual-array setup, showing EDM notch position

3.4. Probe Centre Separation

The separation between the centre of the two arrays, defined symmetrically at the centre of the weld, is a crucial consideration in terms of imaging sensitivity. A Probe Centre Separation (PCS) value must be carefully selected based upon a knowledge of the height of the weld sample, such that the full depth of the weld is covered by the array beam profiles. The PCS value is defined in this work as the centre-element spacing of the two arrays. Assuring this value enables adequate coverage ensures that only a single acquisition is necessary to observe potential flaws across the full weld height. A low PCS value will concentrate energy towards the sample surface, while reducing energy at the backwall. Conversely, a high PCS will reduce energy near the surface of the sample, as well as encourage energy loss with increased path lengths.

3.4.1. PCS Study

A study to understand the sensitivity of images at different PCS values was conducted using the dual-tandem setup for each of the three mock narrow gap samples (NG1, NG2 & NG3), to ensure PCS sensitivity across the full height of the weld could be considered. The sensitivity values obtained in this study were calculated using the method discussed in Section 3.2.6. Three PCS values were chosen, such that the longitudinal normal beam of the two arrays intersected at a depth of $1/3$ (167 mm), $1/2$ (238 mm) and $2/3$ (314 mm) of the sample thickness. A TFM image was created for each PCS value, using the dual-tandem FMC acquisition process discussed above. The sensitivity for each of the four ‘views’ was calculated for the modes presented in section 2.2, for each of the three PCS values in each sample.

The bar plot in Figure 3.9 shows the mean sensitivity at each PCS for each mode, for each of the four views. A PCS corresponding to a longitudinal crossover of $2/3$ sample thickness, showed the highest sensitivity across each of the pulse-echo modes, except LL-T and right L-L. The $1/3$ thickness PCS exhibited the highest sensitivity for through-transmission. However, this was due to a strong reflection from the top of the lower notches, while exhibiting no diffraction effects. Therefore, it was decided that the ability to resolve diffractive effects – as part of the purpose of this work – was considered more valuable to this work.

Based upon these findings and given that all samples used in this work had a height of 120 mm, the $2/3$ thickness PCS value of 314 mm was chosen to be the PCS value used throughout the remainder of the study.

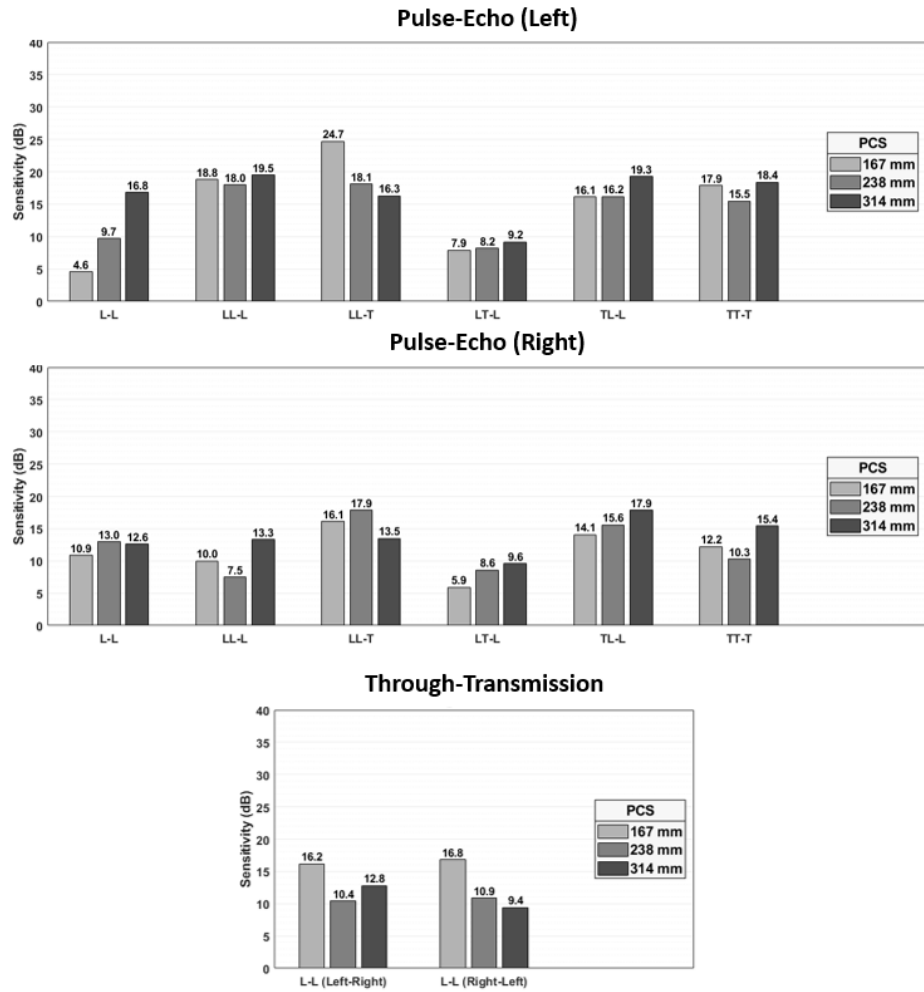


Figure 3.9: PCS sensitivity study results for pulse-echo (left), pulse-echo (right) and through transmission

3.4.2. PCS Error Study

To understand the precision levels required for array positioning, a PCS sensitivity study was conducted with added artificial errors. This considered a single FMC frame with a PCS of 314 mm, by adding a PCS error during the ray-tracing process. The artificial error was incremented from -5 mm to +5 mm and applied to the true PCS value, with image sensitivity recorded for each view in each mock narrow-groove sample (NG1,

NG2 & NG3). This error was applied to the PCS value, while maintaining a consistent centre point, as shown in Figure 3.10.

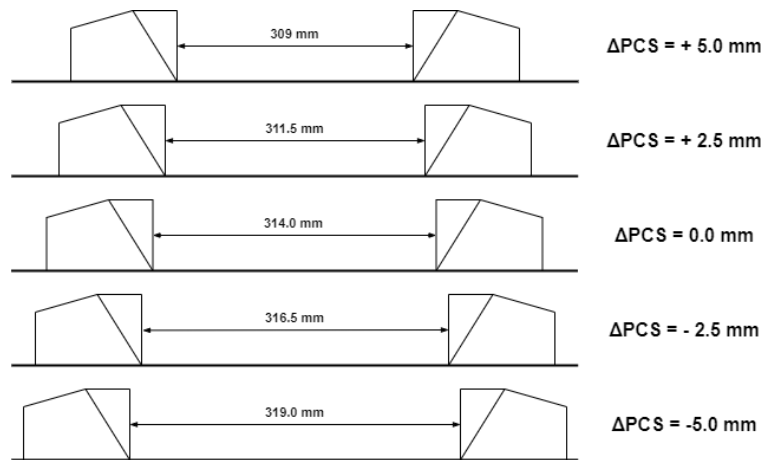


Figure 3.10: PCS values used to study PCS error

As this is a linear offset, the error should not noticeably affect the synthetic focusing of pulse-echo views as this is dependent on a single array. Instead, this is expected to provide a positional error – shifting the defect position with respect to the ‘real’ position. Conversely, for the through-transmission views, focusing will be altered as the relative position of each array is considered in the delay law calculations.

The results of this study can be found in Figure 3.11. It is clear that a positional error does affect the sensitivity of TFM images, and the effect is mode dependent.

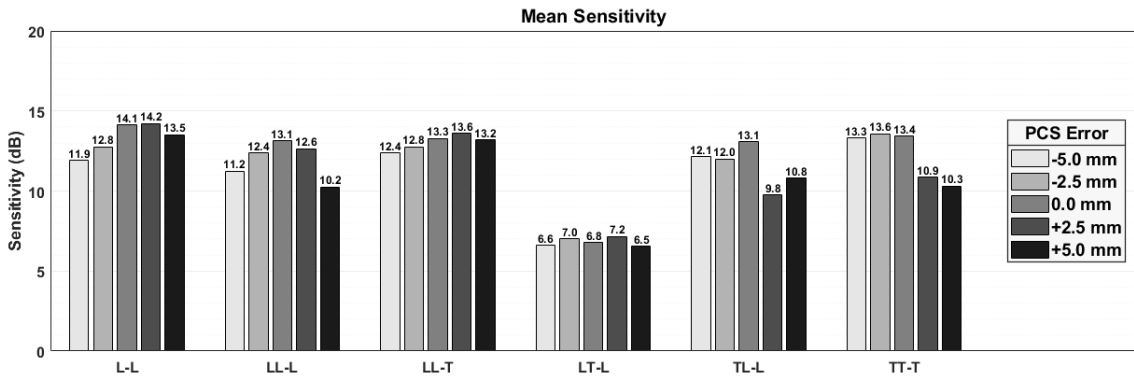


Figure 3.11: PCS error effect on pulse-echo image sensitivity applied to 314 mm PCS

This demonstrates that generally, the PCS does not affect the sensitivity more than ~3.0 dB at what is considered an extreme PCS positional error in this study. However, as previously stated, the effect of this error creates a purely positional error in pulse-echo images - equal to the positional error of the wedge position relative to the PCS centre point - as focusing is unchanged. It is the through-transmission imaging that is likely to be impacted most by this error.

A final sensitivity analysis was conducted to understand the effect of PCS error on through-transmission focusing in TFM images using the direct longitudinal mode, L-L. The results of this are shown in Figure 3.12.

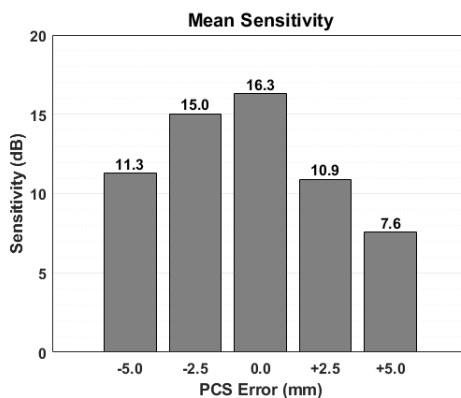


Figure 3.12: PCS error mean-view sensitivity study for L-L through-transmission images

It is clear from this study that, particularly at positive values, the sensitivity of through-transmission images is heavily dependent on PCS error. This asymmetrical sensitivity trend may be due to the encroachment of the lateral wave further into the image due to a positive positional error. In any case, this underlines the importance of precise PCS measurements when considering through-transmission imaging.

3.5. Imaging

As previously discussed, mock narrow-groove samples NG1, NG2 & NG3 were designed to replicate LOSWF defects in a 2° narrow gap J-groove. These were placed at depths of 27.5 mm, 60 mm and 92.5 mm respectively, relative to the notch centre. This section will firstly present TFM images obtained from a standard shear wave inspection, and then images generated using the dual-tandem method, with a PCS of 314 mm.

3.5.1. Shear Inspection

To ensure a fair comparison and quantification of the improvement offered by the dual-tandem method, a standard shear inspection was conducted. An Olympus 36.1° Rexolite shear wedge (SA32-N55S-IHC) was used to observe the performance of a typical ultrasonic inspection of each of the three-mock narrow-groove samples. The probe was positioned 100 mm from the sample centre, as a suitable trade-off between required beam steering and path length.

A TFM image was obtained from each sample, using the self tandem shear mode TT-T. Figure 3.13(b) shows the TFM image of the sample containing a notch at half the sample thickness. There is a slight notch indication in this image, with relatively low sensitivity,

with the height of the notch not being accurately quantified. Figure 3.13(a) and(c), where notches are present at 27.5 mm and 92.5 mm depths respectively, provide no obvious notch indications. This demonstrates the lack of weld coverage available using this method.

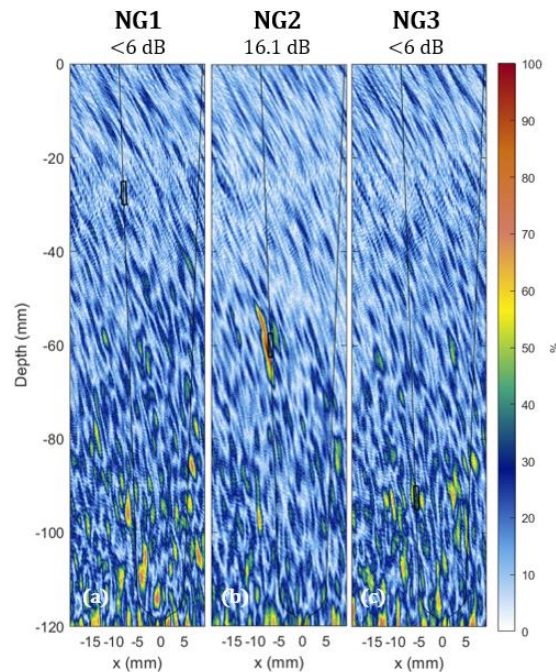


Figure 3.13: TFM images of mock narrow-groove samples using self-tandem shear (TT-T) pulse-echo inspection with a shear-transmission optimised wedge.

3.5.2. Pulse-Echo

The following section discusses the pulse-echo imaging results obtained using the 20° wedge discussed previously for transmission of both shear and longitudinal waves. Zoomed in versions of the images presented in this section can be found in Appendix A.

Figure 3.14 shows the pulse-echo images from the left array, for each imaging mode in sample NG1. Two modes appear to show clear indications from the 27.5 mm deep 2° notch. The direct longitudinal mode L-L in Figure 3.14(a) displays the highest

sensitivity to the notch, however it appears distorted due to the steering required to reach the shallow depth, which results in loss of energy through refraction and sidelobes. Conversely, the longitudinal self-tandem mode LL-L in Figure 3.14(b) exhibits poor sensitivity relative to the L-L mode. However, the added backwall skip demands less extreme steering for focusing at the shallower depth, relative to the direct longitudinal mode. However, the LL-L mode has several artefacts which could be mistaken for additional defects, and as such is likely to return several false-positives if considered in isolation. This is likely ‘leakage’ of another mode indication – which is something that must be considered when analysing multi-mode TFM images. Additionally, relative to the L-L mode, the notch amplitude is low and is therefore difficult to distinguish when normalised in this manner.

The remainder of the modes present no clear notch response, and as such exhibit low SNR values. Of these four in Figure 3.14(c-f), the TL-L mode is the only one which shows a slight indication, however this cannot be confidently resolved from surrounding artefacts without prior knowledge.

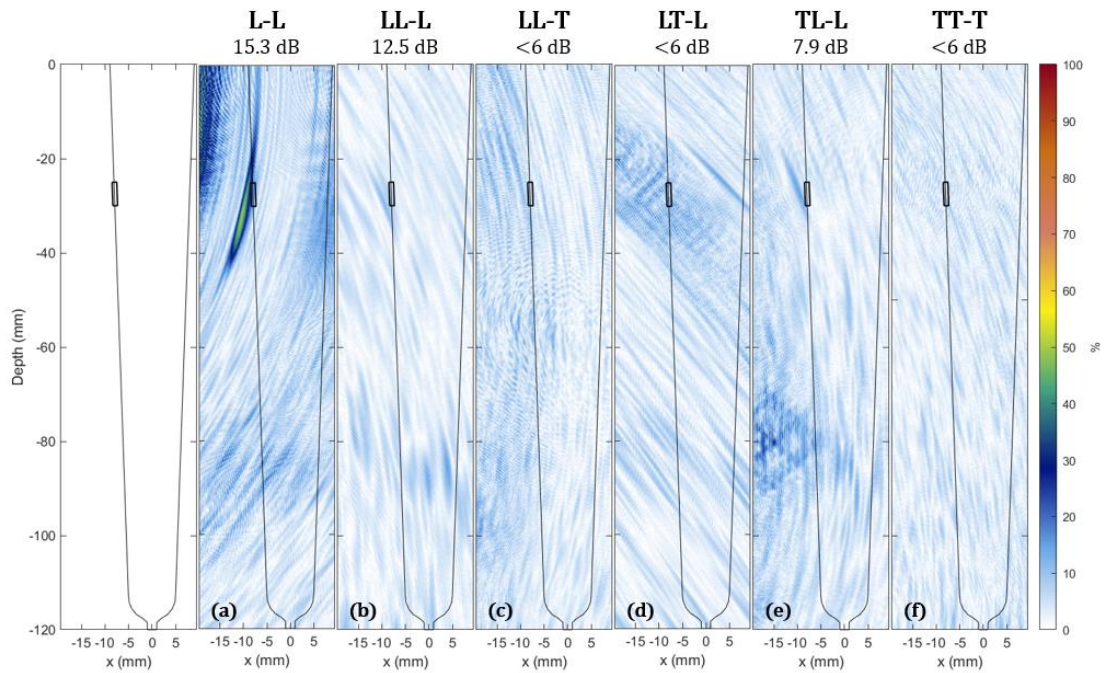


Figure 3.14: Sample NG1, 27.5 mm notch depth multi-mode pulse-echo TFM

In sample NG2, where the notch is located at half the sample thickness, all modes provide a greater sensitivity to the notch relative to sample NG1, as seen in Figure 3.15. The LL-L mode in Figure 3.15(b) provides a high sensitivity indication of reflection from the notch, with no artefacts which could present a false-positive as seen with the shallow notch. The direct longitudinal mode L-L also exhibits top and bottom tip-diffraction, which allows the extent of the defect height to be obtained through geometric sizing methods. In addition, the LT-L mode in Figure 3.15(d) provides tip diffraction, albeit with the poorest sensitivity. The remaining modes exhibit reflections from the notch face, with the LL-T mode providing the greatest sensitivity of the selected modes. Notably, the TT-T mode exhibits a higher SNR value than is seen in Figure 3.13(b), where a shear wedge is used, although again exhibits a lower amplitude when normalised across all modes.

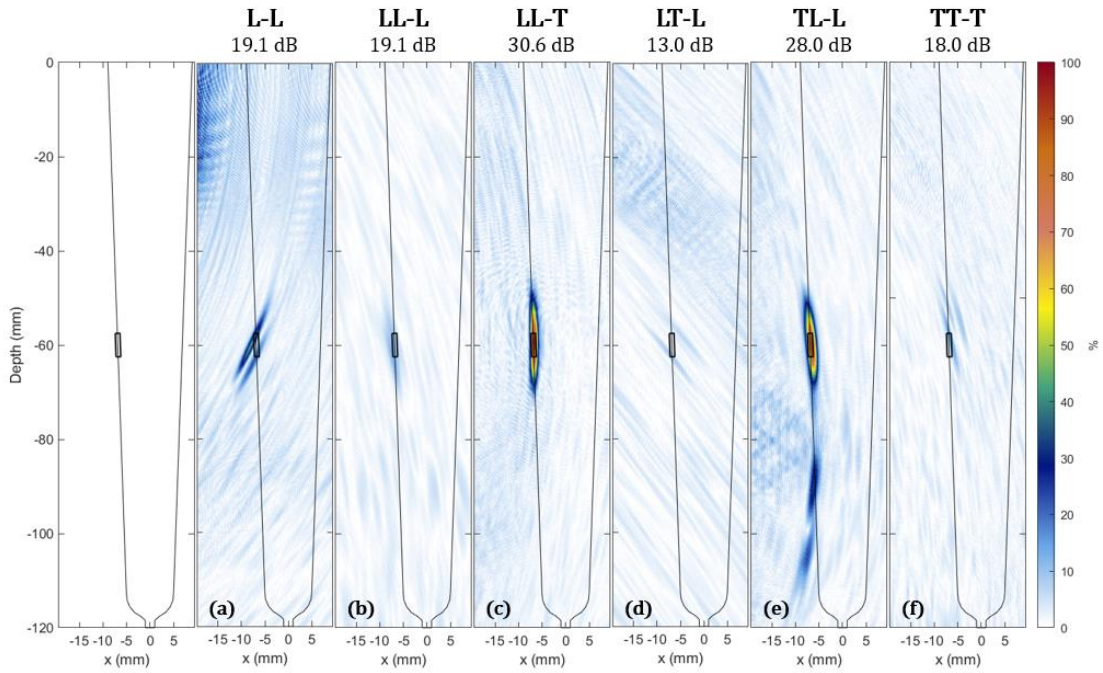


Figure 3.15: Sample NG2, 60 mm notch depth multi-mode pulse-echo TFM

Figure 3.16 demonstrates the sensitivity of each mode to the notch at 92.5 mm depth, in sample NG3. Again, the L-L and LT-L modes, in Figure 3.16(a) and (d), exhibit tip diffraction effects, with the direct mode showing the best sensitivity to these effects and the LT-L mode exhibiting low SNR. The shear mode TT-T provides the highest sensitivity to notch reflections observed across all samples, as seen in Figure 3.16(f). Furthermore, the LL-T and TL-L modes present additional second artefacts, which could be mistaken for a second notch and again risks a false-positive in isolation. This again highlights the caution required when considering multi-mode TFM. All but one (LT-L) of these modes provide a higher sensitivity value than the 16.1 dB value seen using the shear wedge in Figure 3.13(b), demonstrating the increased sensitivity to near-vertical defects obtained by using the optimised wedge angle.

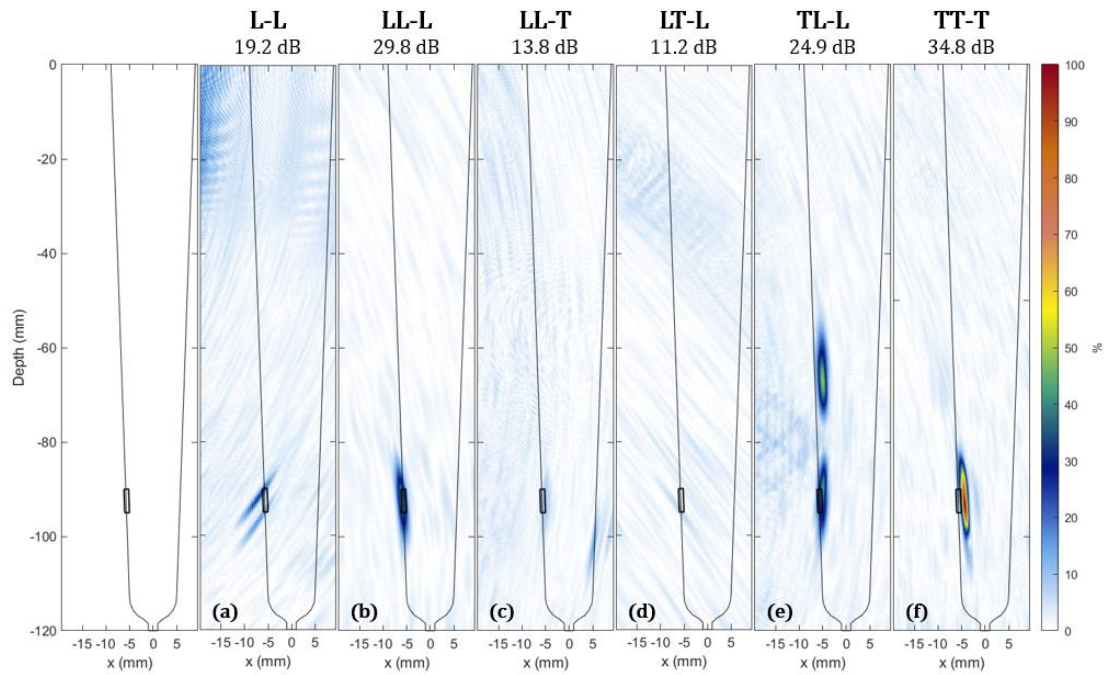


Figure 3.16: Sample NG3, 92.5 mm notch depth multi-mode pulse-echo TFM

The TFM images presented in this section have demonstrated the capability of pulse-echo imaging for detection of near-vertical defects in a mock narrow gap sample, using multi-mode TFM. The sensitivity values of the images presented in this section are summarised in Table 3.4. Sensitivity has been shown to be greater for larger depths, where focusing requires less extreme beam steering. The shallow notch in sample NG1 is only visible in the L-L and LL-L modes, with relatively low sensitivity when compared with notches in samples NG2 and NG3. The shear and longitudinal self-tandem modes provide the best sensitivity at the deepest notch.

Table 3.4: Summary of pulse-echo image sensitivity for mock narrow-groove samples

Sample	Sensitivity (dB)						Shear Wedge
	L-L	LL-L	LL-T	LT-L	TL-L	TT-T	
NG1	15.3	12.5	< 6	< 6	7.9	< 6	< 6
NG2	19.1	19.1	30.6	13.0	28.0	18.0	16.1
NG3	19.2	29.8	13.8	11.2	24.9	34.8	< 6

3.5.3. Through-Transmission

Considering the L-L mode in through-transmission in Figure 3.17, the lateral wave response is again observed. The dead zone due to this lateral wave masks the defect response from the shallow notch in NG1.

The notch at half the sample thickness in Figure 3.17(b) displays a strong bottom tip-diffraction. However, due to the directivity of the longitudinal beam, there is a large difference in amplitude between this and the top tip-diffraction response. In turn, the top tip exhibits an amplitude response 6.0 dB below the bottom tip. The peak-to-peak response displays a notch size of 6.0 mm, which oversized the notch by 1.0 mm.

In Figure 3.17(c), the deepest defect at 92.5 mm depth exhibits both top and bottom tip diffraction responses, with a peak-to-peak size of 5.5 mm, oversizing the 5.0 mm notch by 0.5 mm.

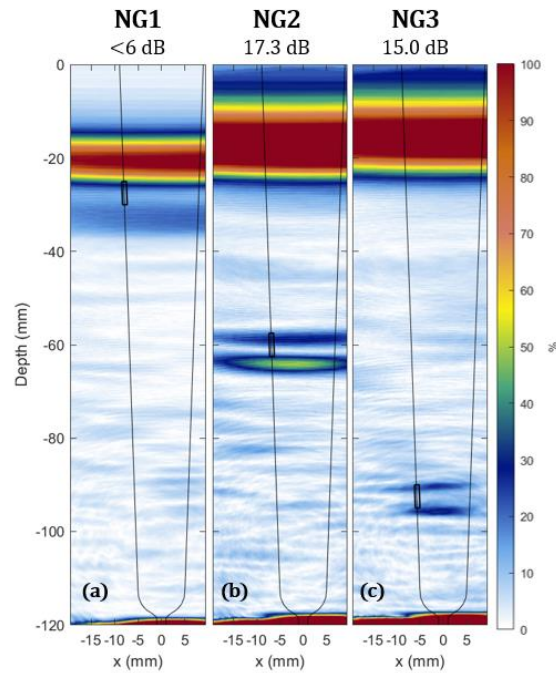


Figure 3.17: Narrow-groove sample imaged at 314 mm PCS in through-transmission with mode L-L for samples (left) NG1, (middle) NG2 & (right) NG3

3.5.4. Image Mixing

Due to the large number of images produced using this method, interpretation can be arduous. In order to condense the acquired image information, an image mixing process is performed as discussed in section 2.4.

For each of the mock narrow-groove samples, a mixed image was formed based on interpretation of images and their indication of diffraction and reflection responses from the EDM notches. Based upon this interpretation, it was determined that the L-L mode would form the fused diffraction image, by a pixel-by-pixel product of the pulse-echo and through-transmission images, as defined in (3.1). Furthermore, the pulse-echo images of modes LL-L, LL-T and TT-T were fused by pixel-by-pixel summation according to (3.2). The diffraction and reflection images were then normalised and

superimposed as defined in (3.3), to provide a single image. Figure 3.18 shows the resulting mixed images for each of the mock narrow-groove samples. It should be noted that, although these images are presented on a linear scale, they do not represent relative amplitude values - due to the superimposing of two normalised images.

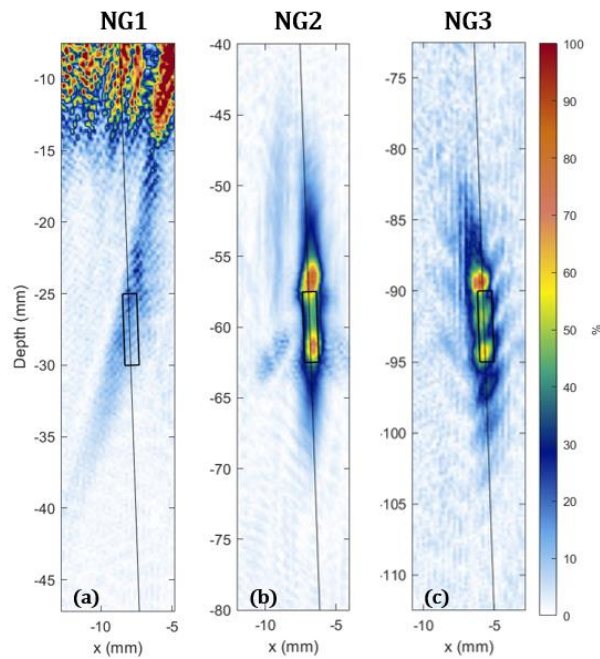


Figure 3.18: Image mixing in mock narrow gap samples (a) NG1, (b) NG2, and (c) NG3 using diffraction modes L-L, and reflection modes LL-L, LL-T & TT-T

Nonetheless, in Figure 3.18 (b) and (c) - samples NG2 and NG3 - where the EDM notch is placed at a depth of 60 mm and 92.5 mm respectively, there is an indication of the geometric extent of the notch in both image axes.

3.6. Further Discussion

3.6.1. Relative Amplitude

To understand the relative amplitudes between each mode in the three-mock narrow-groove samples in Section 3.3, both the maximum image amplitude and maximum notch amplitude were extracted. This allows the difference – if any between the maximum image amplitude and maximum notch response amplitude to be observed. If the image and notch amplitude values are equal, it can be reasoned that the notch response is the maximum amplitude response within the image. A difference in these values suggests that an artefact other than the notch dominates the image.

Firstly, this was conducted for pulse-echo views only in samples NG1, NG2 and NG3 - the results of which are found in Figure 3.19. Each bar is notated with an ‘L’ or ‘R’ to indicate a left or right pulse-echo view. Each view has a maximum image value shown as the wider bar, which is the highest pixel value in the image as a whole. The maximum notch amplitude by the thinner bar, which quantifies the highest a pixel value corresponding to a notch indication. By normalising these values to the maximum amplitude value across all images, a relative comparison can be made. In this case, values are normalised to the maximum image value of the left TT-T pulse-echo image in sample NG3, and all other values are displayed as a percentage of this amplitude value.

As the notch is offset from the centre of the sample to the left in this reference frame, there is a disparity in amplitude between left and right views, with the left pulse-echo view predominantly exhibiting higher notch response amplitudes. An inequality in the

maximum amplitude value extracted from the notch and from the image as a whole, suggests that artefacts with high amplitude relative to the notch response are present in the image.

As observed in the TFM images in Figure 3.14, some modes in sample NG1 do not provide any notch indications, so the notch amplitude is zero. Considering samples NG2 and NG3, with notch depths of 60mm and 92.5 mm respectively, modes L-L and TL-L provide the most consistent notch sensitivity. Despite providing the highest notch amplitude response, the disparity between left and right TT-T views is notable due to the offset position of the notch relative to the PCS centre.

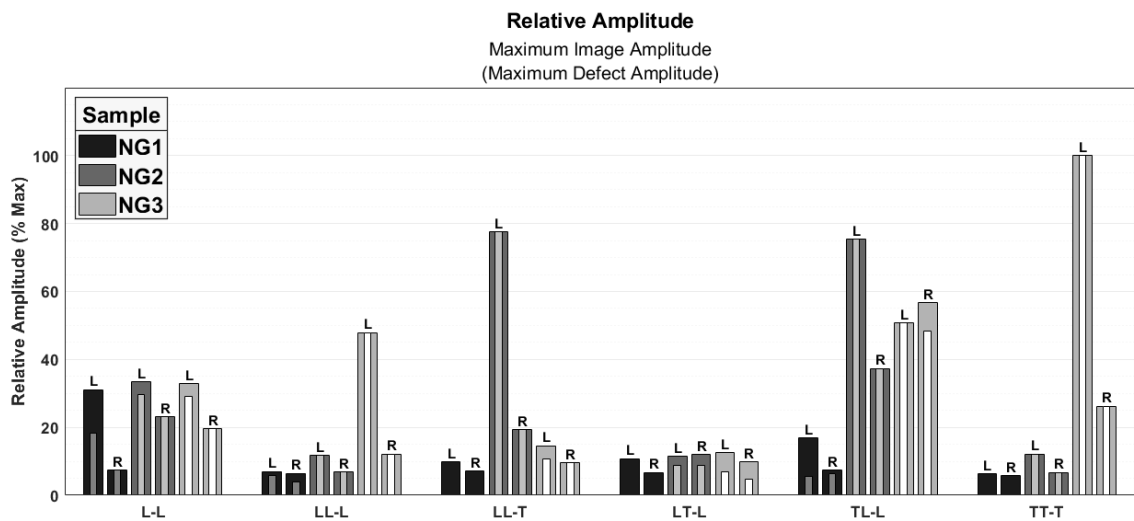


Figure 3.19: Relative amplitude study of mock narrow-groove pulse-echo TFM images. Amplitudes are normalised to the maximum amplitude (NG3 left pulse-echo), with maximum image and defect amplitudes shown. Left pulse-echo views are noted by ‘L’ and right pulse-echo views by ‘R’.

The same study can be conducted to observe the relative amplitudes of L-L pulse-echo and L-L through-transmission images, shown in Figure 3.20. Again, the amplitude values are normalised to the same value as in Figure 3.19.

As discussed previously, the L-L through-transmission images in sample NG1 do not provide notch responses, as these are likely masked by the lateral wave. In the through-transmission images of sample NG2 and NG3 shown in Figure 3.17, it is seen that the notch response is approximately 5.0 dB below the maximum image amplitude. This suggests that the lateral wave response is often double the amplitude of that of the notch, quantifying the difficulty in imaging shallow flaws near the lateral wave response.

It is also noted that the maximum through-transmission image amplitude of sample NG1 in Figure 3.17 is higher than that of the other two samples. As the notch response is masked by the lateral wave, this increase may be caused by the summation of the notch and amplitude responses, even though they cannot be individually resolved in imaging.

The pulse-echo notch responses are higher in amplitude than through-transmission for samples NG2 & NG3 by an average of 8.8 dB for the right view and 11.0 dB for the left. This increase in relative amplitude for the left view is expected, as the notch is physically offset from the PCS centre in this direction, reducing the pulse-echo path relative to through-transmission.

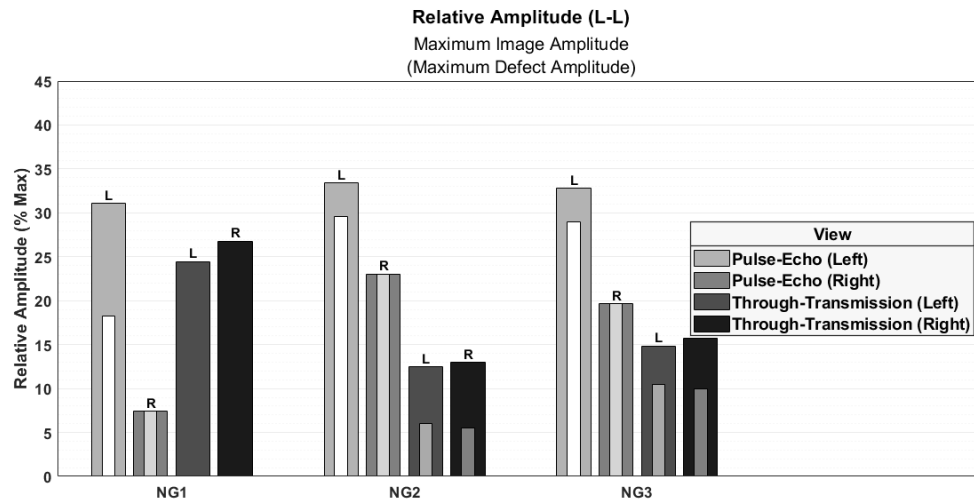


Figure 3.20: Relative amplitude study of mock narrow-groove L-L TFM images. Amplitudes are normalised to the maximum amplitude (NG3 left pulse-echo TT-T), with maximum image and defect amplitudes shown.

3.6.2. Notch Sizing

Typically, when sizing LOSWF defects with a pulse-echo phased array inspection methods, amplitude drop methods are employed - typically 6 dB, 12 dB or 20 dB [175]. The 6 dB drop case works on the assumption that the maximum defect amplitude response drops to approximately 50% when the beam is focused on the very edge of the flaw. However, the accuracy of this method relies heavily on defect orientation and geometry, as an assumption of defect orthogonality to the ultrasonic beam must be made in this case of planar defects such as LOSWF.

The advantage of using longitudinal modes, particularly for through-transmission imaging, is the ability to observe tip diffraction effects. This provides accurate sizing of a planar defect's height, using the peak-to-peak distance between the top and bottom tips. As these indications are inherently caused at the extremities of a flaw, they provide more precise measurement capabilities than amplitude drop methods.

By utilising both the 6 dB amplitude drop method for reflective responses, and peak-to-peak method for diffraction indications, a mean notch size across each pulse-echo view was obtained for each mode and sample. Figure 3.21 highlights the obtained notch height, with reference to the expected 5 mm height.

As is clear from the pulse-echo images presented previously, only the L-L and LL-L modes provided a resolvable defect response from the shallow notch in sample NG1. The L-L mode did not provide an accurate size, due to the spread of the notch response. However, the LL-L mode provided a height close to the expected 5 mm using the 6 dB drop method.

Considering the notch at half the sample thickness, in sample NG2, a notch height is determined for each mode. Modes L-L and LT-L provided tip-diffraction effects and gave a 6.9 mm and 6.5 mm peak-to-peak notch height respectively. The TT-T mode 6 dB drop shows a 3.6 mm notch size. Despite having the lowest error of all modes in this sample, it is the only mode which under-sizes the notch. To ensure the safety of a scanned component, it is preferred to over-size rather than under-size flaws, and this result would therefore be a concern. The remaining modes, all using the 6 dB drop, oversize the notch height by at least 5 mm. Conversely, oversizing of a defect in this manner can be costly and can force unnecessary part rejection, or temporary operation shutdown. For this reason, it is important that defects can be accurately sized such that the appropriate action can be taken.

Now considering the deepest notch, in sample NG3, sizing was able to be conducted using each mode. Of the three notch depths considered, this provided the most accurate

sizing across all modes. Again, modes L-L and LT-L provided tip diffraction indications, with the remaining modes showing reflections from the notch face. L-L and LT-L provided the most accurate notch height at 6.0 and 5.8 mm respectively. Modes LL-T and TT-T showed relatively accurate defect heights of 6.5 mm and 8.1 mm, with modes LL-L and TL-L greatly oversizing using the 6 dB drop method.

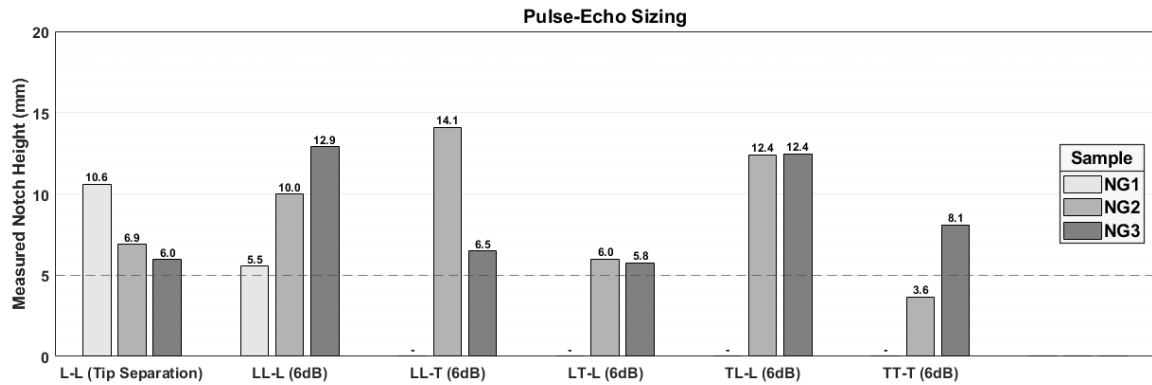


Figure 3.21: Pulse-Echo sizing of notches in each mock narrow-groove sample. Peak-to-peak sizing method used for tip-diffraction indications, and 6 dB drop method for reflections.

The same method can be applied to through-transmission imaging. In this case, only diffraction effects are seen, so the peak-to-peak sizing method is used. Furthermore, only the direct longitudinal mode L-L is considered for through-transmission imaging.

It is initially obvious from Figure 3.22 that the sizing error using through-transmission is reduced relative to the sizing with pulse-echo. As discussed, the lateral wave masks the shallowest notch in sample NG1, therefore no defect response is present to allow sizing. Sample NG2 demonstrates a mean size across the through-transmission views of 6.1 mm. Furthermore, NG3 demonstrates a mean notch height of 5.0 mm. This follows the same pulse-echo trend for mode L-L, with increased sizing accuracy for deeper notches.

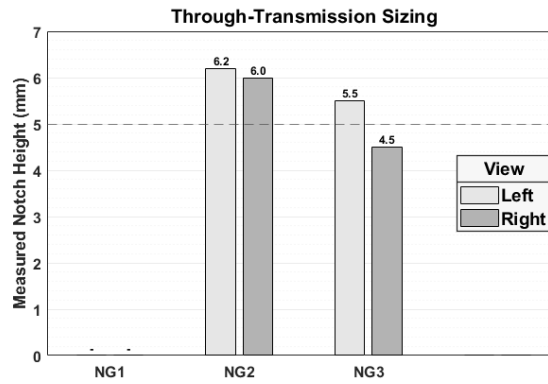


Figure 3.22: Through-Transmission sizing of notches in each mock narrow-groove sample using peak-to-peak sizing method using L-L mode

This demonstrates the ability to size the notch height in both pulse-echo and through-transmission imaging, with through-transmission improving the sizing error. However, due to the views available using this method, the width of the notch may in theory also be sized. By considering the image mixing discussed previously, there is an opportunity to size the notch in both imaging axes. However, as discussed, this requires a great deal of operator input, and is not feasible in this work due to tolerances associated with the PCS measurement. Work is required to produce mixed images seen in Figure 3.18 programmatically, such that the size can be extracted without the inclusion of human error.

In reality, defects such as LOSWF sized in this manner often have minimal width, so determining the width of the defect is not necessary. However, this method could be useful for other flaw types such as porosity and inclusions, to obtain a two-dimensional perception of the defect shape, without the requirement for amplitude drop methods.

It is clear that the dual-tandem method provides advantages to traditional shear pulse-echo in both detection and sizing of near-vertical defects in mock narrow-groove

samples. The inclusion of pulse-echo acquisition from both weld sides allows each weld bevel to be imaged with equal sensitivity. Furthermore, the inclusion of longitudinal through-transmission allows increased sensitivity to tip-diffraction effects. This has been shown to improve near-vertical notch sizing accuracy relative to pulse-echo methods.

3.7. Conclusions

Traditional phased array weld inspection is conducted using a single probe in shear mode. However, this has proven to be ineffective when detecting and imaging near-vertical defects. In narrow-groove weld inspection, LOSWF defects present themselves along the bevel, at typically near-vertical angles. Furthermore, the thick-section nature of narrow-groove welding poses issues with increased attenuation and reduced full weld sensitivity. For this reason, the dual-tandem method is proposed to allow both pulse-echo and through-transmission detection of such defects.

An FMC acquisition and TFM imaging process which allows two pulse-echo and two through-transmission views to be obtained and imaged in a single scan. This was tested using three 120 mm thick carbon steel samples, with EDM notches placed in a position representative of a narrow-groove LOSWF defect at a varying sample depth. The resulting TFM images were found to show good sensitivity to near-vertical notches at various depths from reflection and diffraction effects. Through-transmission imaging provided accurate notch sizing of deeper defects with high-quality TFM images. The introduction of an image mixing algorithm allowed the full extent of the defect in the image plane to be observed at deeper notch depths.

Chapter 4

In-Process Narrow Gap Inspection

4.1. Introduction

With an ultrasonic method demonstrated for the inspection of narrow gap weld geometries using a dual-array setup, the focus of this work was shifted to consider use for an in-process inspection environment. This introduces a number of challenges that are not normally encountered when approaching ultrasonic inspections. As discussed previously, standard ultrasonic welding procedures [23, 24] dictate that the NDT process should occur after the welding process is complete - giving sufficient time for cooling defects such as hydrogen cracking to form. The in-process inspection concept briefly discussed in Section 1.1 seeks to combine the welding and inspection processes, which introduces high temperatures, changes to microstructural behaviour, and complex weld geometries.

By detecting defects as they are formed using a layer-by-layer inspection process, risk to schedule certainty from extensive defect rework is reduced. Defective areas can be reworked between weld passes without extensive excavation, and with minimal process disruption. This is demonstrated in Figure 4.1 for a hot-pass weld defect detected in a

narrow gap weld. In addition to process certainty, this vastly reduces the energy and consumable requirements to complete the weld, and ensures a right-first-time process.

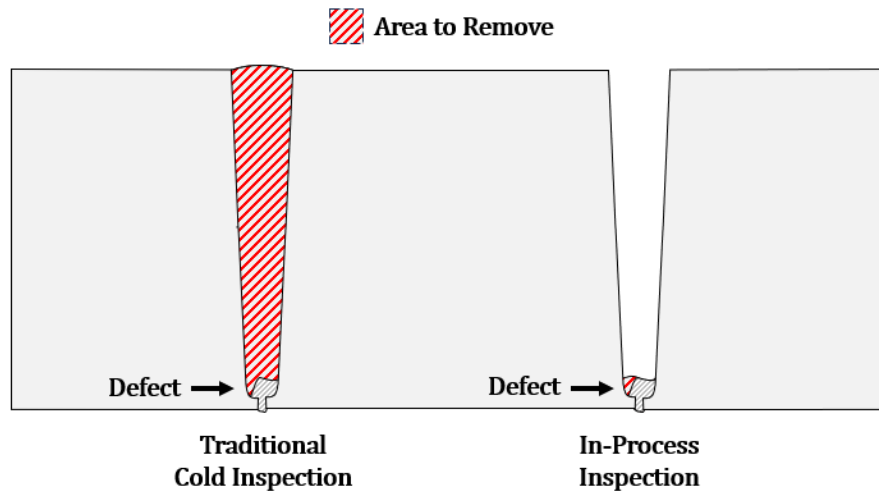


Figure 4.1: Rework required for a hot-pass defect detected with traditional cold inspection post-welding (left) and in-process inspection (right)

The advancement of in-process inspection techniques has seen an increase in the past decade. The use of liquid-filled high-temperature dry-coupled ultrasonic wheel probes have shown high performance in-process inspection of both V-groove welds and Wire + Arc Additive Manufacturing (WAAM) using traditional Phased Array Ultrasonic Testing (PAUT) methods [87, 89, 168]. These wheel probes have demonstrated heat tolerances to process temperatures of up to 350°C experienced in close proximity to the welding process. As a typical immersion array can withstand temperatures up to 60°C, thermally insulating materials and tight thermal management are vital to ensure reasonable operating conditions within the wheel probe. This has allowed continuous inspection of components during manufacture, as well as monitoring of hydrogen cracking post-weld for up to 96 hours [86]. In addition, this has been combined with a

robotic welding infrastructure to provide a combined automated in-process inspection and welding technique [176], ensuring the consistency of both processes. Ultrasonic data obtained in-process has also been used for real-time monitoring and adjustment of welding processes to actively prevent defects forming [177]. The ability to transmit ultrasound with a dry-coupling technique allows safe use during the welding process without contamination of the weld through liquid-coupling. However, this has not yet been demonstrated for narrow-groove weld geometries.

The dual-tandem method discussed in the previous chapter has deployed advanced acquisition and image processing methods through the use of Full Matrix Capture (FMC) and the Multi-Mode Total Focusing Method (MM-TFM) [122, 131]. An advanced path finding algorithm has also been shown in Chapter 3 to compute the post-processing delay laws required for the extensive focussing of algorithms such as TFM and PCI with the dual-tandem method. The MSFMM allows the computation of travel times through non-homogenous and anisotropic materials, with low error and efficient output. The combination of the TFM algorithm with the MSFMM path finding method has often been termed ‘TFM+’ in previous publications [153, 156].

Thus far, the effectiveness of the dual-tandem phased array method has been demonstrated in mock narrow-groove samples containing near-vertical notches to simulate LOSWF defects - considered a ‘cold’ inspection of a completed weld. This Chapter will begin to explore the application of the dual-tandem method as an in-process narrow gap weld inspection technique.

Contrary to the controlled environment preferred for post-manufacture component inspection, an ultrasonic in-process inspection method must maintain detection performance in adverse conditions. Partially-filled weld geometries can introduce non-defect reflections from the un-filled weld groove and uppermost pass weld cap, as well as requiring careful consideration of inspection setup at each weld pass. High temperature gradients can skew and shift ultrasound such that imaging is not properly focused unless compensated for. Other factors such as process interference, data transfer speeds and image processing optimisation also present added challenges. These problems complicate an inspection both mechanically and ultrasonically - complicating and limiting deployment if not addressed correctly.

Key research has already been conducted to understand and address some of these issues faced during an in-process weld inspection. PAUT inspection of partial-weld geometries has shown high-sensitivity of intentionally imbedded tungsten defects in V-groove welds [85]. Thermal compensation methods have been explored using advanced ultrasonic imaging methods, shown to improve defect localisation during high-temperature inspection [154]. In the interest of reducing acquisition, transfer and processing times for real-time imaging, data reduction techniques such as single-bit PCI [143] and Plane-Wave Imaging (PWI) [132, 178] acquisition have been considered in the wider literature.

This work will look to consider and demonstrate the effectiveness of the dual-tandem method for in-process narrow gap weld inspection, by considering the effect of partial weld geometries with steep bevels on mock LOSWF defects.

4.2. Experimental Procedure

The dual-tandem phased array method has been shown to increase sensitivity and effectiveness of near vertical defects in mock narrow gap weld inspection [155]. By utilising a dual-array setup across the weld, a symmetrically uniform sensitivity of reflective phenomena at each weld side is achieved. Particularly when considering in-process inspection, this reduces the need to conduct two individual scans on both weld sides. Furthermore, the ability to perform through-weld propagation can increase the sensitivity of the system to diffractive effects, allowing tip diffraction indications to be detected and accurate flaw sizing.

Imaging using the dual-tandem method has been performed by using post-processing algorithms such as TFM on FMC acquisition data. The remainder of this section will briefly outline the software and hardware requirements of this method, as well as the acquisition and image processing algorithms used.

4.2.1. FMC Acquisition

The hardware used in this work required for FMC acquisition using the dual-tandem phased array method is outlined below. Two arrays with Rexolite wedges were used in conjunction with a PEAK-NDT phased array controller.

- 2x: 5 MHz, 64-element Olympus A32 phased array probes (*0.5 mm pitch*)
- 2x: 60LW Olympus A32 Rexolite wedge (*20° wedge angle, 2330 ms⁻¹ velocity*)
- PEAK-NDT MicroPulse 6 phased array controller (*128/256 channel*)

Subsequently, the DAFMC acquisition and imaging process outlined in the previous chapter were used, utilizing both pulse-echo and pitch-catch data in a single FMC frame.

All data was collated and saved using a LabView [170] acquisition programme which interfaces with the PEAK-NDT array controller. FMC data was then saved in Multi-Frame Matrix Capture (MFMC) [171] file format and processed using the MATLAB GUI described in Section 2.5.9.

4.2.2. Time of Flight Calculation

With the added complexity of the partial weld geometry, careful consideration is required when approaching Time-of-Flight (ToF) calculations required for the extensive focussing involved in post-processing imaging algorithms. To ensure ToF values that accurately represent the propagation of waves throughout the image domain, it is important that the weld geometry at a given pass is known, such that it can be considered in calculations. The extent to which this geometry is known will directly influence the quality of the image produced. However, during the welding process, the exact geometry of the weld cap cannot precisely be known without increasing the complexity and time of the inspection process – counter to the benefit of in-process inspection. From a Weld Procedure Specification (WPS), a pre-emptive approximation of the cap geometry can be made for each weld pass, and used to compensate the ToF values calculated for a given pass.

In reality, the cap of a recently deposited weld pass is not uniform or flat, due to the weaving nature of the welding process. The geometry of this cap can be difficult to

accurately predict, and therefore is difficult to compensate for delay law calculations. Therefore, in this work a perfectly flat weld cap will be used, considering only the bevel geometry and filled weld height.

For the work in this chapter, the MSFMM is again used for this calculation for its flexibility for partial weld geometries. Figure 4.2 shows an uncompensated and geometrically compensated pulse-echo ToF map, for a 30 mm filled partial weld geometry in a 120 mm plate at a PCS value of 327.5 mm. It is clear that there are significant shifts in the ToF on the far weld side when compensating for the weld, as waves are prevented from crossing the air gap in the unfilled weld portion.

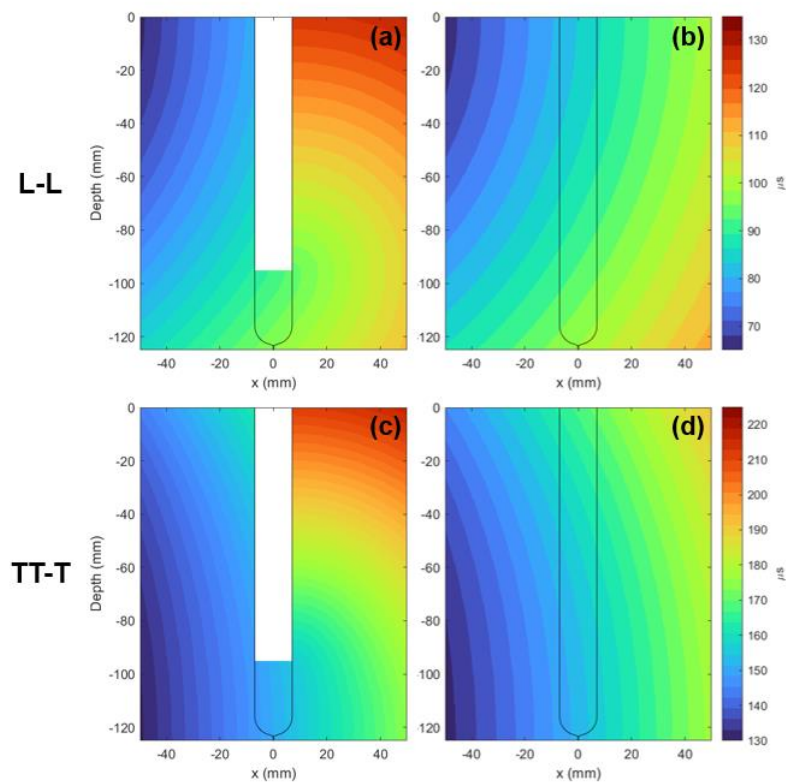


Figure 4.2: Example of ToF compensation for a partial weld geometry, for pulse-echo L-L mode (a) compensated and (b) uncompensated for geometry, and for pulse-echo TT-T mode (c) compensated and (d) uncompensated for weld geometry

4.2.3. Imaging

Imaging was done in the same manner as in the previous Chapter (see Section 3.2), with the addition of using the PCI algorithm. Again, this was done using GPU accelerated MATLAB code [172, 174] generated by the MATLAB GUI introduced in Section 2.5.9.

4.2.4. Data Fusion

As introduced in the previous chapter, data fusion is handled in terms of diffractive I_D and reflective I_R images. Selected diffractive and reflective images are normalised individually, and summed together to create a final multi-mode mixed image I_T , given by the expression in (3.1).

$$I_T = \widehat{I}_D + \widehat{I}_R \quad (4.1)$$

Given the non-linear fusion of reflective and diffractive data, it is not possible to provide a sensible SNR value for fused images. Therefore, fused images will be presented without quantitative SNR analysis.

The mixed image will be presented with different normalisation for TFM and PCI. The TFM mixed image is normalised to either the maximum pixel value in the image, or a common normalisation value for comparison of multiple images.

For mixed PCI images, normalisation is set to the maximum coherence value. This value is the number of A-Scans used for a single image reconstruction, which in this case for a single PCI image using two 64-element arrays is $N = 16,384$. The maximum coherence for a mixed image N_{mix} is therefore given by (4.2), where M_D and M_R are the number of

diffraction and reflection modes used in the mixed image respectively. As the diffraction mixing considers all four views of the image, the number of images M_D used is 4, similarly the number of reflection images M_R is 2 as only the two pulse-echo views are considered.

$$N_{mix} = 4N^{M_D} + 2M_R N \quad (4.2)$$

As a value of maximum coherence in a mixed image would require a pixel to exhibit maximum coherence across all images used, the resulting normalised mixed PCI image often exhibits low coherence, even if the coherence of individual images remains high. For this reason, mixed PCI images are presented on a reduced coherence colour scale in the range of 0% to 25% of the maximum coherence.

4.3. Test Samples

In order to test the dual-tandem method for in-process narrow gap weld inspection, a number of mock narrow gap geometries were created to replicate a partially-filled narrow groove. The samples themselves are 125.0 mm thick A36 mild carbon steel blocks, 500.0 mm in length and with a width of 30.0 mm - a thickness indicative of a thick section found in nuclear components.

These were created to simulate a partial weld geometry at three stages of the welding process; with filled 'weld' heights of 104.0 mm, 70.0 mm and 37.5 mm. Figure 4.3 shows the geometry of the three weld heights. The weld geometry attempted to mimic a 4° inclusive narrow gap weld, with 2.0 mm root height and 5.0 mm radius.

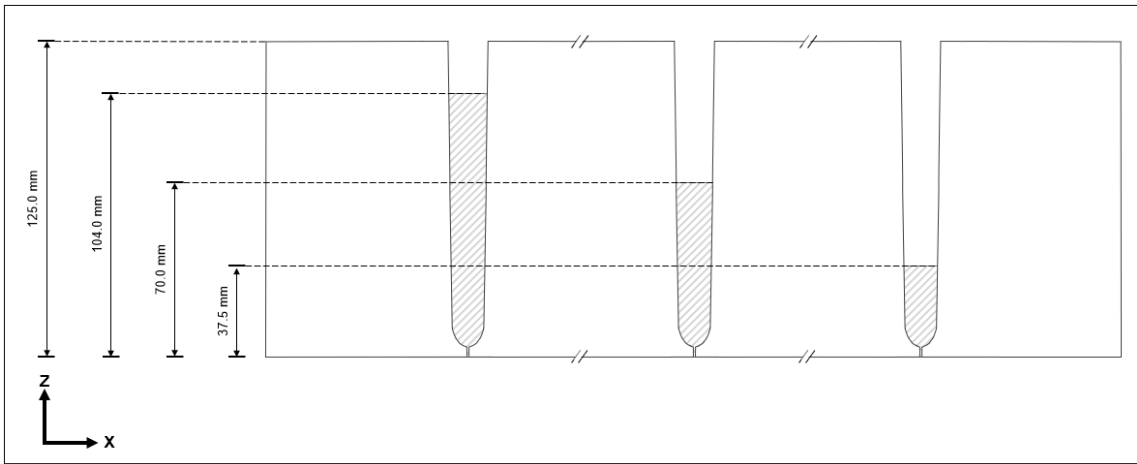


Figure 4.3: Partially filled weld samples with weld fill of 104.0 mm, 70.0 mm and 37.5 mm.

To simulate the existence of a LOSWF defects in these samples, notches created using Electrical Discharge Machining (EDM) were machined into the steel blocks. These were 5.0 mm in height and 1.0 mm wide, rotated at 2° to match the bevel angle, and machined 10.0 mm into the 30.0 mm block thickness. These were positioned such that the notch centre was approximately 7.5 mm below the partially filled weld cap on one side – the geometry of the three samples with EDM notches are pictured in Figure 4.4.

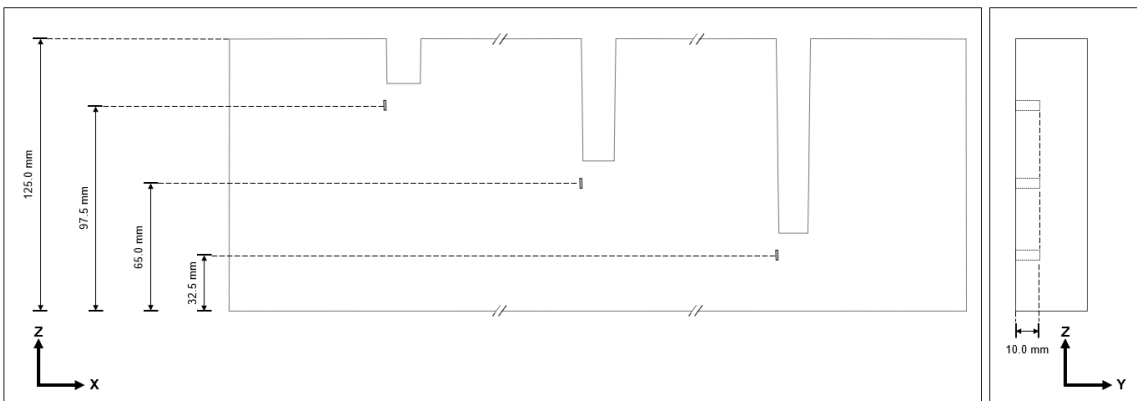


Figure 4.4: EDM notch position and through-thickness depth in mock partial narrow gap samples

The samples will be referred to as Partial Narrow Gap (PNG) for the remainder of this work, with definitions outlined in Table 4.1. Six total samples were created, two for each weld fill height defined above. This consists of one defective sample containing an EDM notch, and a ‘clean’ sample for comparison purposes.

Table 4.1: Sample labels and geometry

Label	Weld Fill Height (mm)	Notch Height (mm)
PNG1	<i>104.0</i>	-
PNG2	<i>104.0</i>	<i>97.5</i>
PNG3	<i>70.0</i>	-
PNG4	<i>70.0</i>	<i>65.0</i>
PNG5	<i>37.5</i>	-
PNG6	<i>37.5</i>	<i>32.5</i>

It should be noted that effects observed in real in-process weld inspection cannot be modelled using these samples. One such effect is high temperature gradients, which can skew ultrasonic waves and cause defect positional errors. Additionally, microstructure effects seen by a Heat Affected Zone (HAZ) are not modelled. These samples aim to simulate the effects of a partial weld in ideal conditions, at a steady room temperature and with no HAZ effects. A photo of sample PNG4 with dual-tandem phased array setup is shown in Figure 4.5.



Figure 4.5: Sample PNG4 with dual-array setup, highlighting simulated 70.0 mm weld fill height and 65.0 mm EDM notch height.

4.4. Adaptive PCS

As demonstrated in the previous chapter, to maximise full weld thickness coverage, a ‘full thickness’ PCS, where the longitudinal crossover of the two arrays is at a depth equal to $2/3$ of the sample thickness is preferred. This is similar to standard inspection procedure for Time of Flight Diffraction (TOFD) techniques [111]. However, when considering an in-process inspection scenario with partial weld geometries, full thickness coverage is not necessarily desirable, as each pass can be inspected individually as deposited. Consequently, an adaptive inter-pass PCS can be employed, concentrating acoustic energy towards the current pass, with less importance given to formerly inspected and unfilled weld sections. The pre-defined full thickness PCS can then be used for a final full thickness cold inspection, required by ISO 17640:2018 [24]. This section will seek to provide a basic rule for an adaptive PCS, such that probe position can be determined for optimum weld coverage at a given weld fill height.

In order to ascertain a reference depth value for calculation of the PCS for a given weld pass, it is necessary to conduct a study using various calculation values. Similar to the full thickness PCS, a value can be calculated such that there is a longitudinal crossover at a given reference depth. This is based upon the filled weld portion, and will consider PCS values for longitudinal crossover points of $1/3$, $1/2$ and $2/3$ relative to the top of the most recently deposited pass. Figure 4.6 shows an example of PCS defined as $1/3$ of the filled weld in sample PNG5, at 372.3 mm.

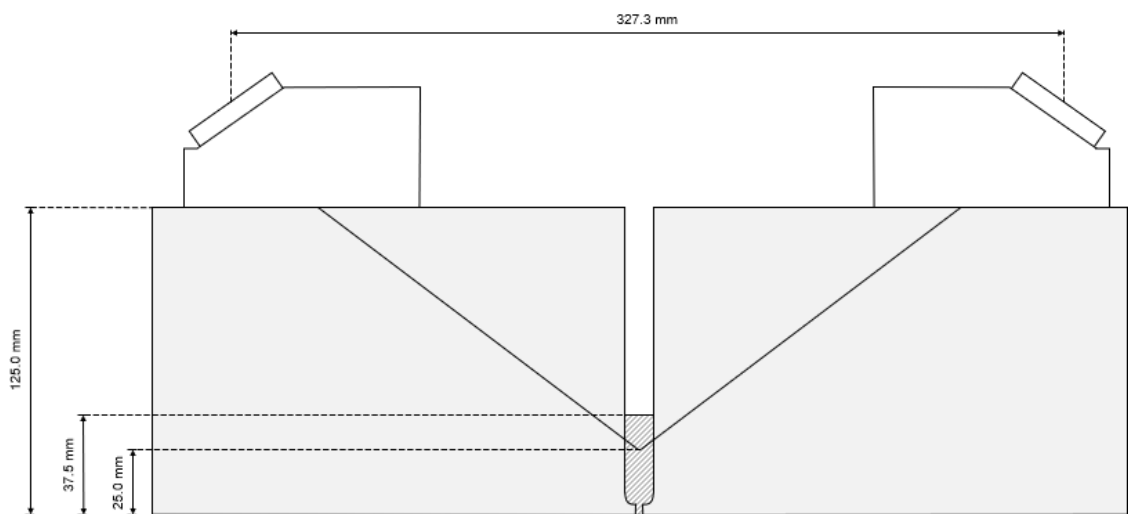


Figure 4.6: $1/3$ filled weld longitudinal beam crossing for PCS calculations on sample PNG5

This study was conducted for the three samples containing EDM notches; PNG2, PNG4 and PNG6.

Images were generated using the direct L-L mode as the diffractive mode and TL-T and TT-T as the reflective modes for each sample. These were chosen as the most suitable modes based upon analysis of the useful notch indications across all direct and self-tandem image modes.

Figure 4.7 shows the defect responses, with amplitude normalised relative to the maximum defect response, and phase to the maximum coherence value. Both the L-L and TT-T mode amplitude responses decrease with increasing PCS. This is also true for the phase coherence of the TT-T mode, however the L-L coherence exhibits the greatest response at 1/2 PCS definition. However, the TL-T mode behaves differently with changing PCS. The amplitude at 1/2 PCS definition is greater than that of the other PCS values for both phase and amplitude – particularly amplitude. Solely, from this data, it is difficult to define an optimum PCS value for this sample, as it appears mode dependent. However, it could be argued that 2 of the three modes are optimum at the 1/3 PCS definition, despite the TL-T mode exhibiting a far greater amplitude at the 1/2 PCS definition.

Figure 4.8 demonstrates the same trend for modes L-L and TT-T in sample PNG4, with the exception of the L-L mode response exhibiting a maximum at the 1/2 fill PCS definition. However, the TL-T trend differs greatly, and falls in line with the TT-T modes – with decreasing amplitude and phase indications with increasing PCS. This suggests that the 1/3 PCS definition is the desirable PCS for this sample.

Figure 4.9 also suggests that the 1/3 PCS fill definition provides the best defect response for sample PNG6. Both the direct L-L mode and TT-T mode drop in amplitude with increasing PCS suggesting that the 1/3 definition is optimum. However, the phase coherence remains consistent for both modes. The TL-T phase coherence also remains fairly steady across the differing PCS, but amplitude response drops.

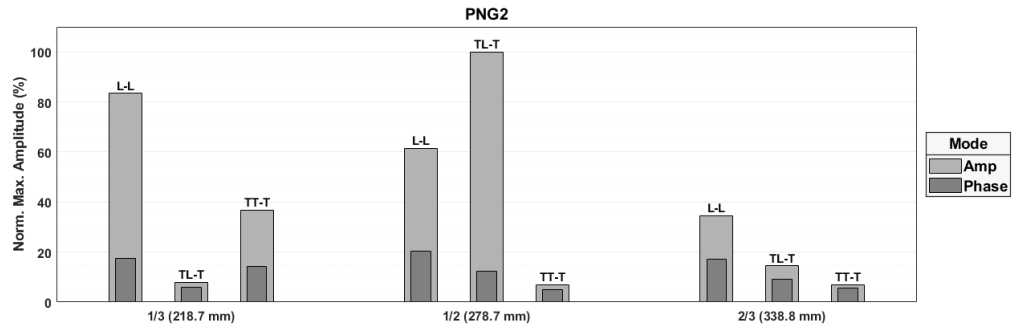


Figure 4.7: Defect response amplitude and phase coherence for L-L and TL-T modes in PNG2 mixed image

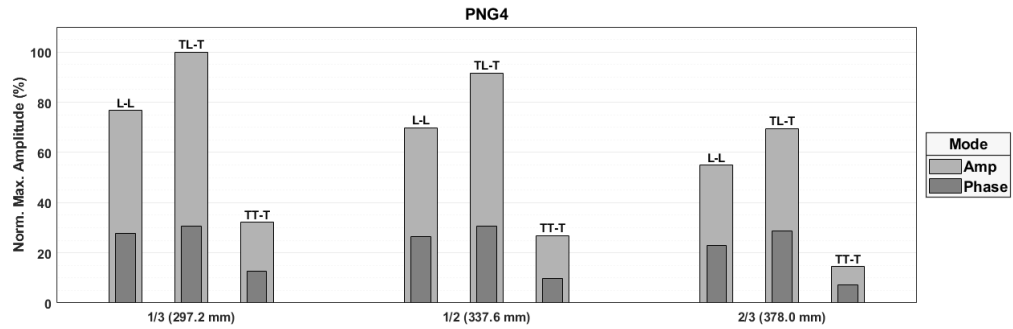


Figure 4.8: Defect response amplitude and phase coherence for L-L and TT-T modes in PNG4 mixed image

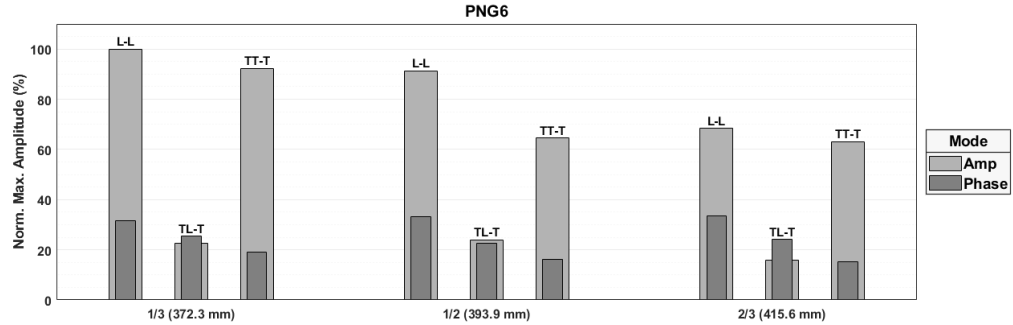


Figure 4.9: Defect response amplitude and phase coherence for L-L and TT-T modes in PNG6 mixed image

It should be noted that differences in a defect response amplitude can be caused by coupling variations between frame capture. To eliminate this as a potential source of error, analysis of the amplitude response from the backwall of each frame using the direct shear T-T mode was conducted, allowing the amplitude variation due to coupling

to be quantified. Figure 4.10 shows the backwall response amplitude, normalised to the maximum response. The coupling variation has the potential to be a significant contributor to any differences in response between frames, given that the same excitation voltage and post-gain was used for each. It is clear that there is no significant (>3 dB) coupling deviation across each frame from the three samples, and therefore the trend in amplitude response in this PCS study is unlikely to be significantly impacted by coupling variation.

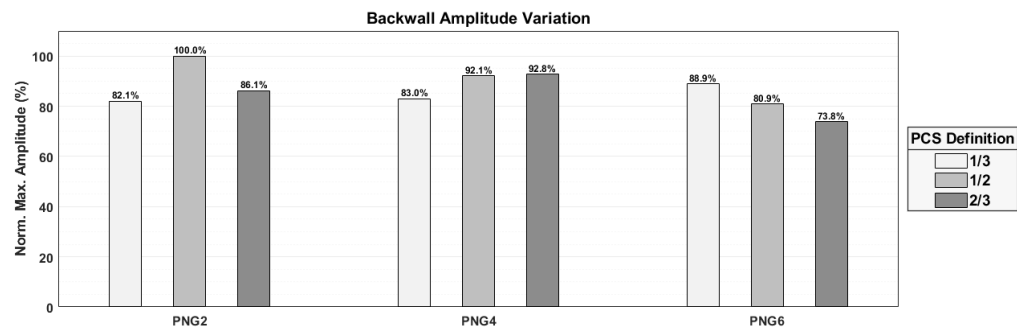


Figure 4.10: Coupling variation analysis using backwall signal of T-T mode for each PCS in each sample

A consistent PCS definition means that a lookup table can be generated, defining the PCS for any given plate thickness and weld fill height, as shown in Figure 4.11 (for thicknesses of 16 mm to 150 mm).

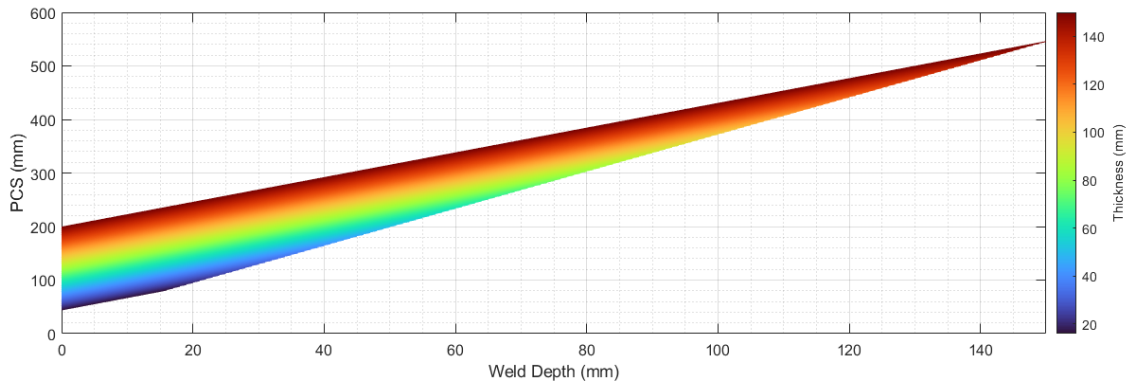


Figure 4.11: 1/3 weld fill PCS definition for varying plate thicknesses and fill heights

This study was performed on modes selected quantitatively based on image performance. However, as further outlined in the Future Work section, the development of an algorithm to quantitatively calculate the optimum PCS and modes used at a given weld height would greatly benefit a method such as this.

4.5. Imaging

This section will present and analyse the TFM and PCI image performance when inspecting samples containing EDM notches (samples PNG2, PNG4 & PNG6). As described in Section 2.6, images are mixed by considering modes which contribute with diffractive and reflective responses. Furthermore, as concluded from the previous adaptive PCS study, a PCS definition of 1/3 of the weld fill height is used. A summary of both the diffractive and reflective modes used in each mixed TFM and PCI image, as well as the PCS used for each sample, is found in Table 4.2.

Table 4.2: Summary of mixed images from each notch sample

Sample	Diffractive Mode	Reflective Modes	PCS (mm)
PNG2	<i>L-L</i>	<i>TL-T, TT-T</i>	218.7
PNG4	<i>L-L</i>	<i>TL-T, TT-T</i>	297.2
PNG6	<i>L-L</i>	<i>TL-T, TT-T</i>	327.5

4.5.1. Partial-Weld Imaging

Mixed TFM and PCI images for samples PNG2, PNG4 and PNG6 were generated using the diffractive L-L mode and reflective TL-T and TT-T modes. The resulting images are found in Figure 4.12, with images from each sample across the rows and the TFM and PCI images on the left- and right-hand columns respectively as labelled. Both TFM and PCI images are shown in a linear colour scale, with TFM normalised to each image maximum, and PCI normalised to the maximum possible phase coherence – shown on a 0% to 25% scale. The PCS values used to generate each image is as defined in Table 4.2.

Figure 4.12(a) and (b) highlight the mixed image from the shallowest notch (97.5 mm from the backwall), simulating a LOSWF defect in the latter passes of the welding process. It is clear from both images that the notch can be resolved clearly. However, the PCI indicates a better contrast between noise and notch response. There is also little to no contribution from the weld geometry in both images.

The images of notch placed at the centre of the weld (65 mm from the backwall) – around halfway through the welding process – shows similar characteristics to the notch 92.5 mm from the backwall. Figure 4.12(c) and (d) both indicate the presence of the notch, however, the TFM lacks the ability to resolve the full body of the notch, and instead a top-tip diffraction indication dominates. Less clearly is the presence of the

bottom tip-diffraction. Measurement of the separation of these indications presents a notch height of 5.6 mm, which is accurate to within a millimetre of the true notch size. Conversely, the PCI image shows the full notch face, but the indication is spread over a larger area, suggesting a greater notch size.

Additionally, significant reflections from the unfilled bevel can be seen at the top of these images. These encroach below the weld fill in the PCI image, but with a relatively low coherence value relative to the notch. Reflections in the TFM image also encroach below the weld fill, but again with an amplitude less than 50% that of the notch response.

Finally, Figure 4.12(e) and (f) display images from the deepest notch (32.5 mm from the backwall). Again, clear notch responses are seen in both the TFM and PCI images. Again, responses from the weld geometry are also seen, which encroach below the weld fill in both images. However, like images from the previously discussed sample, the response is low relative to that of the notch response.

The images of each individual mode and view used to generate these images can be found in Appendix B.

It is therefore clear that using the method outlined in this work, simulated LOSWF can be clearly and accurately detected in mock partial narrow gap samples at various points in the welding process.

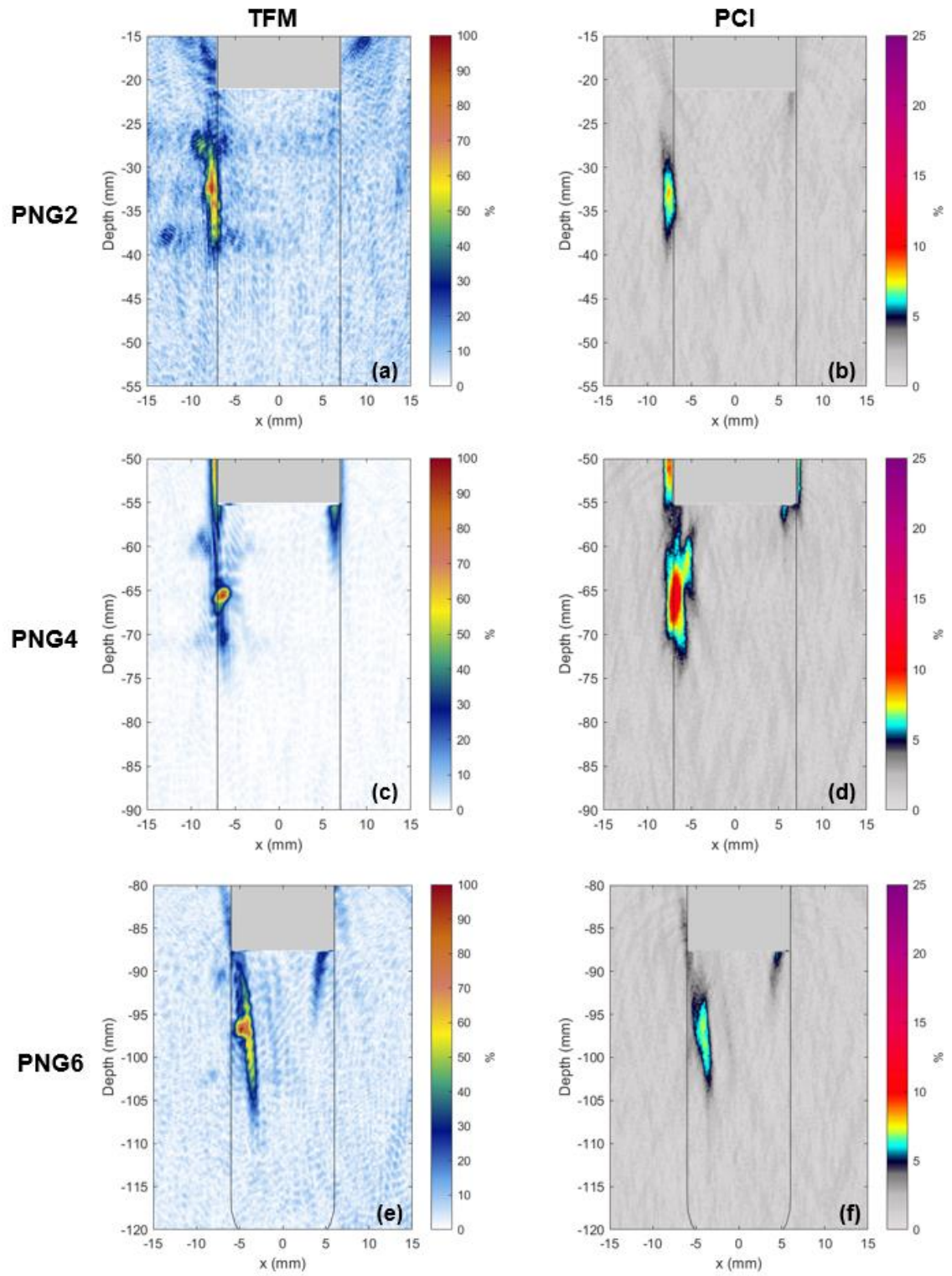


Figure 4.12: Mixed TFM and PCI images of simulated LOSWF in mock partial narrow-groove samples using 1/3 weld fill PCS definition

4.5.2. Weld Geometry Reflections

The images presented in the previous section display minimal geometric responses, with arguably little or no impact on the resolution of the notch. However, it is important to understand the impact of geometric indications so as to avoid occurrences of defect masking or false positives. Reflective responses from the weld geometry will likely cause minimal disruption to the inspection integrity, as they appear along the unfilled bevel. The problematic response would be diffractive in nature, emanating from the corners of the partial weld cap. To understand this, diffractive responses from both the weld geometry and the notch were compared. Amplitude values were obtained using the direct longitudinal mode (L-L), as this elicited the greatest diffractive effects from both the weld geometry and notch defect.

The geometric response amplitude for the three weld heights presented in this study were obtained by inspection of samples PNG1, PNG3 and PNG5. As no notch was present in these samples, responses seen around the partial weld cap must be from the geometry itself. The greatest responses were observed at the corners of the partial weld cap in pulse-echo views. The amplitude of notch tip-diffraction effects were observed in samples PNG2, PNG4 and PNG6.

Figure 4.13 shows the amplitude comparison, linearly normalised to the maximum observed amplitude. It is clear in each sample that the notch response is greater than the weld geometry response in each sample, with an average notch-to-weld response ratio of 6.5 dB.

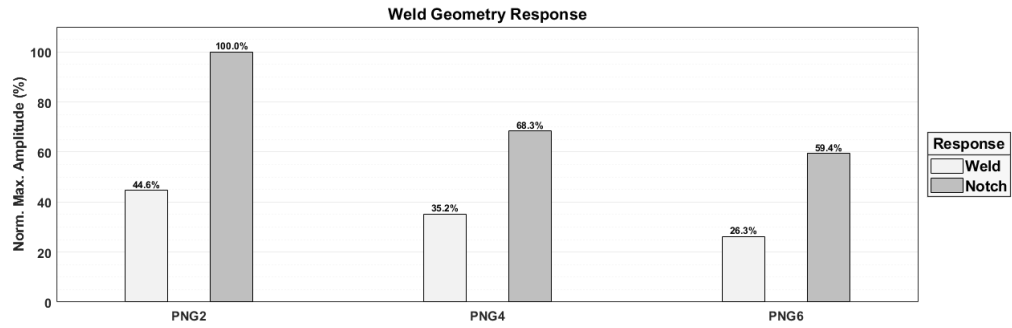


Figure 4.13: Diffractive response amplitude from the weld geometry and notch tips in each mock partial narrow gap sample

It should be noted that the samples presented in this case are considered ‘worst-case’ in terms of weld geometry, as the unfilled weld corners are machined at a right-angles. In reality, the partial weld cap corners will not be as ‘sharp’, due to the behaviour of the liquid weld pool during solidification. It can therefore be hypothesised that for a real-weld geometry, the notch-to-weld response ratio will be greater. An exaggerated schematic of a less sharp weld cap can be seen in Figure 4.14.

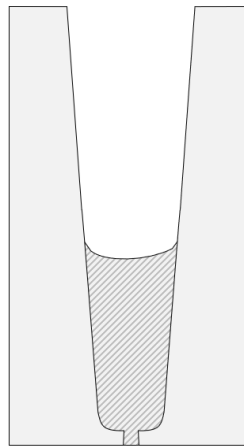


Figure 4.14: Exaggerated weld cap of partially filled geometry

4.5.3. Mode-Converted Diffraction

Mode-converted through-transmission imaging has been investigated for TOFD techniques for improved dead-zone imaging [113, 114]. This considers direct modes with mode-conversion (either L-T or T-L). The advantage of this for TOFD is that the low-velocity of the shear leg increases the time between the lateral wave and diffracted wave – reducing dead zones typically seen with traditional TOFD.

This same method can be applied to the pitch-catch imaging of the dual-tandem method. In full-depth cold scans, this would have the same effect of reducing the lateral wave dead zone associated with TOFD [155]. However, the technique can also be applied to partial weld geometries, by increasing the time between diffracted waves and weld reflections. The main issue with this approach is the ‘leaking’ of other mode converted signals into the image, which can introduce the possibility of false-positive defect reports.

Figure 4.15(a) shows the standard L-L pitch-catch image, showing top and bottom tip-diffraction of the EDM notch. Figure 4.15(b) and (c) show the mode converted diffracted signals – L-T and T-L respectively. Although relatively lower in amplitude than the L-L mode, tip-diffraction can also be clearly seen. Additionally, geometric reflections from the partial weld also appear to be reduced. However, a significant number of additional responses are present in the images, in turn creating potential dead zones. This may not be an issue when considering in-process inspection, given that the dead zone does not interfere with the current pass being inspected.

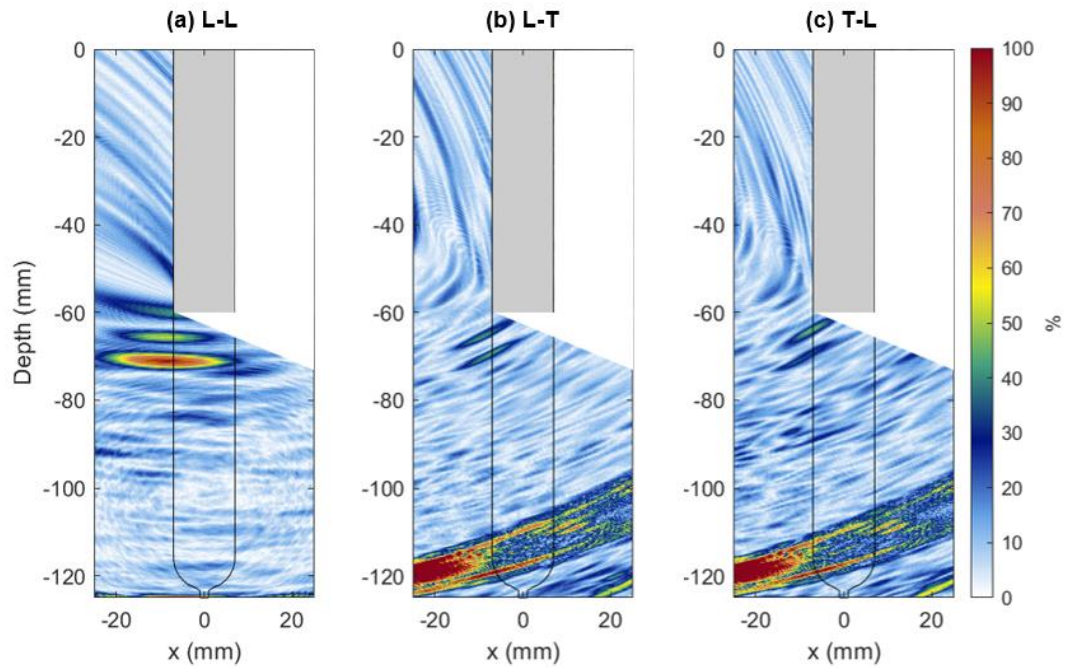


Figure 4.15: Pitch-catch TFM images for sample PNG4 using mode (a) L-L, (b) L-T and (c) T-L

The possible advantage of using mode-converted waves for pitch-catch imaging is therefore clear, and would merit consideration for future work in this field.

4.6. Conclusion

The ability to detect and correct defects during the welding process suggests obvious benefits to manufacturing costs and efficiency, particularly for thick-section welding techniques such as narrow gap. However, geometrical reflections observed from partial weld geometries have the potential to mask or provide false-positive defects. A dual-tandem phased array inspection method has been shown to provide good LOSWF detection sensitivity for partial weld geometries.

A PCS study based on amplitude and phase coherence has provided an inspection plan to maximise inspection sensitivity as the weld is filled, with good defect detection

sensitivity for weld passes across the full weld thickness. This is achieved using a dual-aperture FMC acquisition method, in addition to an adaptive path-finding delay law calculation algorithm to compensate for the partial weld geometry. This has been shown with advanced offline image processing algorithms such as TFM and PCI, coupled with multi-mode image mixing techniques, to precisely and clearly detect LOSWF type defects in a partial weld geometry.

Chapter 5

Single-Bit Coded Excitation for Lightweight Ultrasonic Imaging

5.1. Introduction

Despite the advantages to image quality provided by FMC and subsequent post-processing techniques, there is a subsequent negative effect on both data transfer rates and processing times relative to traditional phased array methods. This is further exacerbated when considering multi-array systems, such as the dual tandem method discussed previously in this thesis. Therefore, the streamlining and compression of data is an issue that must be addressed when considering real-world applications of advanced imaging algorithms utilising FMC datasets.

The NDT process can be performed at various stages of a component's lifecycle – from in-process inspection during heavy pipe welding [86, 179], to resin monitoring during epoxy curing in composite materials [180]. This is vital for critical components in nuclear, petrochemical and renewable fields, with inspections performed regularly to ensure component integrity, and requiring the streaming and real-time processing of large datasets. This can be costly in terms of both the hardware and computational power

required to generate images in real-time. Additionally, inspection data is often required to be retained for several decades to allow for lifetime monitoring and analysis of structural health. It is often impractical to store such large quantities of raw FMC data, and only processed images are saved, which limits future data analysis. These standards are often dictated by independent regulators, such as the Office for Nuclear Regulation (ONR) in the UK.

There is a clear benefit to compressing stored data to the point where information can be as comprehensively analysed in the future as at the time of inspection, while limiting storage space. Numerous methods have been proposed to achieve this for ultrasonic inspection, such as leveraging the reciprocity of the FMC dataset to nearly halve the data required to be collected [181, 182], termed Half Matrix Capture. Other signal processing techniques such as Compressive Sensing [183] have been shown across a number of fields for data compression, and applied to ultrasonic testing data [184]. The use of sparse phased arrays [185, 186] seeks to minimise the volume of data acquired while maximising information obtained through selective element firing. This has been shown to be effective for 2-dimensional arrays [187], where both acquisition times and processed data can be large. However, this is often at the cost of image resolution and the creation of grating lobes. Other notable compression techniques include parameter extraction [188, 189] and domain transformation [190].

However, it may be the rise in popularity of phase-based imaging that lends the simplest solution to ultrasonic data compression – namely PCI imaging using the Sign Coherence Factor (SCF). As this algorithm considers only the sign of each sampled time point,

rather than the phase itself, binary quantisation of data is possible. In turn data storage can be reduced to a single-bit per time-sampled point [143]. In turn, reduced hardware requirements and faster processing are possible, as well as limiting transfer rates and the volume of data required to be stored.

A further challenge observed when considering inspections using FMC acquisition is the low energy transmission relative to other phased array methods. This challenge is intensified in scattering or layered material inspection conducted in NDT applications – for example, in austenitic metal alloys [191]. Despite advantages in post-processing focusing ability, FMC acquisition can often result in low SNR for an individual time signal as only a single element is fired at any one time. This is particularly exaggerated at high element count and low pitch arrays required to provide useful focusing in post-processing. Particularly when attempting acquisition for the purpose of PCI, this can significantly hinder imaging performance as low-amplitude responses may not be distinguishable from the noise floor, reducing the accuracy of phase coherence calculations. This issue may be further exacerbated when extended to attenuating materials or inspections involving large ultrasound travel times.

Typically, increasing the dynamic range of an ultrasonic system will result in greater signal resolution, and as such there have been numerous attempts to developed methods for improving the dynamic range of ultrasound acquisition. One such method is the simple averaging of several consecutive ultrasonic signals which can increase the dynamic range by up to $3N$ dB for every 2^N averages, for an integer N . Additionally, coded excitation has been shown to improve ultrasound SNR by over 20 dB through

increasing the average power of a transmitted waveform [192-194]. Despite seeing limited deployment in NDT, it has been shown that by implementing orthogonal Golay-based coded excitation, the dynamic range of TFM imaging in steel can be maintained through dry coupled media without compromise to range resolution or acquisition time [195].

It is clear that both PCI and coded excitation have individually demonstrated unique advantages when approaching advanced ultrasonic imaging techniques. However, these have not yet been implemented together. This work will show that there are a number of benefits attainable by combining these methods.

Firstly, implementing both PCI and coded excitation techniques indicates the potential for data size reduction, by combining the single-bit nature of PCI with the pulse compression techniques of coded excitation. Additionally, work by Isla and Cegla [196] has previously demonstrated higher data rates and throughput using binary receive data with coded excitation. If stored before pulse compression, data can be stored compactly with single-bit precision, with the possibility of high frame rate and low latency imaging.

Furthermore, hardware simplification is possible, firstly due to SNR gains offered by coded excitation, allowing dynamic range to be preserved at low voltages and removing the requirement for high-voltage pulsers. The use of Analogue-to-Digital Converters (ADCs) can be replaced by simplified hardware suitable for single-bit digitisation, such as comparators.

This work will show that through single-bit digitisation of FMC data using coded excitation, PCI images of notch tip-diffraction using phase coherence can be generated with high SNR. Additionally, it will be shown that pulse compression of the single-bit coded excitation signals provides sufficient resolution to generate amplitude TFM images with imaging performance comparable to those generated through standard single-cycle acquisition.

5.2. Coded Excitation

The concept of coded excitation, first discussed at Bell Labs in the early 1950s [197], sought to improve radar range and accuracy through the use of frequency modulated pulses. Application of this technology achieved transmission outputs with orders of magnitude greater energy than traditional pulses, and without any increase to input power [198]. The use of pulse modulation was later applied to medical ultrasound to improve imaging performance [199], and finally to wider ultrasonic phased array use [194]. Nowadays, coded excitation is a term given to a range of pulse compression techniques used to improve the dynamic range of received ultrasonic signals.

Stemming from increasing use within the medical diagnostic imaging field, the first use of coded excitation in NDT was to increase the sensitivity of flaw detection using immersion transducers in pitch-catch configuration [200]. Since, coded excitation has been exploited for many practical NDT applications, including air coupled ultrasonic transducers [201, 202], ultrasonic inspection of carbon fibre polymers [203] and attenuating materials [204], guided waves [205], and thermography [206]. Many

modulation techniques have been presented and discussed for these applications, including chirps [207, 208], Barker and Golay [209, 210] code excitation.

Coded excitation involves the transmission of a long coded pulse, from which a coded received signal is obtained. The peak transmission power remains constant, but the average transmission power is increased with the longer pulse relative to single cycle transmissions. Using pulse compression techniques, the received signal is decoded, resulting in a higher SNR and resolution signal.

This work will focus on the use of complementary Golay series for pulse modulation [211]. Unlike the majority of pulse compression techniques, excitation using complementary Golay pairs can suppresses the formation of sidelobes. Golay pairs can be generated using a recursive algorithm [212], resulting in sequences of 2^N cycles, where N is an integer number. Furthermore, the ability to perform pulse compression using binary excitations can provide benefits in simplified pulse generation architecture design, contrary to other coded excitation methods which require high level pulsers. An example of a $2^{N=2}$ cycle Golay pair is shown in Figure 5.1.

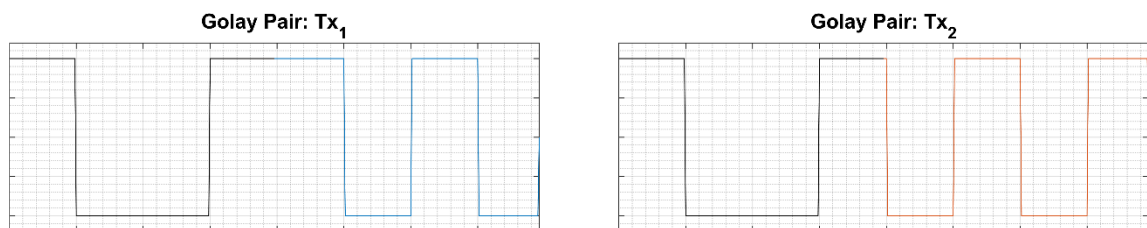


Figure 5.1: Example of 4 cycle complimentary Golay pair

To implement Golay excitation with an FMC acquisition, a traditional single transmission pulse is replaced with two subsequent transmissions, taking the form of

each Golay pair, Tx_1 and Tx_2 . The overall transmission number is therefore doubled, and in turn so too the number of received signals.

It is the similar yet inverse nature of these waveforms that together allow sidelobe suppression to be achieved. This can be demonstrated by considering the correlation of each transmission waveform with their matched filters Rx_1 and Rx_2 . The autocorrelation functions obtained from each waveform can then be summed, with constructive addition of the main lobe, and cancellation of sidelobes. The result is a compressed waveform Rx_p with reduced peak sidelobe level. This process is shown visually in Figure 5.2.



Figure 5.2: Demonstration of sidelobe suppression by the sum of two complimentary Golay functions, resulting in a single main lobe

In reality, the matched filters are replaced by the received time-trace, and a compressed time signal Rx_p is obtained. This process is conducted for each pair collected during the FMC acquisition, resulting in a compressed dataset. The expression for processing a single pair is given in (5.1)

$$Rx_p = (Tx_1 * Rx_1) + (Tx_2 * Rx_2) \quad (5.1)$$

The SNR improvement using this method is two-fold; a 3 dB improvement is observed from the averaging of two time signals, with a further 3 dB increase for each increment

of N [213]. The SNR improvement expected from an N -cycle Golay transmission is given as the expression in (5.2) [195].

$$\Delta SNR = 3(N + 1) \text{ dB} \quad (5.2)$$

Although the number of transmission events is doubled, the net acquisition time can remain unchanged by selecting mutually orthogonal Golay pairs. This allows two waveforms to be transmitted simultaneously without interference, allowing them to be separated during pulse compression [195, 210, 214].

One drawback of pulse modulation arises when considering large cycle numbers, which increases the dead zone directly after transmission. The length of this dead zone is proportional to the number of cycles used, and can prevent detection of near-source reflectors. However, in most NDT applications, immersion or acoustic wedge delay lines are used to introduce a stand-off between the array and inspected specimen. This provides an effective time delay medium such that the dead zone does not impact the desired inspection area.

PCI, as discussed in Section 2.5.3 of this thesis, is a phase-based imaging technique which can consider only the sign of a received signal. The binary nature of the wavelet sign suggests that the effects of attenuation can be removed for shallow defects, given that the signal can be distinguished from the noise floor. For signals with larger travel times, there will come a critical point where the noise dominates the wavelet and the sign is no longer consistent, reducing the coherence of phase across the dataset.

Therefore, the phase coherence of a signal should remain independent of attenuation, such that it occurs before a ‘cut-off’ point where the signal falls beneath the noise floor.

Each sample point can be sufficiently stored as a single-bit digit by conversion to sign in hardware, greatly reducing the amount of data required to be transferred and processed [143]. Applying this process in acquisition hardware would remove the requirement of high-resolution ADCs to obtain a digital signal. Instead, these could be replaced by a simple comparator - reducing the complexity, size and cost of necessary array controllers. Similarly to the method described above for software processing, the comparator compares an input voltage V_{In} to a reference voltage V_{Ref} . Depending on the polarity of the input relative to this reference, either a positive or negative saturation voltage V_{Sat} is applied to the output. The result is a binary signal with minimal processing which can be used for PCI imaging.

One important practical consideration for this hardware implementation is the presence of a DC offset. This can offset the polarity of single-bit data and lead to incorrect sign values. If the DC offset is larger than the noise level, the ability to determine noise by the summation of phase values is removed, as they will constructively sum to a perceived large coherence. It is therefore imperative that the DC offset is removed from the analogue signal prior to digitisation by the comparator.

5.3. Experimental Procedure

In order to perform and collect coded excitation data, a tri-level excitation capable phased array controller (FIToolbox[®] from Diagnostic Sonar Ltd., Livingston, UK [215])

was used. This allowed controlled excitation of a 5 MHz 64-element linear phased array (Olympus 5L64-A32) with a 60% fractional bandwidth.

Data acquisition using the FIToolbox[®] array controller was performed using a LabView [170] interface, allowing manipulation of ultrasonic controls including the excitation waveform required for coded excitation.

Received data was sampled at 50 MHz, and digitised through a 12-bit ADC. This was then interpolated to 16-bit for ease of writing to and reading from file, with single-bit digitisation performed in post-processing software. This allowed for direct comparison of conventional data bit-depth and single-bit using the same dataset, with quantisation done in software rather than hardware. This was under the assumption that quantisation in post-processing would produce the same binary signal as would be acquired through hardware quantisation.

Data processing, including pulse compression and imaging, was conducted in MATLAB (The MathWorks Ltd., Natick, Massachusetts) 2023a, and accelerated with parallel CPU and GPU processing toolkits [172-174].

The test piece used in this work was designed to simulate an inspection where the use of single-bit PCI with coded excitation could be applied. PCI has been shown to increase detection and sizing capabilities of crack-tip diffraction [139], and so imaging of tip diffraction was determined to be a suitable benchmark to test this work. Furthermore, to ensure that dead zones associated with Golay transmission did not inadvertently hinder

imaging at higher cycle numbers, the defect should be placed sufficiently far from the array position.

A 5.0 x 1.0 mm notch was placed in a 125.0 x 500.0 x 300.0 mm 1018 steel block, in order to mimic a planar defect. This was positioned 27.5 mm from the backwall, relative to the centre of the notch. The array was placed at a horizontal offset of 55.0 mm from the centre of the notch, as shown in Figure 5.3. Data from both standard single-cycle excitation, as well as Golay excitation utilising 2 to 128 cycles were acquired through an FMC acquisition process. Given the ToF from the array to the notch, the maximum number of cycles before the dead zone begins to enter the domain of the notch is 128 cycles.

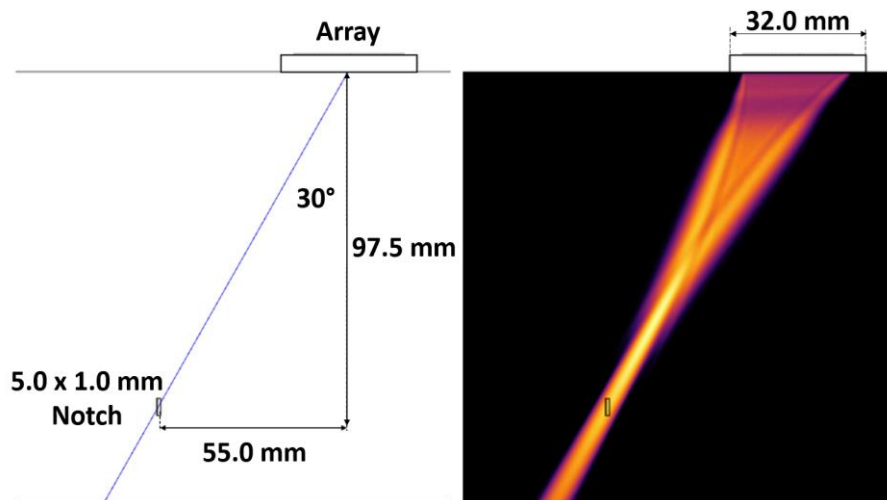


Figure 5.3: Experimental setup for data collection, showing the offset of a phased array probe from a rectangular notch (left) and beam profile when the full aperture is focused at the notch centre (right)

5.4. Pulse Compression

The Golay excitation waveform can be transmitted in a number of formats. Typical transmission is conducted by tri-level systems, which allows the transmission of pulses with a positive or negative polarity of 1, and zero. By considering a pulse width of 100% of the wavelength, such that a perfectly square pulse is considered, a single-bit transmission can be defined in single-bit format.

As previously mentioned, data was digitised using a 12-bit ADC and stretched through interpolation to 16-bit for the purposes of saving the data to file. This was quantised digitally in post-processing software to obtain the single-bit format. As discussed, this is also possible to do with hardware alone, by digitising using a simple comparator as a single-bit ADC.

Once FMC data is acquired using Golay excitation, each element-pair is associated with two receive signals Rx_1 and Rx_2 . Both the uncompressed and compressed receive data for a single element-pair is shown in Figure 5.4, using both 12-bit and single-bit data from the same original dataset. The compressed signal generated from the single-bit receiver quantisation retains much of the amplitude information seen in the 12-bit compressed signal, however it exhibits a longer dead zone. This is caused by the amplification of the element ‘ringdown’ during quantisation, and remains consistent until reaching the noise floor. For this reason, the bandwidth and dampening properties of the array are important to determine the size of this dead zone extension, regardless of Golay cycle number.

The single-bit correlation function measures the correlation in the phase of the excitation pulse and its received signal at each cycle in the transmission. High amplitude is seen when there is a strong phase match between the transmission cycles and reception, with low amplitude when there is little phase correlation, e.g. at points containing incoherent noise.

Although the individual compressed A-Scans generated from single-bit quantisation exhibit poor SNR and no obvious defect indications themselves, they can still be used with delay-and-sum imaging algorithms such as TFM and PCI to generate an image of a reflector. Given that received reflector responses are coherent in phase across a given FMC dataset, random noise is suppressed as its phase is also random. This results in a SNR which is proportional to the number of A-Scans used in the imaging algorithm.

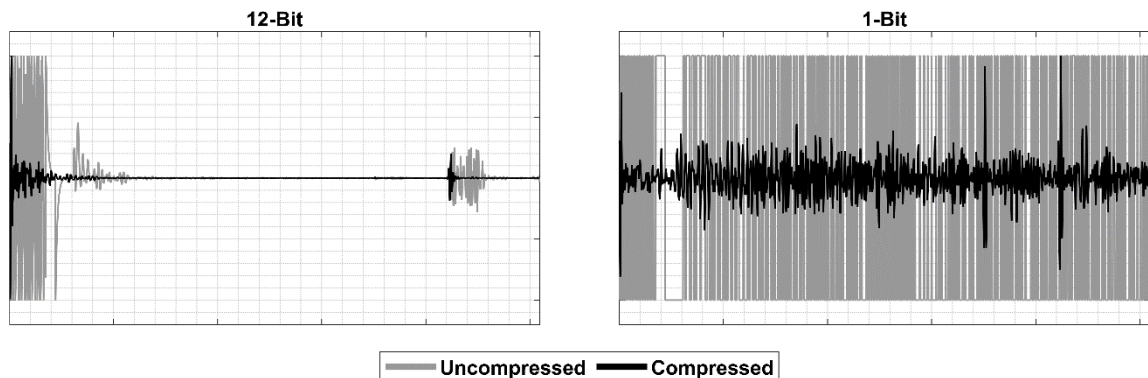


Figure 5.4: Demonstration of pulse compression using 12-bit (left) and single-bit (right) receiver quantisation and receive signals from the same dataset. The raw signal is shown in grey, with the resulting compressed A-Scan highlighted in black.

5.5. Compression SNR Analysis

In order to understand the effect of quantising received data prior to pulse compression, the top tip diffraction response from the EDM notch was studied. SNR was calculated by

considering the maximum response from the backwall signal, with the noise calculated using the root-mean square. The noise region was considered from the point at which ring-down of the transducer had reached the noise floor, to before the backwall indication.

For the 12-bit receiver quantisation, the resulting SNR of this response was 18.0 dB, with the single-bit receiver quantisation data producing 14.5 dB SNR. This reduction is expected, as the data bit-depth is significantly reduced.

However, this suggests that despite a significant reduction in bit-depth of input data, from 2^{12} to 2^1 , a large amount of data is retained and exploited during pulse compression – with unexpectedly low impact on processed time signal SNR. It appears that although the input received signal is binary in nature, data is still maintained across the pulse length. It can be theorised that increasing the number of cycles in transmission will increase the bit-depth of the processed data.

This study was expanded by observing the SNR of the backwall response for varying numbers of Golay excitation cycles, using both 12-bit and single-bit inputs. Transmissions of Golay cycles from 2 to 128 were used, with a duty cycle of 100%, the results of which are graphically shown in Figure 5.5.

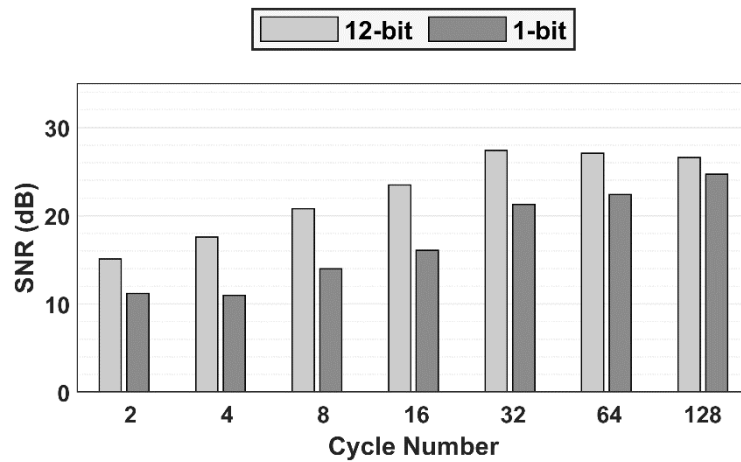


Figure 5.5: SNR Analysis of backwall indication utilising 12-bit and 1-bit receiver quantisation data with 100% duty cycle

Theoretically, it is expected that with each doubling of cycle number, there should be a 3 dB increase in SNR. This is explained by the root-sum square nature of the summation of two noise signals, which leads to a $\sqrt{2}$ reduction in noise and translates to a 3 dB SNR increase.

The 12-bit receiver quantisation data follows this 3 dB trend up to and including the use of 32 cycles, after which the SNR plateaus. Interestingly, the single-bit receiver quantisation data does not follow this trend. Despite showing little SNR improvement at low cycle numbers, the SNR continues to rise with increasing cycle number.

The plateau of this trend is likely due to an asymmetry between positive and negative transmission cycles of the complimentary Golay pair. Any asymmetry between positive and negative excitation pulses will lead to imperfect compression, and therefore reduced performance in the cancellation of sidelobes. It has been shown that this asymmetry can occur from the finite time required for the pulser to change the transmission polarity, termed 'rise time'. These non-zero rise times are particularly applicable when

considering square pulses in this case [216]. It should be noted that pulse compression degradation of Golay code has also been attributed to the generation of noise due to inadequate quantisation of received signals [217], signal aliasing and doppler effects of large scanning speeds [216], as well as nonlinearities [218], which should not impact pulse compression integrity in this work.

It is likely that once the SNR is sufficiently high, this degradation begins to dominate the noise level and prevents further SNR improvement. However, when considering compression using single-bit inputs, only asymmetric polarity is considered, which has less of an effect on compression degradation as the square wave is more closely preserved in reception. Therefore, the SNR continues to improve with increasing cycle numbers.

Considering the same study, instead with a 71% duty cycle, we observe the trend seen in Figure 5.6. The SNR no longer plateaus at higher cycle frequencies for the 12-bit receiver quantisation, and the 3 dB SNR increase is approximately observed. There is a mean 4.0 dB difference in SNR value between the 12-bit and single-bit receiver quantisation across this trend.

The 100% duty cycle assumes the pulser switches polarity across a single sample point. However, physically this is not the case and therefore leads to a breakdown during pulse compression. The 71% duty cycle attempts to align with the natural cycle of the pulser, and follows the desired input signal resulting in lesser pulse degradation.

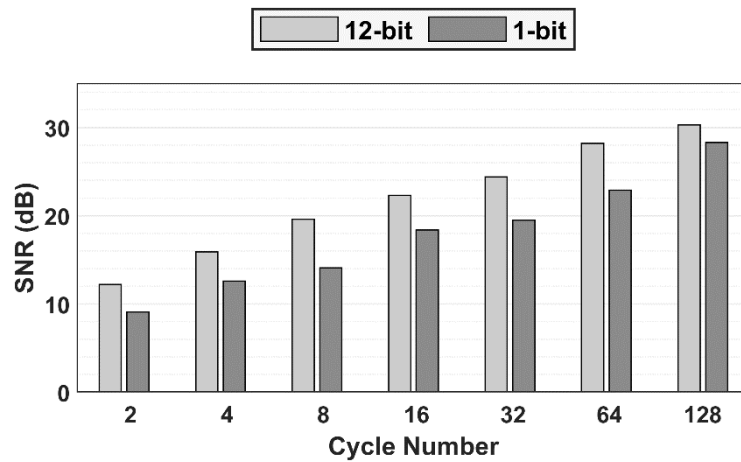


Figure 5.6: SNR Analysis of backwall indication utilising 12-bit and 1-bit receiver quantisation data with 71% duty cycle

Furthermore, the pulser may not be able to provide a consistent voltage at high cycle numbers, with the power depleting over the pulse time. The ‘on’ time of the pulser for the 100% duty cycle is greater, and therefore this effect may be of higher significance and impact lower cycle numbers than that of the 71% cycle.

Despite the loss of SNR when considering a single-bit receiver quantisation, a notable benefit is obtained through the reduction in data size. The use of Golay coded excitation doubles the data size due to the double firing requirement, however, there is a factor of 6 reduction in memory usage when compressing data at single-bit from 12-bit. This suggests that processing and streaming data would improve in efficiency by a factor of 6. Particularly when considering the large number of frames acquired during component scanning, the memory saved by using single-bit data is sizeable.

There is therefore a trade-off when approaching these methods. Reduced data sizes and processing times associated with single-bit acquisition introduces an SNR reduction.

However, for inspection cases where this approximate 4 dB reduction is acceptable, single-bit acquisition is preferable.

This data reduction can be simply quantified. Considering 2000 FMC frames from a 64-element probe, each containing 4096 time signals (double when considering Golay pairs) with 1000 sampled points each, there is an obvious 6-factor reduction in data size, as shown in Table 5.1.

Table 5.1: Quantification of data size reduction using single-bit processing

	12-bit		1-bit	
	Single	Coded	Single	Coded
Excitation	Single	Coded	Single	Coded
A-Scan Number	4096	8192	4096	8192
Sampled Points	1000	1000	1000	1000
Number of Frames	2000	2000	2000	2000
Data Size (GB)	11.44	22.89	0.95	1.91

It should be noted that this study was conducted using FMC data, and therefore single-element firing. As such, the backwall indication is contained well within the dynamic range of the 12-bit ADC and just above the noise floor. This was done in order to ascertain the behaviour of coded excitation and single-bit digitisation techniques for this imaging case.

5.6. Imaging

5.6.1. PCI Imaging

After pulse compression, the sign can be calculated and a PCI image processed as previously discussed. It should be clarified that due to the nature of the PCI algorithm,

all PCI images can be generated using single-bit data, as only the polarity is used for generation.

In order to determine the effectiveness of imaging using single-bit Golay processing, a standard single cycle dataset is used as a benchmarking reference. The single cycle data was acquired with a transmission voltage of 80 V and 48 dB of gain in reception, such that the first backwall signal was unsaturated and fully contained within the dynamic range.

A PCI image of the same 5.0 x 1.0 mm notch from sample specified in Figure 5.3 formed from this data is shown on the left of Figure 5.7 from a single cycle transmission dataset. As is the case with all PCI images, the image is normalised to the maximum possible coherence, which in the case of a 64-element FMC dataset is 64^2 or 4096. Both the top and bottom tip diffraction indications are clearly seen, and demonstrates the ability of PCI to resolve diffuse reflectors. Sizing the notch from this image using the maximum value from each tip provides an accurate measurement of the extent of the notch in the depth axis.

Now considering data obtained from a 16-cycle Golay transmission, a comparison between images generated using 12-bit and 1-bit pulse compression can be made. Again, acquisition was performed with an 80 V excitation and 48 dB gain. Figure 5.7 contains two PCI images, formed from a 12-bit (middle) and 1-bit (right) receiver quantisation respectively. The 12-bit receiver quantisation shows similar quality to the single cycle dataset, with both top and bottom tip diffraction well resolved, and the ability to size

accurately. The 1-bit receiver quantisation resolves the top tip well, however the bottom tip is not as prominent.

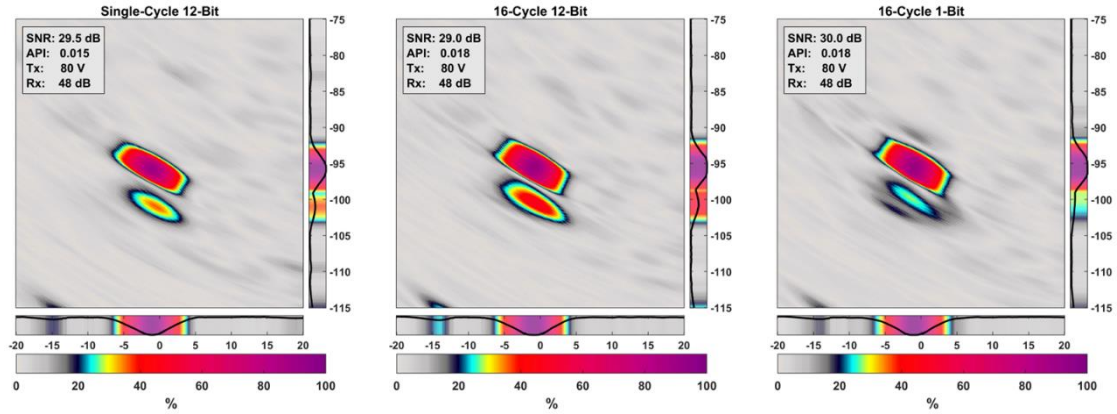


Figure 5.7: PCI images processed from single cycle and 16-cycle Golay FMC datasets with 80 V excitation and 48 dB gain. Images from single-cycle 12-bit data (left), 16-cycle 12-bit data (middle) and 16-cycle 1-bit data (right) are shown. The SNR, API, Tx voltage and Rx gain are presented for each image.

5.6.2. TFM Imaging

Due to signal resolution recovered during pulse compression of binary inputs, it may be possible to perform amplitude-based imaging using TFM. As outlined in Section 2.5.2 of this thesis, TFM is an amplitude-based imaging method for post processing of FMC datasets.

Firstly, a reference TFM image can be formed from the single cycle dataset, and is shown on the left of Figure 5.8. The noise measurement for SNR calculation was based upon the top-right area of each image, such that no notch or backwall indication was considered. The signal was measured to be the maximum value of the top-tip indication of the notch.

The image is linearly normalised to the top-tip indication amplitude, which has an SNR of 35.7 dB. The diffraction indication from the bottom tip of the notch is much lower in amplitude than the top, at around 9% relative amplitude.

Now considering the 16-cycle Golay transmission data, with both 12- and 1-bit compression inputs, we can resolve the TFM images observed in Figure 5.8. The 12-bit receiver quantisation image shows similar image quality, with a bottom tip relative amplitude drop of ~93%. However, the TFM image observed from the single-bit receiver quantisation also shows similar quality. This shows that despite two single-bit inputs, information stored within the received signal's sign can produce a sufficient resolution signal after pulse compression to image based on amplitude. The relative amplitude of the bottom tip in this image is 5.8%, not significantly less than the 12-bit receiver quantisation.

The 12-bit input image exhibits an SNR of 39.5 dB, with the 1-bit input exhibiting a slightly lower SNR of 37.5 dB. It should also be noted that the 12-bit image contains reflections from the backwall in the bottom-left of the image. These are absent in the single-bit image, however this is likely due to the reduced sampling resolution, rather than an imaging improvement.

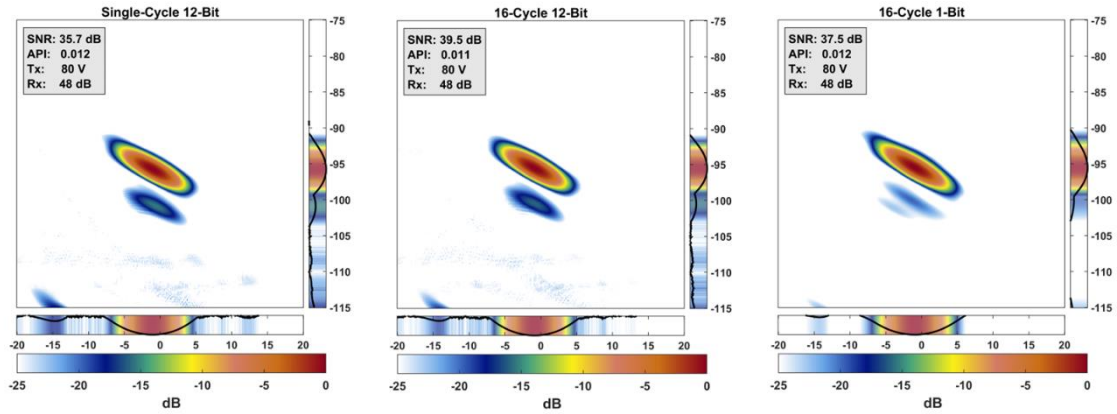


Figure 5.8: TFM images processed from single cycle and 16-cycle Golay FMC datasets with 80 V excitation and 48 dB gain. Images from single-cycle 12-bit data (left), 16-cycle 12-bit data (middle) and 16-cycle 1-bit data (right) are shown. The SNR, API, Tx voltage and Rx gain are presented for each image.

Given that these images were produced from the same raw dataset, no coupling or orientation variations can be contributed to the SNR difference. Therefore, the binary quantisation is the only parameter in the imaging process that could enact this change.

5.6.3. Low Voltage Excitation

The benefit of coded excitation in this case is the observed increase in dynamic range. It follows that a reduction in the transmission voltage should be possible without a dramatic reduction in SNR. Theoretically, for each halving of the input energy, an equivalent gain increase of 6 dB can be applied to counteract the energy drop, such that utilisation of the dynamic range remains constant. Therefore, for a reduction in excitation voltage to 10 V from 80 V, a gain of 66 dB should be applied. A dataset was acquired to this effect to observe the low voltage effects of single-bit pulse compression on PCI imaging.

Figure 5.9 shows the 12-bit and 1-bit receiver quantisation PCI images at low voltage excitation. The 12-bit image demonstrates a performance similar to the equivalent 80 V image, with both top and bottom tip diffraction resolved to within 12 dB of the maximum coherence value. Again, however, the single bit image fails to resolve the bottom tip to the same coherence, despite a clear top tip diffraction signal.

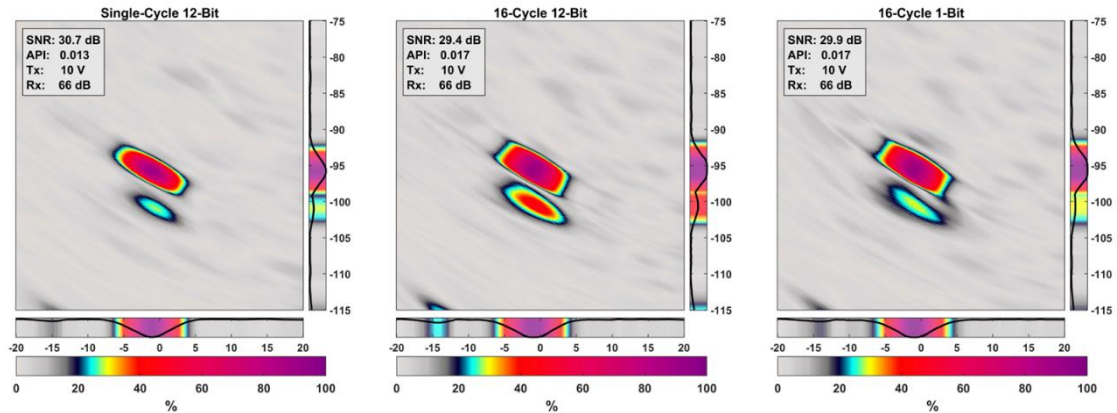


Figure 5.9: PCI images processed from single cycle and 16-cycle Golay FMC datasets with 10 V excitation and 66 dB gain. Images from single-cycle 12-bit data (left), 16-cycle 12-bit data (middle) and 16-cycle 1-bit data (right) are shown. The SNR, API, Tx voltage and Rx gain are presented for each image.

The drop in coherence of the bottom tip indication in the 1-bit receiver quantisation PCI image is likely due to the drop of the signal beneath the noise floor across a critical number of time signals within the FMC dataset. As discussed earlier, this results in the phase (or sign) of the indication becoming lost to the noise.

In order to quantify these results, the SNR value of the top tip was measured in each PCI image, and presented visually in Figure 5.11 (top), and numerically in Table 5.2. Images produced through coded excitation exhibit slightly lower coherence overall, relative to the single cycle data. However, when comparing low input voltages to higher initial values, coded excitation exhibits little change in SNR for the 1-bit receiver quantisation.

The independence of gain selection on saturation means that low-amplitude signals can be resolved from the noise floor and their coherence preserved at low voltages.

Additionally, the Array Performance Indicator (API) [122] quantifies the imaging performance based on the ability to resolve a point scatterer. A low API value indicates that the indication approaches a single point, while a larger API indicates spreading of the scatterer response. The dimensionless indicator considers both the wavelength of ultrasound in the medium λ , and the area A_{-6dB} at which the point scatterer response is greater than -6dB. The relationship is shown in (5.3), and discussed in more detail in Section 2.5.7.2.

$$API = \frac{A_{-6dB}}{\lambda^2} \quad (5.3)$$

This allows quantification of the imaging performance across both arrays and imaging algorithms, and relays the ability of the system to resolve a point scatterer, such as a tip diffraction indication from a notch. As observed in Table 5.2, the API is largely unaffected by input bit-depth, excitation voltage or gain when imaging using the PCI algorithm.

The same can be applied to TFM imaging. Figure 5.10 shows the TFM images produced from the 12- and 1-bit receiver quantisation data for a 10 V excitation with 66 dB gain. There is little impact observed on both the relative amplitude and the SNR when comparing these images to their 80 V excitation equivalents. The 1-bit image exhibits the slightly lower SNR of 37.0 dB.

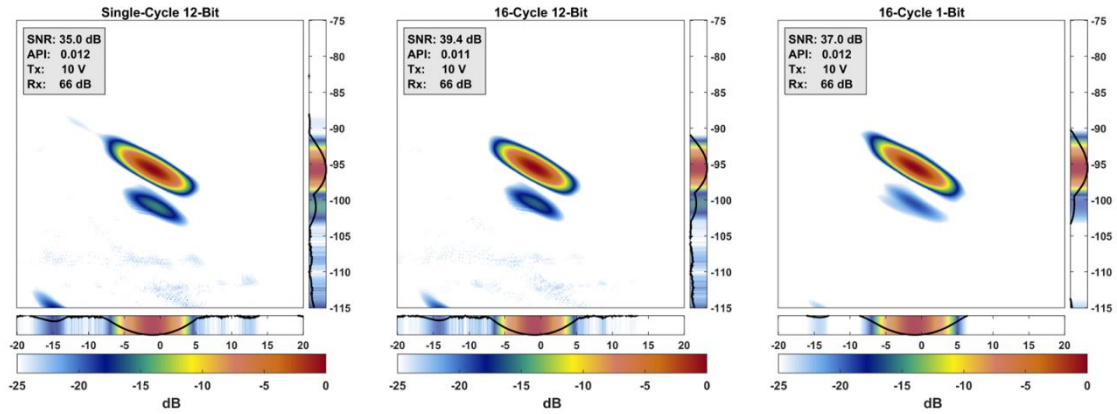


Figure 5.10: TFM images processed from single cycle and 16-cycle Golay FMC datasets with 10 V excitation and 66 dB gain. Images from single-cycle 12-bit data (left), 16-cycle 12-bit data (middle) and 16-cycle 1-bit data (right) are shown. The SNR, API, Tx voltage and Rx gain are presented for each image.

Again, the imaging performance can be quantified and is demonstrated in both Figure 5.11 (bottom) and Table 5.2. It is clear that the 1-bit receiver quantisation images exhibit a close resemblance to the 12-bit receiver quantisation. Similarly to PCI imaging, the API remains unaffected by the TFM algorithm across each dataset. It is interesting to note that the TFM algorithm out-performs the PCI in this regard, with a consistently better API value. It is clear that the 12-bit receiver quantisation images SNR remains fairly consistent, with the 1-bit receiver quantisation SNR remaining higher, with a noticeable drop at low voltage and high gain.

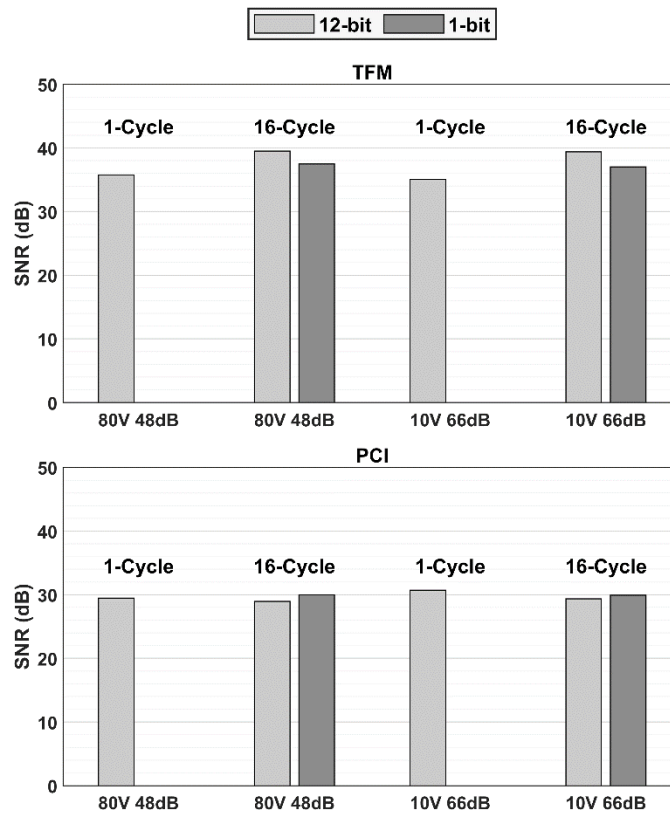


Figure 5.11: SNR Analysis of notch indication in TFM image utilising 12-bit and 1-bit receiver quantisation. This is demonstrated for TFM (top) and PCI (bottom) for both high and low input voltages.

Table 5.2: Quantitative performance of PCI & TFM imaging

	Single Cycle		16-Cycle Golay			
	12-Bit		12-Bit		1-bit	
Tx (V)	80	10	80	10	80	10
Rx (dB)	48	66	48	66	48	66
PCI SNR	29.5	30.7	29.0	29.4	30.0	29.9
PCI API	0.015	0.013	0.018	0.017	0.018	0.017
TFM SNR	35.7	35.0	39.5	39.4	37.5	37.0
TFM API	0.011	0.012	0.011	0.011	0.012	0.012

5.7. Conclusion

This work has shown that the use of single-bit receive data for Golay coded excitation has enabled a new and efficient imaging system for data transfer, processing and storage, with little compromise to image quality. This has been demonstrated for both PCI and TFM algorithms through the use of FMC acquisition. The outcome of this work provides benefits in three key areas:

- Data compression
- Data transfer and processing rates
- Hardware complexity

The compression by use of single-bit receive data can prove beneficial across a number of industrial applications where regulations dictate the storage of historical data over several decades. This would reduce the volume of storage infrastructure required, limiting costs and space. Consequently, data accessibility is more efficient with a greater density of data accessible with the same read speeds. Energy efficiency is also improved with fewer physical storage devices to manage.

In addition to the obvious compression benefits, improved imaging frame rates could be achieved by acceleration of pulse compression and imaging processing. The ability to recover a high resolution received signal from two single-bit inputs allows both PCI and TFM imaging to be performed. Currently, commercial use of TFM is hindered by limited frame rates and costly hardware acceleration required for real-time imaging such as GPUs [219] and FPGAs [220]. However, this lightweight method using coded

excitation could improve transfer and processing times and allow for a wider practical field of view. In addition, fast transfer and processing rates can enhance the sensor-based communication and automation propelled by NDE 4.0 [221].

The third benefit is the savings gained on hardware requirements. High voltage circuitry typically requires larger boards and are more discrete, increasing the hardware volume required relative to standard integrated Circuits (ICs). Additionally, this results in complex hardware requiring localised cooling and high voltage power supplies. By ensuring that transmission and reception operate within the same low voltage range with coded excitation, both the transmission and reception can be handled by the same IC, reducing complexity, board size and power consumption. Furthermore, low-voltage excitation enables the design of an “intrinsically safe” array controller, which could operate in otherwise unsafe conditions for current array controllers. Further benefits of a low voltage system include improvements to battery life, and lesser piezoelectric stresses – prolonging probe lifespan. Additionally, replacing the need for ADCs with simple comparators reduces both the hardware complexity and size. This further increases power efficiency, while reducing latency associated with digitising data with ADCs.

The combination of these factors can provide the foundation for a handheld and intrinsically safe ultrasonic acquisition and imaging system, with manageable power consumption and battery life. The ability to perform high-quality imaging in challenging environments with a lightweight system could prove invaluable across many fields. Examples of this could include use in medical theatres for tissue monitoring during

operation, or by emergency medical services for on-site use. Industrially, applications can range from use in damp conditions experienced in offshore oil and gas inspection, or in renewable energy fields where a handheld device could improve inspection practicality.

However, there are also a number of limitations associated with this work, the most obvious of which is the reduced resolution of stored data. This imposes a restriction on the scope of future data analysis outside the image generation outlined in this work. Furthermore, the use of coded excitation and necessary pulse compression introduces an additional step in the processing of data that must be considered when approaching real-time applications.

This work also assumes that an indication is distinguishable from noise. If this is not the case, such as in attenuating materials or when considering large travel paths, single-bit pulse compression may not be beneficial, particularly at low Tx voltages. Furthermore, a single imaging scenario is presented in this work, highlighting the imaging of tip diffraction from a rectangular notch. Future work in this area must consider multiple imaging scenarios, including probe positioning, reflector type, the inclusion of delay lines, and attenuating media.

Future work to further explore a single-bit PCI and TFM imaging platform using coded excitation would require the design of an array controller with the capability to perform quantisation in-hardware. This would allow complications such as DC offsets and transfer rate improvements to be explored fully.

Chapter 6

Summary

6.1. Conclusions

Current welding and inspection practices are not indicative of the technologically driven culture of the present and future. From both an economical and sustainability perspective, the adopted welding and inspection processes for many heavy manufacturing industries are underperforming due to factors including; large energy requirements, expensive labour costs, schedule uncertainty and process inconsistencies.

An automated welding and in-process inspection system has been proposed as a solution to these downfalls, and forms the basis of the work presented in this thesis. This proposes a consistent automated sensor-driven welding process, leading to reduced rework and reheat costs, reliable component scheduling, assurance of component safety and overall improved manufacturing efficiency. Such a process not only epitomises the innovation encapsulated by NDT 4.0, but could revolutionise the way in which heavy welding manufacturing is done.

However, a number of challenges stand in the way of implementation of in-process inspection. The first is the high-temperatures and temperature gradients experienced due

to close proximity to the weld. A further issue is the presence of geometric artefacts in ultrasonic data due to partial weld geometries.

This thesis has sought to consider the application of in-process weld inspection to that of narrow gap welding. This weld geometry is typically used in high-integrity, thick-section components in the nuclear, oil and gas, and naval industries. Traditionally difficult to inspect ultrasonically, this presented additional challenges not applicable to typical weld geometries.

Firstly, a new ultrasonic setup was required to ensure reliable detectability of defects in a narrow gap weld. The dual-tandem method was proposed and tested, consisting of two opposite-facing phased array probes. This allowed data acquisition of both pulse-echo (considered by most-all phased array inspection systems) and pitch-catch (typically considered by single-element inspection such as TOFD) datasets within a single acquisition sequence using FMC. This enabled advanced imaging algorithms and multi-mode imaging considerations – increasing the likelihood of a defect being detected.

The dual-tandem setup was tested on a range of mock narrow gap samples, with the aim to test the system based on the ability to detect a notch – representative of a typical LOSWF defect found in a narrow gap weld. The probe positioning was optimised based on sensitivity to the defect at various depths, and different imaging modes and views explored using TFM imaging. This demonstrated high sensitivity and detectability relative to a standard inspection, and demonstrated reasonable sizing capability.

This method was then considered for use in an in-process inspection environment. Building on work considering inspection at high temperature gradients using the MSFMM [154], the geometrical reflections observed of a partially-filled weld were considered. To do so, further mock narrow gap samples were designed to mimic welds at various stages of completion, again with added notches. An adaptive probe positioning system was designed to ensure optimum performance as a weld was filled. TFM and PCI imaging algorithms were used with MSFMM TOF calculations, allowing for geometric compensation. Reflections from the unfilled geometry were observed and quantified using the dual-tandem method, and the detectability of notches was determined to be dependent on careful mode choice. Notches could be separated from the geometry and showed a satisfactory relative amplitude using the dual-tandem method.

However, despite the advantages shown by implementing the dual-tandem method for narrow gap weld inspection, the volume of data collected and processed was significant. Therefore, in order to move this method towards an in-process technique, data collection, processing time and stored data volume had to be improved.

A number of data compression algorithms were considered, but the use of a single-bit acquisition system, optimised for PCI imaging, was explored. This would allow digitisation of ultrasonic data based on the sign of the received wave, as an approximation for its phase. It was found that by coupling this acquisition technique with Golay-based coded excitation techniques, pulse compression allowed amplitude data to be recovered from the single-bit data, allowing both PCI and TFM imaging. This

was shown to greatly reduce the volume of data required for transfer and processing. Furthermore, a low voltage, intrinsically safe ultrasonic imaging system with lightweight hardware was proposed.

The culmination of the work in this thesis sets the foundations for a novel ultrasonic inspection system for narrow gap welds. Combined with the single-bit acquisition and coded excitation for data compression, the deployment of the dual-tandem technique as an in-process weld inspection system can improve the efficiency and reliability of manufacturing using narrow gap welds.

6.2. Suggestions for Future Work

In order to progress the work outlined in this thesis, future work should be focused on advancing the dual-tandem method from static, liquid coupled testing to robotic dry-coupled in-process deployment using a high-temperature roller probe [86, 87]. To an extent this is underway, however a number of further challenges must be addressed.

The future work proposed will be separated into three equally important sections; imaging performance, imaging efficiency and mechanical deployment.

6.2.1. Imaging Performance

The defect detection capability of a system is directly related to the imaging performance. Therefore, future development of the work in this thesis would benefit from research of methods which could enhance the ability of the system to detect and represent defects accurately.

Imaging performance could initially be aided by the development of a pre-inspection sensitivity mapping algorithm, allowing efficient mode and view selection, with optimisation of the FMC acquisition method. Currently in this work, this was done by human interpretation, but may be suited to the application of either statistical or machine learning methods. Removing the human element from this process would improve consistency across multiple scans, while removing the opportunity for qualitative human judgement to hinder the optimum performance of the system.

Additionally, the inspection of challenging (coarse-grained and anisotropic) materials may be suited to the increased diffraction sensitivity offered by the dual-tandem method. This is perhaps a necessary endeavour, as many industries use such materials for corrosion resistance, and would require the same defect detectability assurances afforded to the materials used in this work.

Furthermore, the work presented in this thesis considers only the 5 MHz 64-element probe. By doubling the pitch size from 0.5 mm used in this work, to 1.0 mm by firing two elements at once, and halving the element number, the energy transmitted per element firing would increase, and potentially improve SNR. This has been tested and verified by recreating an increased pitch in postprocessing. However, if performed in acquisition, this would reduce the data required to be acquired and streamed, and in turn reducing image processing times. This would perhaps impact the focusing ability of the array, although with the large ray paths associated with narrow gap inspection, imaging is typically performed in the far field and may reduce the impact of increasing pitch.

In addition to potential improvements to the system, performance challenges will require thought when considering an in-process environment. The presence of temperature gradients through a deployed roller probe during in-process imaging will likely require active imaging compensation and probe cooling. This has been addressed in work not included in this thesis [154], but requires additional research in order to improve performance and efficiency of compensation, as well as a suitable method to monitor temperature gradients in the roller probe.

Moreover, the transition from a controlled research environment to an industrial setting will not be without challenges. The effect of broadband noise from surrounding equipment, such as welders and manipulators, could detriment the image quality and produce significant artefacts. A method for reducing this noise within the phased array controller, through insulation or firmware algorithms, may be required.

6.2.2. Imaging Efficiency

The obvious step in for improving the imaging efficiency of the dual-tandem method is the practical deployment of the single-bit coded excitation system. So far, this has been tested with a simple single-array setup due to hardware limitations. Furthermore, single-bit data was not acquired, instead produced in software. The design of a phased array system that utilises the findings of this work to implement single-bit acquisition with low-voltage coded excitation would allow the performance advantages to be fully explored and implemented.

Additionally, the acquisition technique used may be revised. The use of Plane Wave Imaging (PWI) can reduce both the acquisition and image processing time, by limiting the volume of data collected. This has been shown to provide comparative multi-mode imaging quality to TFM with a notable reduction in acquisition and processing times [132], and may aid the development of a real-time implementation of the dual-tandem method.

The encoding method for triggering the capture of ultrasonic data must also be considered when approaching automated deployment. In-process inspection datasets have been captured using robotic manipulators in previous work [176], and therefore data should be collected at regular intervals along a defined scan path. This can be done either through software or hardware communication, the latter perhaps providing the greatest benefit in terms of reduced latency. The position at which each frame is captured would allow the generation of two-dimensional C-scans, or three-dimensional models of the geometry. An example of such a C-scan and 3D model generated in work not presented in this thesis, can be seen below for a narrow-groove weld.

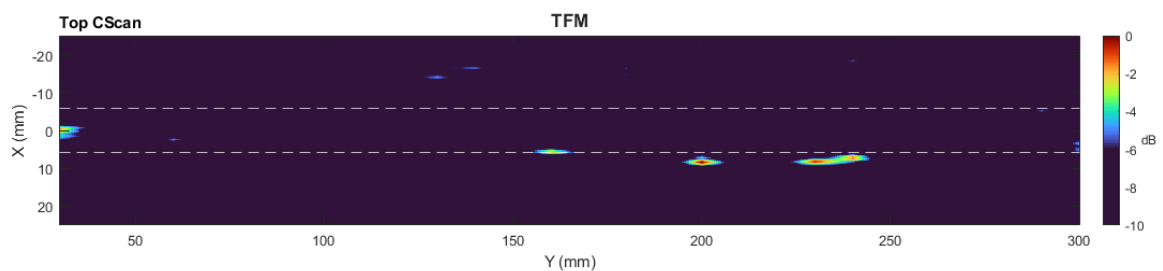


Figure 6.1: Example of a C-Scan of a narrow-groove weld, showing defective areas detected using TFM imaging

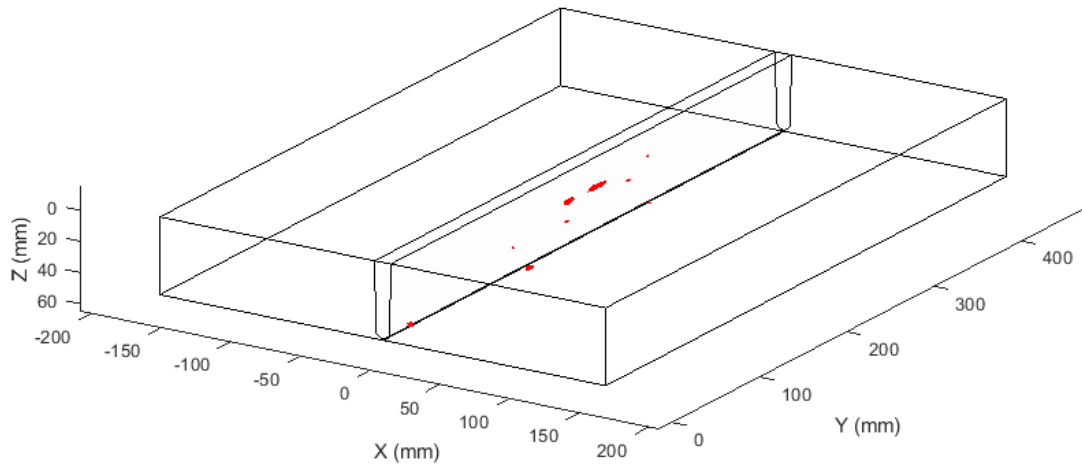


Figure 6.2: Example of a 3D model of a narrow-groove weld, showing defective areas detected using TFM imaging with an amplitude $>-6\text{dB}$

To improve efficiency further, the implementation of Phased Array TOFD (PA-TOFD) inspection with this setup may provide a fast screening method to detect the presence of defects. If possible, this could be used as the main point of defect detection during in-process inspection, and only when an indication exceeds a defined amplitude threshold would the full imaging system be required in order to characterise and size the flaw. FMC or PWI data could still be continuously acquired and streamed such that retrospective analysis could be performed, with data only processed in real time at PA-TOFD indication areas. This would not only reduce the demand for continuous fast imaging, but also reduce the complexity of the process and fall in line with the current inspection methods.

6.2.3. Mechanical Deployment

To prevent damage to the phased array probe in close proximity to the high-temperature weld environment, a dry-coupled high-temperature roller probe should be used [87].

This would introduce added attenuation from the both the tyre and dry-coupling, requiring an increase in receive gains when acquiring ultrasonic data. This could have an impact on SNR, and as such a low-noise phased array acquisition system would be beneficial. Additionally, this could benefit from the use of coded excitation as outlined in Section 5.2 of this thesis, in order to increase dynamic range given that a defect response is distinguishable from the noise floor.

Additionally, the robotic automation of the dual-tandem setup would necessitate accurate synchronisation of two separate robotic manipulators to ensure probes remain parallel and ensure through-transmission imaging remains consistent across the scan. This is the subject of ongoing research, and a number of methods have arisen for close control of tandem robots. An example of the tandem setup, including two separate manipulators equipped with dry-coupled roller probes, is shown in Figure 6.3.



Figure 6.3: Tandem phased array setup on a narrow gap weld using two robotic manipulators with dry-coupled high-temperature roller probes

Furthermore, the use of a dry-coupled roller probe necessitates the consistent application of force to ensure the probe remains sufficiently coupled to the inspected component. This is achieved through force-torque control, in which the vertical position of the manipulator is adjusted to ensure constant force is applied across the scan path. This is crucial in ensuring a consistent and repeatable scanning process, as well ensuring calibration of the probe at a defined force is applicable across the full scan. A further

photo of the tandem roller probes, highlighting these force-torque sensors is shown in Figure 6.4.

An example of images obtained through data collected from the dry-coupled roller probes is shown in Figure 6.5, with a TFM image created using the LL-T mode. The left shows a standard PAUT sector scan image collected using a single array. This is compared with a TFM image created using FMC data collected from dual-array system.

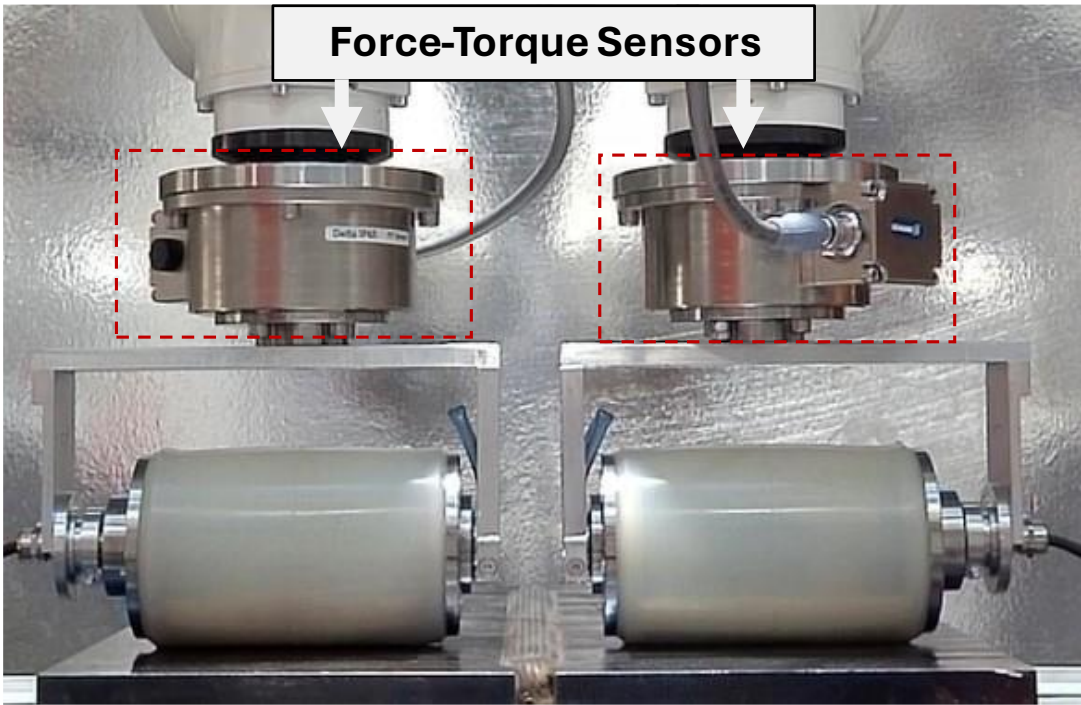


Figure 6.4: Tandem phased array setup on a narrow gap weld showing force-torque sensors used to ensure consistent coupling during scanning

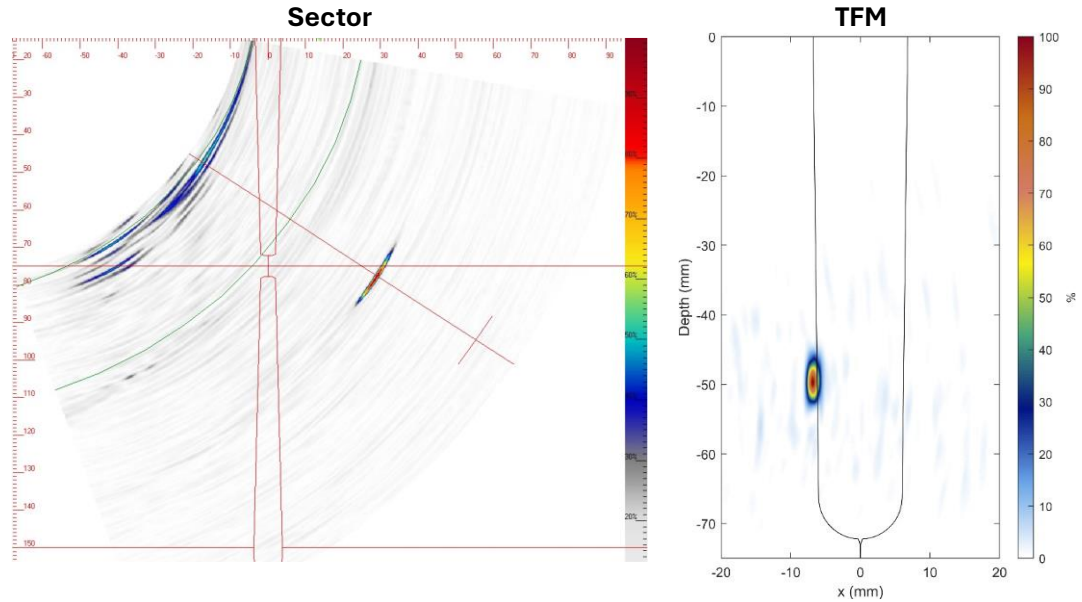


Figure 6.5: Comparison of sector scan image and LL-T TFM image of LOSWF in narrow gap weld using dry-coupled roller probe.

A factor that must be considered when approaching the in-process environment, is the presence of grinding dust, weld spatter and other obstacles which may find their way onto the roller probe path, and reduce coupling efficiency.

6.3. Final Summary

The work demonstrated in fulfilment of this Engineering Doctorate has shown developments in ultrasonic phased array inspection of narrow gap welds. A dual-array inspection system utilising advanced path finding and imaging algorithms has been developed for the detection of mock-LOSWF defects in both fully-filled and partial weld samples. Further research is underway, deploying this inspection system using dry-coupled high-temperature roller probes for in-process weld inspection of narrow gap welds.

Furthermore, a data compression technique utilising pulse compression of ultrasonic Golay transmission waveforms has demonstrated the possibility of a fast, intrinsically safe imaging system with improved data transfer and processing rates. This could enable the real-time inspection of the dual-array system for narrow gap weld inspection, coupled with acquisition techniques such as PWI and with further computational acceleration through GPU processing.

Appendix A

Zoomed in images of those presented in Section 3.5.2.

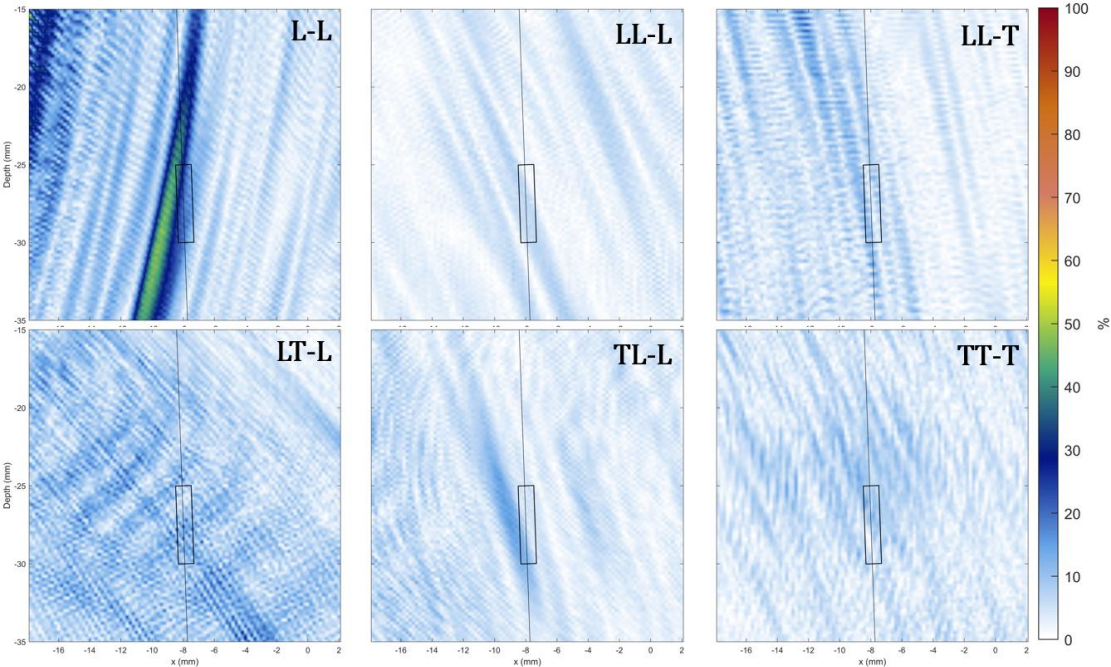


Figure 7.1: Zoomed in TFM images in Section 3.5.2, of sample NG1

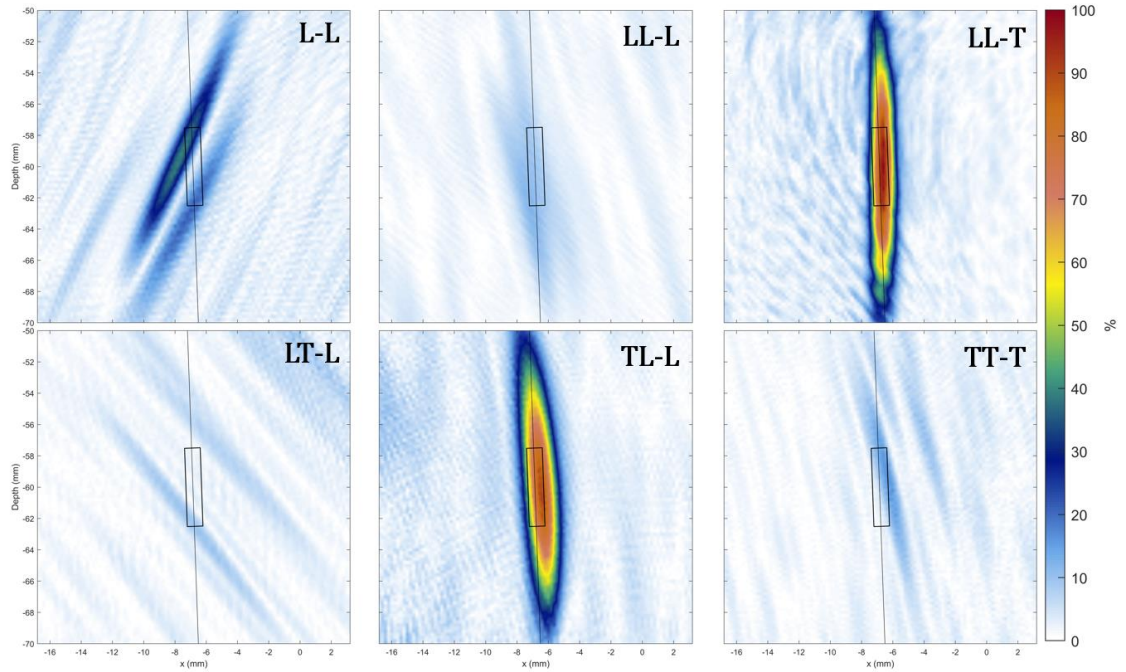


Figure 7.2: Zoomed in TFM images in Section 3.5.2, of sample NG2

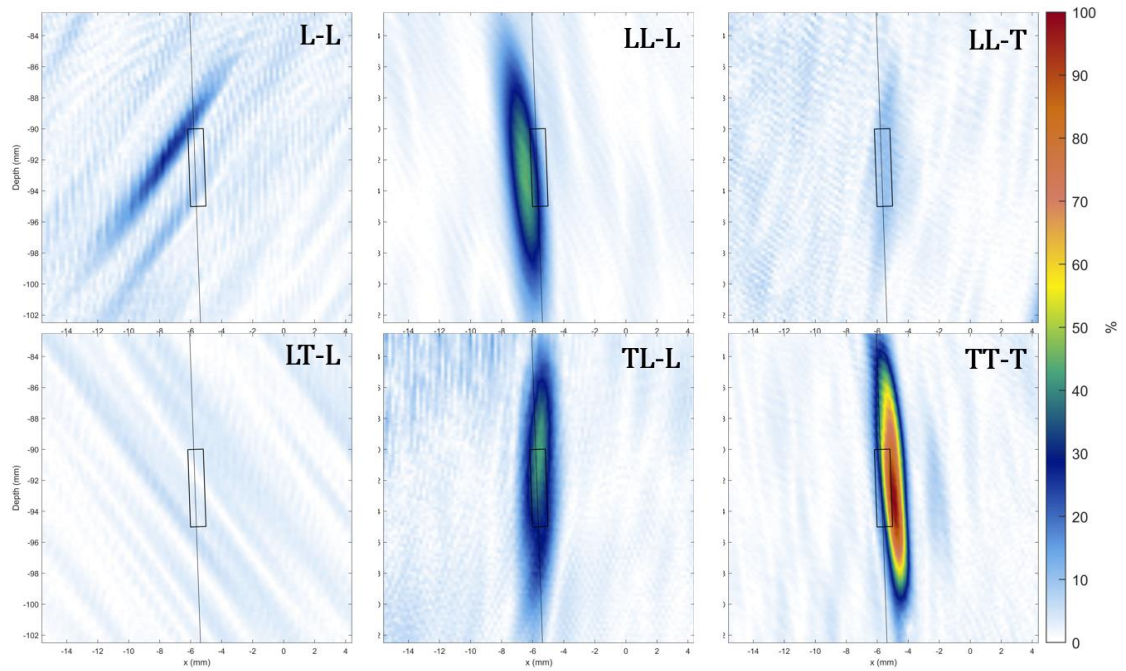


Figure 7.3: Zoomed in TFM images in Section 3.5.2, of sample NG3

Appendix B

Individual views and modes used to generate mixed images in Section 4.5.1.

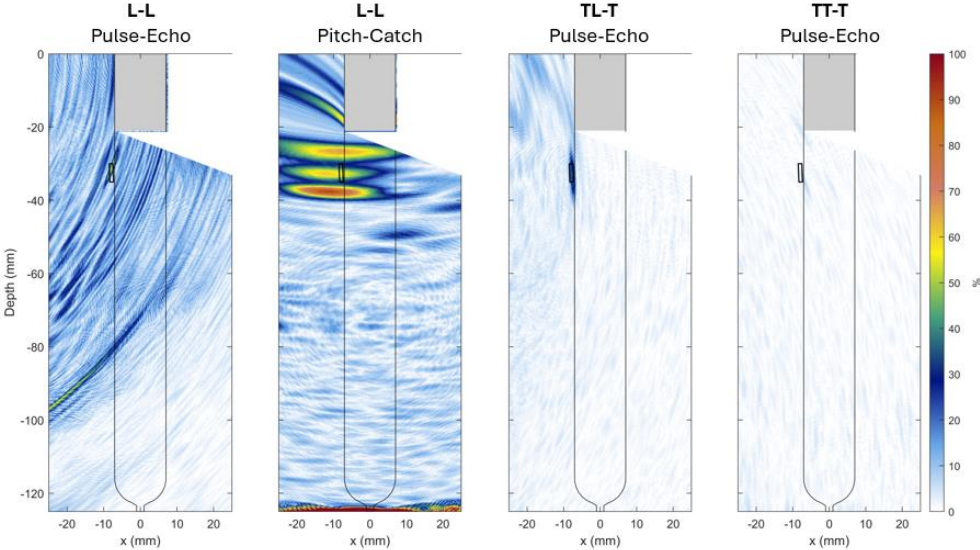


Figure 8.1: TFM images from right array transmission only, used to generate mixed images of sample PNG1 in Section 4.5.1

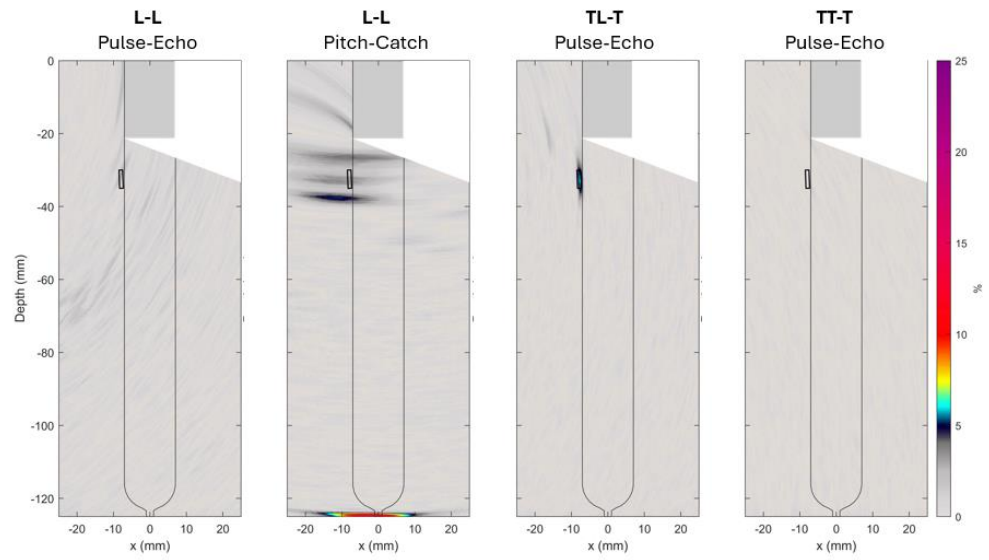


Figure 8.2: PCI images from right array transmission only, used to generate mixed images of sample PNG1 in Section 4.5.1

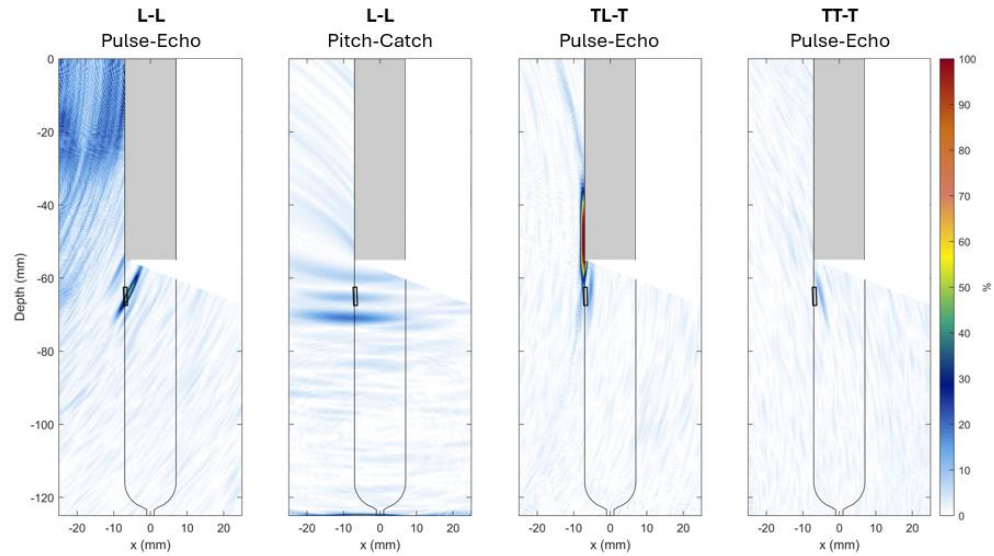


Figure 8.3: TFM images from right array transmission only, used to generate mixed images of sample PNG2 in Section 4.5.1

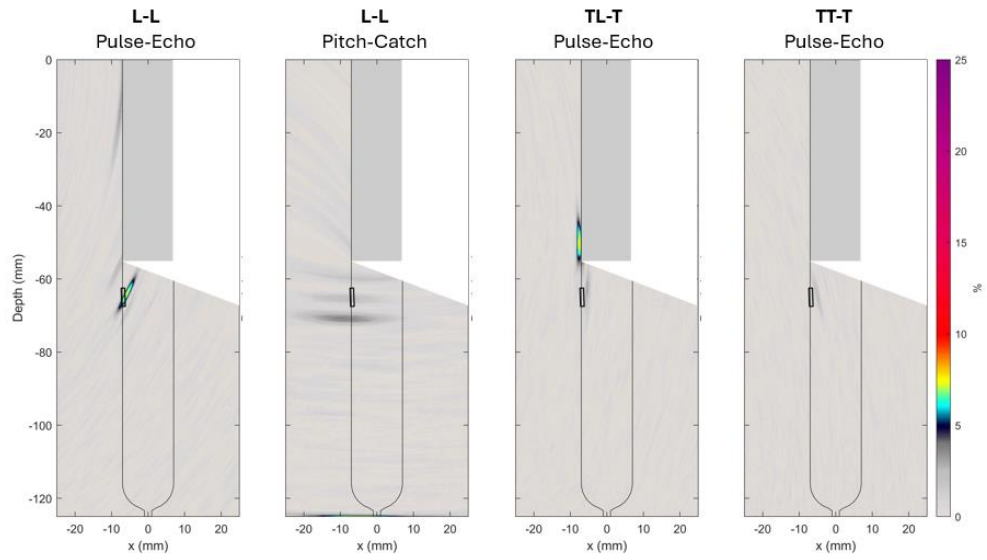


Figure 8.4: PCI images from right array transmission only, used to generate mixed images of sample PNG2 in Section 4.5.1

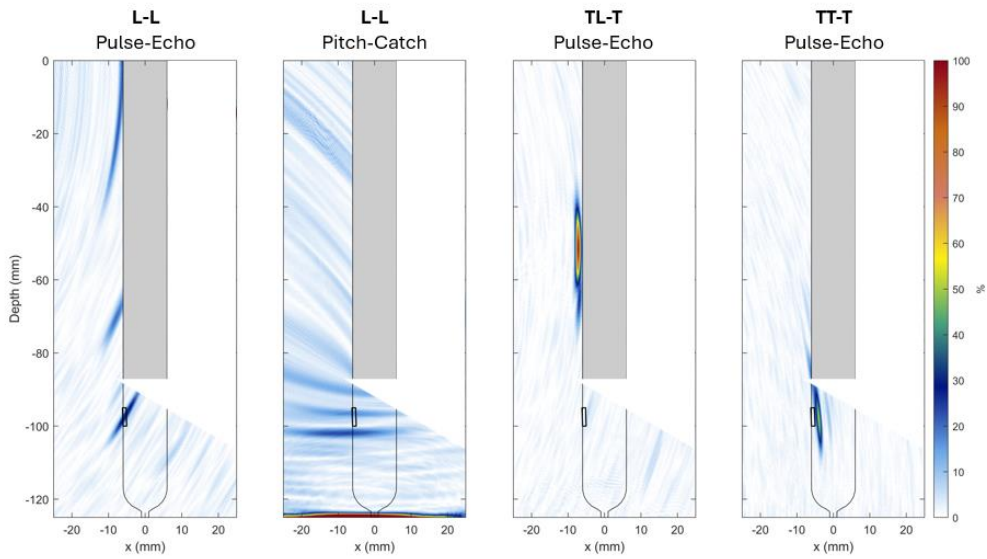


Figure 8.5: TFM images from right array transmission only, used to generate mixed images of sample PNG3 in Section 4.5.1

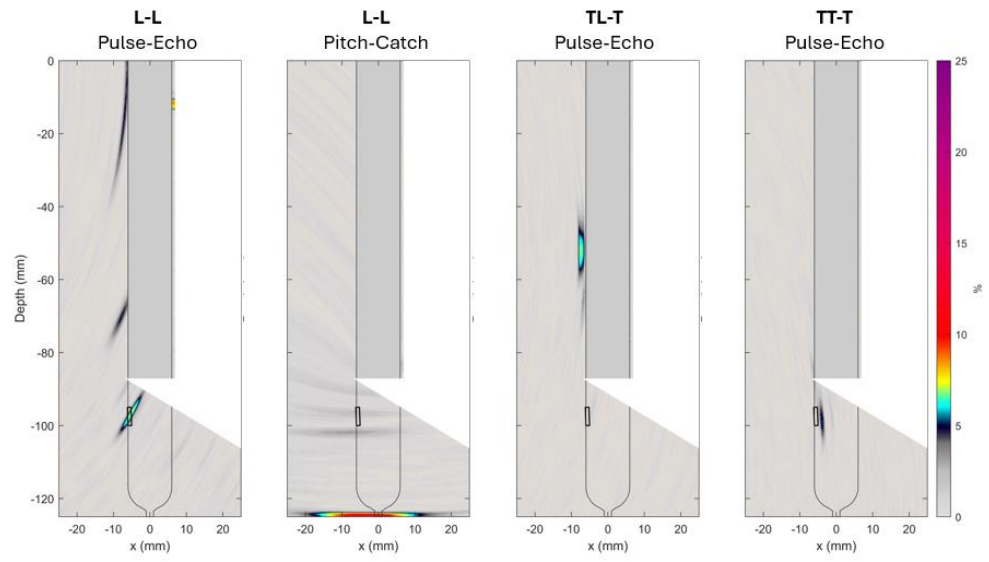


Figure 8.6: PCI images from right array transmission only, used to generate mixed images of sample PNG3 in Section 4.5.1

References

- [1] Department for Energy Security and E. I. S. Net Zero and Department for Business, *Net Zero Strategy: Build Back Greener*. 2022, HM Government.
- [2] Department for Energy Security and Net Zero and E. I. S. Department for Business, *Powering up Britain: The Net Zero Growth Plan*. 2023.
- [3] Department for Energy Security and Net Zero, *Digest of Uk Energy Statistics (Dukes): Electricity*. 2023.
- [4] E. I. S. Department for Business and The Rt Hon Kwasi Kwarteng MP, *Plans Unveiled to Decarbonise Uk Power System by 2035*. 2021.
- [5] Energy Institute, *Statistical Review of World Energy*. 2023.
- [6] C. Matthew and A. Walker, *Nuclear Energy in the Uk*. 2022, UK Parliament POST.
- [7] Department for Energy Security & Net Zero (DESNZ) and E. I. S. Department for Business, *Historical Electricity Data: 1920 to 2022*. 2023.
- [8] Office for nuclear Regulation. *Operational Reactors*. 2024 [cited January 2024]; Available from: <https://www.onr.org.uk/civil-nuclear-reactors/index.htm>.
- [9] Department for Energy Security and Net Zero and E. I. S. Department for Business, *British Energy Security Strategy*. 2022.
- [10] ITV News. *Government Closes 'Historic' Deal to Build First Nuclear Plant in a Generation*. 2013 [cited October 2023]; Available from: <https://www.itv.com/news/2013-10-21/government-closes-historic-deal-to-build-first-nuclear-plant-in-a-generation-hinkley-point>.
- [11] BBC News. *Hinkley Point Nuclear Agreement Reached*. 2015 [cited October 2023]; Available from: <https://www.bbc.co.uk/news/business-34587650>.
- [12] Department for Energy Security and Net Zero, et al., *Six Companies through to Next Stage of Nuclear Technology Competition*. 2023.
- [13] EDF. *Sizewell B Power Station*. 2024 [cited January 2024]; Available from: <https://www.edfenergy.com/energy/power-stations/sizewell-b>.
- [14] The Times. *Hinkley Point C: Why Can't Britain Build New Nuclear Power Stations?* 2024 [cited January 2024]; Available from: <https://www.thetimes.co.uk/article/why-hinkley-point-c-delayed-uk-nuclear-power-station-key-reasons-kvc266mfg>.
- [15] E. a. I. S. C. House of Commons Business, *Decarbonisation of the Power Sector*. 2023.
- [16] Department for Energy Security & Net Zero (DESNZ), et al., *Six Companies through to Next Stage of Nuclear Technology Competition*. 2023.
- [17] Rolls-Royce SMR. *Our Technology*. 2023 [cited January 2024]; Available from: <https://gda.rolls-royce-smr.com/our-technology>.
- [18] C. Bai, et al., *Industry 4.0 Technologies Assessment: A Sustainability Perspective*. International Journal of Production Economics, 2020. **229**: p. 107776.
- [19] McKinsey & Company. *What Are Industry 4.0, the Fourth Industrial Revolution, and 4ir?* 2022 [cited October 2023].

- [20] Zion Market Research, *Welding Robotics Market Size, Share, Trends, Growth and Forecast 2030*. 2023.
- [21] Research and Markets, *Non-Destructive Testing Market Size, Share & Trends Analysis Report by Test Method (Traditional Ndt Method, Digital/Advanced Ndt Method), by Offering, by Vertical, by Region, and Segment Forecasts, 2022-2030*. 2022.
- [22] RCNDE, et al., *A Landscape for the Future of Ndt in the Uk Economy*. 2014.
- [23] The British Standards Limited, *Bs En Iso 19285:2017: Non-Destructive Testing of Welds – Ultrasonic Testing*, in *Phased array ultrasonic testing (PAUT) - Acceptance levels*. 2017.
- [24] The British Standards Limited, *Bs En Iso 17640:2018: Non-Destructive Testing of Welds – Ultrasonic Testing*, in *Techniques, testing levels, and assessment*. 2018.
- [25] J. Schey, A., *Introduction to Manufacturing Processes*. 2nd ed.. ed. 1987, New York: New York : McGraw-Hill.
- [26] T. Lienert, et al., *Welding Fundamentals and Processes*. 2011, ASM International.
- [27] A. M. A. Aditya, et al. *Friction Welding of Similar and Dissimilar Materials: Analysis of Tensile Strength*. in *Proceeding of 5th International Conference on Advances in Manufacturing and Materials Engineering*. 2023. Singapore: Springer Nature Singapore.
- [28] TWI Global. *Rotary Friction Welding*. 2023 [cited October 2023]; Available from: <https://www.twi-global.com/technical-knowledge/job-knowledge/rotary-friction-welding-148>.
- [29] TWI Global. *Linear Friction Welding*. 2023 [cited October 2023]; Available from: <https://www.twi-global.com/technical-knowledge/job-knowledge/linear-friction-welding-146>.
- [30] TWI Global. *What Is Friction Stir Welding (Fsw)? - Process and Applications*. 2023 [cited October 2023]; Available from: <https://www.twi-global.com/technical-knowledge/faqs/faq-what-is-friction-stir-welding>.
- [31] S. Katayama, *Fundamentals and Details of Laser Welding*. 2020: Springer Singapore.
- [32] H. Schultz, *Introduction*, in *Electron Beam Welding*, H. Schultz, Editor. 1993, Woodhead Publishing. p. 1-5.
- [33] B. Nacke and E. Baake, *Induction Heating for Welding*, in *Induction Heating - Heating - Hardening - Annealing - Brazing - Welding*. 2016, Vulkan Verlag.
- [34] N. K. Babu, et al., *Arc Welding*. 2015, London: Springer London: London. p. 593-615.
- [35] R. W. Messler, *Joule Heating*, in *Principles of Welding - Processes, Physics, Chemistry, and Metallurgy*. 2004, John Wiley & Sons.
- [36] TWI Global. *What Is Tungsten Inert Gas (Gtaw or Tig) Welding?* 2023 [cited October 2023]; Available from: <https://www.twi-global.com/technical-knowledge/job-knowledge/tungsten-inert-gas-tig-or-gta-welding-006>.
- [37] S. E. Hughes, *Welding Processes*, in *Quick Guide to Welding and Weld Inspection*. 2009, Woodhead Publishing.

- [38] TWI Global. *Metal Inert Gas (Mig) Welding - Process and Applications*. 2023 [cited October 2023]; Available from: <https://www.twi-global.com/technical-knowledge/job-knowledge/mig-welding-004>.
- [39] Crown Publications. *Mechanised and Automated Tig Welding the Zero Risk, Zero Defects Approach*. 2018 [cited October 2023]; Available from: <https://www.crown.co.za/latest-news/african-fusion-latest-news/7283-mechanised-and-automated-tig-welding-the-zero-risk-zero-defects-approach>.
- [40] J. L. Theodore, et al., *Electric Welding*, 1936, United States Patent Office
- [41] TWI Global. *What Is Submerged-Arc Welding?* 2023 [cited October 2023]; Available from: <https://www.twi-global.com/technical-knowledge/faqs/faq-what-is-submerged-arc-welding>.
- [42] Siim Sild. *Submerged Arc Welding (Saw) Explained*. 2023 [cited October 2023]; Available from: <https://fractory.com/submerged-arc-welding-explained/>.
- [43] TWI Global. *What Is the Heat Affected Zone (Haz)?* 2023 [cited October 2023]; Available from: [https://www.twi-global.com/technical-knowledge/faqs/what-is-the-heat-affected-zone#:~:text=The%20heat%20affected%20zone%20\(HAZ\)%20is%20a%20non%2Dmelted,welding%20or%20high%2Dheat%20cutting](https://www.twi-global.com/technical-knowledge/faqs/what-is-the-heat-affected-zone#:~:text=The%20heat%20affected%20zone%20(HAZ)%20is%20a%20non%2Dmelted,welding%20or%20high%2Dheat%20cutting).
- [44] R. Singh, *Stresses, Shrinkage, and Distortion in Weldments*, in *Applied Welding Engineering (Third Edition)*, R. Singh, Editor. 2020, Butterworth-Heinemann. p. 207-249.
- [45] J. C. Lippold, *Hydrogen-Induced Cracking*. Welding metallurgy and weldability, 2014. **306**.
- [46] S. E. Hughes, *Lack of Fusion*, in *Quick Guide to Welding and Weld Inspection*. 2009, Woodhead Publishing.
- [47] S. E. Hughes, *Porosity*, in *Quick Guide to Welding and Weld Inspection*. 2009, Woodhead Publishing.
- [48] TWI Global. *What Is Narrow Gap Welding?* 2023 [cited October 2023]; Available from: <https://www.twi-global.com/technical-knowledge/faqs/faq-what-is-narrow-gap-welding>.
- [49] T. Manzoli and E. Caccia, *Narrow Gap Welding of Heavy Gauge Steel Nuclear Components*. Welding International, 1989. **3**(5): p. 417-423.
- [50] P. Kah, *Chapter 7 - Narrow Gap Welding of Thick Sections*, in *Advancements in Intelligent Gas Metal Arc Welding Systems*, P. Kah, Editor. 2021, Elsevier. p. 327-340.
- [51] X. Zhang, et al. *Properties of Welded Joint for Narrow Gap Laser Welding of Austenitic Stainless Steels*. 2010. Laser Institute of America.
- [52] X. Zhang, et al., *Welding of Thick Stainless Steel Plates up to 50 Mm with High Brightness Lasers*. Journal of Laser Applications, 2011. **23**(2).
- [53] R. N. Gunn, *Welding Processes*, in *Duplex Stainless Steels*. 1997, Woodhead Publishing. p. 133-145.
- [54] TWI Global. *How Can Electron Beam Welding Be Used for Fabrication of Thick Sections?* . 2023 [cited November 2023]; Available from: <https://www.twi-global.com/technical-knowledge/faqs/faq-how-can-electron-beam-welding-be-used-for-fabrication-of-thick->

[sections#:~:text=Typical%20welding%20parameters%20for%2070mm,section%20fabrications%20quickly%20and%20economically.](#)

- [55] Arc Machines Inc. *The Narrow Gap Welding Process: Advantages of Choosing Narrow Groove Welding*. 2023 [cited October 2023]; Available from: <https://resources.arcmachines.com/the-narrow-gap-welding-process-advantages-of-choosing-narrow-groove-welding-slp/>.
- [56] H. Hänninen, et al., *Structural Integrity of Ni-Base Alloy Welds*. 2014: VTT Espoo, Finland.
- [57] J. F. Hunt, *Narrow Gap Welding of Pressure Vessels – a Manufacturer's View*, in *Welding for Challenging Environments*, C. Welding Institute of, Editor. 1986, Pergamon. p. 107-116.
- [58] N. Sekimura and N. Yamashita, *20 - Plant Life Management (Plim) Practices for Boiling Water Nuclear Reactors (Bwr): Japanese Experience*, in *Understanding and Mitigating Ageing in Nuclear Power Plants*, P.G. Tipping, Editor. 2010, Woodhead Publishing. p. 706-731.
- [59] L. Wan, et al., *Narrow-Gap Tungsten Inert Gas Welding of 78-Mm-Thick Ti-6al-4v Alloy*. *Materials Science and Technology*, 2016. **32**(15): p. 1545-1552.
- [60] H. Ming, et al., *Microstructure of a Safe-End Dissimilar Metal Weld Joint (Sa508-52-316l) Prepared by Narrow-Gap Gtaw*. *Materials Characterization*, 2017. **123**: p. 233-243.
- [61] A. Mitra, et al., *Design and Development of Thick Plate Concept for Rotatable Plugs and Technology Development for Future Indian Fbr*. *Nuclear Engineering and Design*, 2012. **246**: p. 245-255.
- [62] Polysoude. *Narrow Gap Welding*. 2023 [cited October 2023]; Available from: <https://www.polysoude.com/narrow-gap-welding/>.
- [63] K. Sotoodeh, *Dissimilar Welding between Piping and Valves in the Offshore Oil and Gas Industry*. *Welding International*, 2021. **35**(1-3): p. 34-44.
- [64] T. Yin, et al., *Research on Filling Strategy of Pipeline Multi-Layer Welding for Compound Narrow Gap Groove*. *Materials*, 2022. **15**(17): p. 5967.
- [65] Y. Bao, et al., *The Influence of Oscillation Parameters on the Formation of Overhead Welding Seams in the Narrow-Gap Gmaw Process*. *Applied Sciences*, 2023. **13**(9): p. 5519.
- [66] J. D. N. Cheeke, *Fundamentals and Applications of Ultrasonic Waves*. 2016: CRC Press.
- [67] R. A. Kastelein, et al., *Audiogram of a Harbor Porpoise (Phocoena Phocoena) Measured with Narrow-Band Frequency-Modulated Signals*. *The Journal of the Acoustical Society of America*, 2002. **112**(1): p. 334-344.
- [68] D. A. Mann, et al., *Ultrasound Detection by Clupeiform Fishes*. *The Journal of the Acoustical Society of America*, 2001. **109**(6): p. 3048-3054.
- [69] L. A. Miller and A. Surlykke, *How Some Insects Detect and Avoid Being Eaten by Bats: Tactics and Countertactics of Prey and Predator: Evolutionarily Speaking, Insects Have Responded to Selective Pressure from Bats with New Evasive Mechanisms, and These Very Responses in Turn Put Pressure on Bats to "Improve" Their Tactics*. *BioScience*, 2001. **51**(7): p. 570-581.

- [70] P.-K. Choi, *Ultrasound Propagation*, in *Ultrasonics*. 2022, IOP Publishing. p. 1-1-1-33.
- [71] L. Rayleigh, *On Waves Propagated Along the Plane Surface of an Elastic Solid*. Proceedings of the London Mathematical Society, 1885. **s1-17**(1): p. 4-11.
- [72] H. Lamb, *On the Vibrations of an Elastic Sphere*. Proceedings of the London Mathematical Society, 1881. **s1-13**(1): p. 189-212.
- [73] S. V. Kuznetsov, *Love Waves in Nondestructive Diagnostics of Layered Composites. Survey*. Acoustical Physics, 2010. **56**(6): p. 877-892.
- [74] R. Halmslaw, *Non-Destructive Testing*. 1987: The British Institute of Non-Destructive Testing.
- [75] Engineering Toolbox. *Water - Speed of Sound Vs. Temperature*. 2004 [cited October 2023]; Available from: https://www.engineeringtoolbox.com/sound-speed-water-d_598.html.
- [76] Engineering Toolbox. *Solids and Metals - Speed of Sound*. 2004 [cited October 2023]; Available from: https://www.engineeringtoolbox.com/sound-speed-solids-d_713.html.
- [77] P. T. Bobrowsky and B. Marker, *Encyclopedia of Engineering Geology*. 2018: Springer Cham.
- [78] D. B. Sirdeshmukh, et al., *Mechanical Properties of Solids*. 2011, Springer Berlin Heidelberg. p. 261-289.
- [79] D. Ganguly, et al., *Medical Imaging: A Review*. 2010, Springer Berlin Heidelberg. p. 504-516.
- [80] E. A. Foster, et al., *Automated Real-Time Eddy Current Array Inspection of Nuclear Assets*. *Sensors*, 2022. **22**(16): p. 6036.
- [81] A. Zolfaghari and F. Kolahan, *Reliability and Sensitivity of Visible Liquid Penetrant Ndt for Inspection of Welded Components*. *Materials Testing*, 2017. **59**(3): p. 290-294.
- [82] V. P. Vavilov and D. D. Burleigh, *Review of Pulsed Thermal Ndt: Physical Principles, Theory and Data Processing*. *NDT & E International*, 2015. **73**: p. 28-52.
- [83] R. Hanke, et al., *X-Ray Based Methods for Non-Destructive Testing and Material Characterization*. Nuclear Instruments and Methods in Physics Research Section A: Accelerators, Spectrometers, Detectors and Associated Equipment, 2008. **591**(1): p. 14-18.
- [84] M. R. Torloni, et al., *Safety of Ultrasonography in Pregnancy: Who Systematic Review of the Literature and Meta - Analysis*. *Ultrasound in Obstetrics & Gynecology*, 2009. **33**(5): p. 599-608.
- [85] Y. Javadi, et al., *In-Process Calibration of a Non-Destructive Testing System Used for in-Process Inspection of Multi-Pass Welding*. *Materials & Design*, 2020. **195**: p. 108981.
- [86] Y. Javadi, et al., *High-Temperature in-Process Inspection Followed by 96-H Robotic Inspection of Intentionally Manufactured Hydrogen Crack in Multi-Pass Robotic Welding*. *International Journal of Pressure Vessels and Piping*, 2021. **189**: p. 104288.

- [87] R. K. W. Vithanage, et al., *A Phased Array Ultrasound Roller Probe for Automated in-Process/Interpass Inspection of Multipass Welds*. IEEE Transactions on Industrial Electronics, 2021. **68**(12): p. 12781-12790.
- [88] R. Zimmermann, et al., *Multi-Layer Ultrasonic Imaging of as-Built Wire + Arc Additive Manufactured Components*. Additive Manufacturing, 2021. **48**: p. 102398.
- [89] R. K. W. Vithanage, et al., *Development of a Phased Array Ultrasound Roller Probe for Inspection of Wire + Arc Additive Manufactured Components*. Journal of Manufacturing Processes, 2022. **80**: p. 765-774.
- [90] Y. Javadi, et al., *Ultrasonic Phased Array Inspection of Wire + Arc Additive Manufacture Samples Using Conventional and Total Focusing Method Imaging Approaches*. Insight - Non-Destructive Testing and Condition Monitoring, 2019. **61**(3): p. 144-148.
- [91] D. Ensminger and L. J. Bond, *Ultrasonics: Fundamentals, Technologies and Applications*. Vol. 3. 2011: CRC Press.
- [92] H. E. Van Valkenburg, *Standardization of Ultrasonic Ndt from an Astm Perspective: Past, Present, and Future*, in *Nondestructive Testing Standards: Present and Future*. 1992, ASTM International. p. 49-55.
- [93] F. A. Firestone, *Flaw Detecting Device and Measuring Instrument*, 1942, United States Patent Office no 2280226
- [94] F. A. Firestone, *The Supersonic Reflectoscope, an Instrument for Inspecting the Interior of Parts by Means of Sound Waves*. Journal of the Acoustical Society of America,, 1945. **17**(3): p. 287-299.
- [95] W. S. Erwin, *Supersonic Measuring Means*, 1947, United States Patent Office no 2431233
- [96] F. A. Firestone, *Method of Supersonic Inspection*, 1952, United States Patent Office no 2592134
- [97] J. C. Somer, *Electronic Sector Scanning for Ultrasonic Diagnosis*. Ultrasonics, 1968. **6**(3): p. 153-159.
- [98] G. Bradfield, *Improvements in Ultrasonic Flaw Detection*. Journal of the British Institution of Radio Engineers, 1954. **14**(7): p. 303-308.
- [99] W. Gebhardt, *Improvement of Ultrasonic Testing by Phased Arrays*. Nuclear Engineering and Design, 1983. **76**(3): p. 275-283.
- [100] B. W. Drinkwater and P. D. Wilcox, *Ultrasonic Arrays for Non-Destructive Evaluation: A Review*. NDT & E International, 2006. **39**(7): p. 525-541.
- [101] S. McKnight, et al., *A Comparison of Methods for Generating Synthetic Training Data for Domain Adaption of Deep Learning Models in Ultrasonic Non-Destructive Evaluation*. NDT & E International, 2023: p. 102978.
- [102] C. Mineo, et al. *Fast Ultrasonic Phased Array Inspection of Complex Geometries Delivered through Robotic Manipulators and High Speed Data Acquisition Instrumentation*. in *2016 IEEE International Ultrasonics Symposium (IUS)*. 2016.
- [103] T. Stratoudaki, et al., *Laser Induced Ultrasonic Phased Array Using Full Matrix Capture Data Acquisition and Total Focusing Method*. Optics Express, 2016. **24**(19): p. 21921.

- [104] D. Pieris, et al., *Laser Induced Phased Arrays (Lipa) to Detect Nested Features in Additively Manufactured Components*. *Materials & Design*, 2020. **187**: p. 108412.
- [105] J. Singh, et al., *Deep Learning Based Inversion of Locally Anisotropic Weld Properties from Ultrasonic Array Data*. *Applied Sciences*, 2022. **12**(2): p. 532.
- [106] J. Curie and P. Curie, *Development, Via Compression, of Electric Polarization in Hemihedral Crystals with Inclined Faces*. *Bulletin de la Société Minéralogique de France*, 1880. **3**(4).
- [107] S. Cochran, *Piezoelectricity and Basic Configurations for Piezoelectric Ultrasonic Transducers*, in *Ultrasonic Transducers*, K. Nakamura, Editor. 2012, Woodhead Publishing. p. 3-35.
- [108] H. Wei, et al., *An Overview of Lead-Free Piezoelectric Materials and Devices*. *Journal of Materials Chemistry C*, 2018. **6**(46): p. 12446-12467.
- [109] R. Singh, *Ultrasonic Testing*, in *Applied Welding Engineering - Processes, Codes and Standards*. 2012, Elsevier.
- [110] M. G. Silk and B. H. Lidington, *The Potential of Scattered or Diffracted Ultrasound in the Determination of Crack Depth*. *Non-Destructive Testing*, 1975. **8**(3): p. 146-151.
- [111] The British Standards Limited, *Bs En Iso 10863:2020: Non-Destructive Testing — Ultrasonic Testing*, in *Use of time-of-flight diffraction technique (TOFD)*. 2020.
- [112] IPEC. *Time of Flight Diffraction (Tofd)*. 2023 [cited October 2023]; Available from: <https://www.ipec.ie/time-of-flight-diffraction/>.
- [113] S.-J. Jin, et al., *Corrected Mode-Converted Wave Method for Detecting Defects in Tofd Dead Zone*. *Journal of Nondestructive Evaluation*, 2023. **42**(3).
- [114] S. J. Jin, et al., *Quantitative Detection of Shallow Subsurface Defects by Using Mode-Converted Waves in Time-of-Flight Diffraction Technique*. *Journal of Nondestructive Evaluation*, 2020. **39**(2).
- [115] IMASONIC. *Design Notes for Phased Array*. [cited October 2023]; Available from: <https://www.imasonic.com/industry/design-notes-for-phased-array/>.
- [116] Evident. *Grating Lobes and Side Lobes*. *Phased Array Tutorial* [cited October 2023]; Available from: <https://www.olympus-ims.com/en/ndt-tutorials/transducers/lobes/>.
- [117] J. R. Frederick, et al., *Improved Ultrasonic Nondestructive Testing of Pressure Vessels Annual Progress Report, August 1, 1975--July 31, 1976*. 1977: United States. p. v.
- [118] ASTM, *Astm E2491-06: Standard Guide for Evaluating Performance Characteristics of Phased-Array Ultrasonic Examination Instruments and Systems*. 2010.
- [119] C. Brillouin, et al., *Tofd Inspection with Phased Arrays*, in *17th World Conference on Nondestructive Testing*. 2008: Shanghai.
- [120] S. Zhang, et al., *Study of Pa-Tofd Inspection Based on Numerical Simulation*, in *19th World Conference on Non-Destructive Testing (WCNDT 2016)*. 2016: Munich.

- [121] D. Lines. *The Application of Real-Time Medical Ultrasound Imaging to Ndt.* in *British Institute of NDT Symposium on Ultrasonic Imaging, Visualisation and Display*. 1982. Northampton.
- [122] C. Holmes, et al., *Post-Processing of the Full Matrix of Ultrasonic Transmit–Receive Array Data for Non-Destructive Evaluation*. *NDT & E International*, 2005. **38**(8): p. 701-711.
- [123] J. Zhang, et al., *Comparison of Ultrasonic Array Imaging Algorithms for Nondestructive Evaluation*. *IEEE Transactions on Ultrasonics, Ferroelectrics, and Frequency Control*, 2013. **60**(8): p. 1732-1745.
- [124] C. Fan, et al., *A Comparison between Ultrasonic Array Beamforming and Super Resolution Imaging Algorithms for Non-Destructive Evaluation*. *Ultrasonics*, 2014. **54**(7): p. 1842-1850.
- [125] V. Cizek, *Discrete Hilbert Transform*. *IEEE Transactions on Audio and Electroacoustics*, 1970. **18**(4): p. 340-343.
- [126] L. Marple, *Computing the Discrete-Time "Analytic" Signal Via Fft*. *IEEE Transactions on Signal Processing*, 1999. **47**(9): p. 2600-2603.
- [127] A. J. Hunter, et al., *The Wavenumber Algorithm for Full-Matrix Imaging Using an Ultrasonic Array*. *IEEE Transactions on Ultrasonics, Ferroelectrics and Frequency Control*, 2008. **55**(11): p. 2450-2462.
- [128] E. L. Villaverde, et al. *High-Frequency Total Focusing Method (Tfm) Imaging in Strongly Attenuating Materials with the Decomposition of the Time Reversal Operator Associated with Orthogonal Coded Excitations*. 2017. Author(s).
- [129] M. Sutcliffe, et al., *Multiple Virtual Source Aperture Imaging for Non-Destructive Testing*. *Insight - Non-Destructive Testing and Condition Monitoring*, 2014. **56**(2): p. 75-81.
- [130] C. Holmes, et al., *The Post-Processing of Ultrasonic Array Data Using the Total Focusing Method*. *Insight - Non-Destructive Testing and Condition Monitoring*, 2004. **46**(11): p. 677-680.
- [131] J. Zhang, et al., *Defect Detection Using Ultrasonic Arrays: The Multi-Mode Total Focusing Method*. *NDT & E International*, 2010. **43**(2): p. 123-133.
- [132] L. Le Jeune, et al., *Plane Wave Imaging for Ultrasonic Non-Destructive Testing: Generalization to Multimodal Imaging*. *Ultrasonics*, 2016. **64**: p. 128-138.
- [133] K. Sy, et al., *Development of Methods for the Analysis of Multi-Mode Tfm Images*. *Journal of Physics: Conference Series*, 2018. **1017**(1): p. 012005.
- [134] P. D. Wilcox, et al., *Advanced Reflector Characterization with Ultrasonic Phased Arrays in Nde Applications*. *IEEE Transactions on Ultrasonics, Ferroelectrics, and Frequency Control*, 2007. **54**(8): p. 1541-1550.
- [135] Evident, *Omniscan™ X3 64 Phased Array and Tfm Flaw Detector*. 2023.
- [136] Sonatest, *Veo3*. 2022.
- [137] Zetec, *Topaz64 Fully Integrated, Portable Phased Array Ut & Tfm Device*. 2023.
- [138] The British Standards Limited, *Bs Iso 23865:2021: Non-Destructive Testing — Ultrasonic Testing, in General use of full matrix capture/total focusing technique (FMC/TFM) and related technologies*. 2021.

- [139] J. Camacho, et al., *Ultrasonic Crack Evaluation by Phase Coherence Processing and Tfm and Its Application to Online Monitoring in Fatigue Tests*. NDT & E International, 2018. **93**: p. 164-174.
- [140] B. Gauthier, et al., *Towards an Alternative to Time of Flight Diffraction Using Instantaneous Phase Coherence Imaging for Characterization of Crack-Like Defects*. Sensors, 2021. **21**(3): p. 730.
- [141] J. Camacho, et al., *Phase Coherence Imaging*. IEEE Transactions on Ultrasonics, Ferroelectrics and Frequency Control, 2009. **56**(5): p. 958-974.
- [142] J. F. Cruza, et al., *Plane-Wave Phase-Coherence Imaging for Nde*. NDT & E International, 2017. **87**: p. 31-37.
- [143] B. Gauthier, et al., *Lightweight and Amplitude-Free Ultrasonic Imaging Using Single-Bit Digitization and Instantaneous Phase Coherence*. IEEE Transactions on Ultrasonics, Ferroelectrics, and Frequency Control, 2022. **69**(5): p. 1763-1774.
- [144] C.-H. Kwan, et al., *Tfm Acoustic Influence Map*, in *ASNT Research Symposium 2019*. 2019: Los Angeles.
- [145] M. Parrilla, et al. *Dynamic Focusing through Arbitrary Geometry Interfaces*. in *2008 IEEE Ultrasonics Symposium*. 2008.
- [146] C. Mineo, et al., *Solving Ultrasonic Ray Tracing in Parts with Multiple Material Layers through Root-Finding Methods*. Ultrasonics, 2022. **124**: p. 106747.
- [147] C. Mineo, et al., *Generalised Bisection Method for Optimum Ultrasonic Ray Tracing and Focusing in Multi-Layered Structures*. Ultrasonics, 2021. **111**: p. 106330.
- [148] O. Nowers, et al., *Ultrasonic Array Imaging through an Anisotropic Austenitic Steel Weld Using an Efficient Ray-Tracing Algorithm*. NDT & E International, 2016. **79**: p. 98-108.
- [149] O. Nowers, et al., *Novel Ray-Tracing Algorithms in Nde: Application of Dijkstra and a* Algorithms to the Inspection of an Anisotropic Weld*. NDT & E International, 2014. **61**: p. 58-66.
- [150] M. S. Hassouna and A. A. Farag, *Multistencils Fast Marching Methods: A Highly Accurate Solution to the Eikonal Equation on Cartesian Domains*. IEEE Transactions on Pattern Analysis and Machine Intelligence, 2007. **29**(9): p. 1563-1574.
- [151] J. A. Sethian, *Fast Marching Methods*. SIAM Review, 1999. **41**(2): p. 199-235.
- [152] A. M. Popovici and J. A. Sethian, *3 - D Imaging Using Higher Order Fast Marching Traveltimes*. Geophysics, 2002. **67**(2): p. 604-609.
- [153] K. M. M. Tant, et al., *A Transdimensional Bayesian Approach to Ultrasonic Travel-Time Tomography for Non-Destructive Testing*. Inverse Problems, 2018. **34**(9): p. 095002.
- [154] E. A. Foster, et al., *Thermal Compensation of Ultrasonic Transmit and Receive Data for Steel Welded Plates at the Point of Manufacture*. NDT & E International, 2023. **137**: p. 102812.
- [155] E. Nicolson, et al., *Dual-Tandem Phased Array Method for Imaging of near-Vertical Defects in Narrow-Gap Welds*. NDT & E International, 2023. **135**: p. 102808.

- [156] K. M. M. Tant, et al., *Effective Grain Orientation Mapping of Complex and Locally Anisotropic Media for Improved Imaging in Ultrasonic Non-Destructive Testing*. Inverse Problems in Science and Engineering, 2020. **28**(12): p. 1694-1718.
- [157] J. Ludlam, et al., *Travel Times and Ray Paths for Acoustic and Elastic Waves in Generally Anisotropic Media*. Journal of Computational Physics, 2023.
- [158] E. Mohseni, et al. *Eddy Currents and Ultrasonic Testing Data Fusion for Wire + Arc Additive Manufacturing*. in *60th Annual British Conference on NDT*. 2023. Northampton.
- [159] E. Mohseni, et al. *Data Fusion for Multi-Modal in-Process Non-Destructive Evaluation of Wire + Arc Additive Manufacturing*. in *IEEE International Ultrasonics Symposium 2023*. 2023. Montréal.
- [160] P. D. Wilcox, et al., *Fusion of Multi-View Ultrasonic Data for Increased Detection Performance in Non-Destructive Evaluation*. Proceedings of the Royal Society A: Mathematical, Physical and Engineering Sciences, 2020. **476**(2243): p. 20200086.
- [161] R. L. T. Bevan, et al., *Data Fusion of Multiview Ultrasonic Imaging for Characterization of Large Defects*. IEEE Transactions on Ultrasonics, Ferroelectrics, and Frequency Control, 2020. **67**(11): p. 2387-2401.
- [162] R. L. T. Bevan and A. J. Croxford, *Automated Detection and Characterisation of Defects from Multiview Ultrasonic Imaging*. NDT & E International, 2022. **128**: p. 102628.
- [163] The British Standards Limited, *Bs En Iso 18563-1:2017: Non-Destructive Testing of Welds – Characterization and Verification of Ultrasonic Phased Array Equipment*, in *Instruments*. 2015.
- [164] The British Standards Limited, *Bs En Iso 18563-2:2017: Non-Destructive Testing of Welds – Characterization and Verification of Ultrasonic Phased Array Equipment*, in *Probes*. 2017.
- [165] N. Badeau, et al., *Total Focusing Method Amplitude Fidelity Estimation Using an Analytical Model*, in *ASNT Research Symposium*. 2020: Williamsburg.
- [166] The British Standards Limited, *Bs En Iso 13588:2019: Non-Destructive Testing of Welds – Ultrasonic Testing*, in *Use of automated phased array technology*. 2019.
- [167] A. E. Bazulin, et al., *Reconstructing the Image of Reflectors at Base-Metal–Weld Interface Using Ultrasonic Antenna Arrays*. Russian Journal of Nondestructive Testing, 2021. **57**(9): p. 739-752.
- [168] E. Mohseni, et al., *Model-Assisted Ultrasonic Calibration Using Intentionally Embedded Defects for in-Process Weld Inspection*. Materials & Design, 2021. **198**: p. 109330.
- [169] Evident. *Material Sound Velocities*. 2023 [cited November 2022]; Available from: <https://www.olympus-ims.com/en/ndt-tutorials/thickness-gauge/appendices-velocities/>.
- [170] National Instruments, *Labview VI7 (64-Bit)*. 2017.
- [171] Paul Wilcox. *Mfmc Format*. 2019; 2:[Available from: <https://github.com/ndtatbristol/mfmc>].

- [172] MathWorks, *Matlab*. 2022.
- [173] MathWorks, *Parrallel Computing Toolbox*. 2022.
- [174] MathWorks, *Gpu Coder*. 2022.
- [175] M. V. Felice and Z. Fan, *Sizing of Flaws Using Ultrasonic Bulk Wave Testing: A Review*. Ultrasonics, 2018. **88**: p. 26-42.
- [176] M. Vasilev, et al., *Sensor-Enabled Multi-Robot System for Automated Welding and in-Process Ultrasonic Nde*. Sensors, 2021. **21**(15): p. 5077.
- [177] N. E. Sweeney, et al., *In-Process Phased Array Ultrasonic Weld Pool Monitoring*. NDT & E International, 2023. **137**: p. 102850.
- [178] G. Montaldo, et al., *Coherent Plane-Wave Compounding for Very High Frame Rate Ultrasonography and Transient Elastography*. IEEE Transactions on Ultrasonics, Ferroelectrics, and Frequency Control, 2009. **56**(3): p. 489-506.
- [179] Y. Javadi, et al., *Continuous Monitoring of an Intentionally-Manufactured Crack Using an Automated Welding and in-Process Inspection System*. Materials & Design, 2020. **191**: p. 108655.
- [180] D. G. Aggelis and A. S. Paipetis, *Monitoring of Resin Curing and Hardening by Ultrasound*. Construction and Building Materials, 2012. **26**(1): p. 755-760.
- [181] C. Holmes, et al., *Advanced Post-Processing for Scanned Ultrasonic Arrays: Application to Defect Detection and Classification in Non-Destructive Evaluation*. Ultrasonics, 2008. **48**(6-7): p. 636-642.
- [182] D. Lines, *Rapid Distributed Data Collection with Arrays - the Next Step Beyond Full Waveform Capture*. Insight, 2006. **48**.
- [183] M. Fornasier and H. Rauhut, *Compressive Sensing*. 2011, Springer New York. p. 187-228.
- [184] Z. Bai, et al., *Compressive Sensing of Phased Array Ultrasonic Signal in Defect Detection: Simulation Study and Experimental Verification*. Structural Health Monitoring, 2018. **17**(3): p. 434-449.
- [185] P. Yang, et al., *A Novel Method to Design Sparse Linear Arrays for Ultrasonic Phased Array*. Ultrasonics, 2006. **44**: p. e717-e721.
- [186] L. Moreau, et al., *Ultrasonic Imaging Algorithms with Limited Transmission Cycles for Rapid Nondestructive Evaluation*. IEEE Transactions on Ultrasonics, Ferroelectrics, and Frequency Control, 2009. **56**(9): p. 1932-1944.
- [187] A. Austeng and S. Holm, *Sparse 2-D Arrays for 3-D Phased Array Imaging - Design Methods*. IEEE Transactions on Ultrasonics, Ferroelectrics, and Frequency Control, 2002. **49**(8): p. 1073-1086.
- [188] Y. Lu, et al., *A Successive Parameter Estimation Algorithm for Chirplet Signal Decomposition*. IEEE Transactions on Ultrasonics, Ferroelectrics and Frequency Control, 2006. **53**(11): p. 2121-2131.
- [189] Y. Nabil, et al. *Ultrasonic Signals Parameters Estimation Based on Differential Evolution*. in *3rd International Conference on Control Engineering & Information Technology (CEIT)*. 2015. IEEE.
- [190] G. Cardoso and J. Saniie. *Performance Evaluation of Dwt, Dct, and Wht for Compression of Ultrasonic Signals*. in *IEEE Ultrasonics Symposium, 2004*. 2004.
- [191] L. J. Cunningham, et al., *The Detection of Flaws in Austenitic Welds Using the Decomposition of the Time-Reversal Operator*. Proceedings of the Royal Society

- A: Mathematical, Physical and Engineering Sciences, 2016. **472**(2188): p. 20150500.
- [192] R. Y. Chiao and H. Xiaohui, *Coded Excitation for Diagnostic Ultrasound: A System Developer's Perspective*. IEEE Transactions on Ultrasonics, Ferroelectrics, and Frequency Control, 2005. **52**(2): p. 160-170.
- [193] S. Zhou, et al. *Medical High-Frequency Ultrasound Imaging Using Golay-Coded Pulse Excitation*. in *2012 5th International Conference on BioMedical Engineering and Informatics*. 2012.
- [194] M. O'Donnell, *Coded Excitation System for Improving the Penetration of Real-Time Phased-Array Imaging Systems*. IEEE Transactions on Ultrasonics, Ferroelectrics and Frequency Control, 1992. **39**(3): p. 341-351.
- [195] D. Lines, et al. *Using Coded Excitation to Maintain Signal to Noise for Fmc+Tfm on Attenuating Materials*. in *IEEE International Ultrasonics Symposium*. 2019. IEEE.
- [196] J. A. Isla and F. B. Cegla, *Simultaneous Transmission and Reception On all Elements of an Array: Binary Code Excitation*. Proceedings of the Royal Society A: Mathematical, Physical and Engineering Sciences, 2019. **475**(2225): p. 20180831.
- [197] C. E. Cooke, *The Early History of Pulse Compression Radar-the History of Pulse Compression at Sperry Gyroscope Company*. IEEE Transactions on Aerospace and Electronic Systems, 1988. **24**(6): p. 825-833.
- [198] J.R. Klauder, et al., *The Theory and Design of Chirp Radars*. Bell Labs Technical Journal, 1960. **39**(4).
- [199] Y. Takeuchi, *An Investigation of a Spread Energy Method for Medical Ultrasound Systems: Part One: Theory and Investigation*. Ultrasonics, 1979. **17**(4): p. 175-182.
- [200] F. Lam and J. Szilard, *Pulse Compression Techniques in Ultrasonic Non-Destructive Testing*. Ultrasonics, 1976. **14**(3): p. 111-114.
- [201] T. H. Gan, et al., *The Use of Broadband Acoustic Transducers and Pulse-Compression Techniques for Air-Coupled Ultrasonic Imaging*. Ultrasonics, 2001. **39**(3): p. 181-194.
- [202] D. Hutchins, et al., *Coded Waveforms for Optimised Air-Coupled Ultrasonic Nondestructive Evaluation*. Ultrasonics, 2014. **54**(7): p. 1745-1759.
- [203] M. K. Rizwan, et al., *Ultrasonic Imaging of Thick Carbon Fiber Reinforced Polymers through Pulse-Compression-Based Phased Array*. Applied Sciences, 2021. **11**(4): p. 1508.
- [204] D. A. Hutchins, et al., *Ultrasonic Propagation in Highly Attenuating Insulation Materials*. Sensors, 2020. **20**(8): p. 2285.
- [205] J. Lin, et al., *Excitation Waveform Design for Lamb Wave Pulse Compression*. IEEE Transactions on Ultrasonics, Ferroelectrics, and Frequency Control, 2016. **63**(1): p. 165-177.
- [206] H. Malekmohammadi, et al., *Comparison of Optimisation Strategies for the Improvement of Depth Detection Capability of Pulse-Compression Thermography*. Quantitative InfraRed Thermography Journal, 2020. **17**(1): p. 26-39.

- [207] M. Pollakowski and H. Ermert, *Chirp Signal Matching and Signal Power Optimization in Pulse-Echo Mode Ultrasonic Nondestructive Testing*. IEEE Transactions on Ultrasonics, Ferroelectrics and Frequency Control, 1994. **41**(5): p. 655-659.
- [208] J. Mamou, et al., *Chirp-Coded Excitation Imaging with a High-Frequency Ultrasound Annular Array*. IEEE Trans Ultrason Ferroelectr Freq Control, 2008. **55**(2): p. 508-13.
- [209] Z. Fan, et al., *Convolution of Barker and Golay Codes for Low Voltage Ultrasonic Testing*. Technologies, 2019. **7**(4): p. 72.
- [210] I. Trots, *Mutually Orthogonal Golay Complementary Sequences in Synthetic Aperture Imaging Systems*. Archives of Acoustics, 2015. **40**(2): p. 283-289.
- [211] M. Golay, *Complementary Series*. IRE Transactions on Information Theory, 1961. **7**(2): p. 82-87.
- [212] X. Huang. *Complementary Properties of Hadamard Matrices*. 2006. IEEE.
- [213] O. Siljama, et al., *Automated Flaw Detection in Multi-Channel Phased Array Ultrasonic Data Using Machine Learning*. Journal of Nondestructive Evaluation, 2021. **40**(3).
- [214] F. Zhao and J. Luo, *Diverging Wave Compounding with Spatio-Temporal Encoding Using Orthogonal Golay Pairs for High Frame Rate Imaging*. Ultrasonics, 2018. **89**: p. 155-165.
- [215] D. I. A. Lines, et al., *Real-Time Full Matrix Capture + Total Focusing and Other Novel Imaging Options Using General Purpose Pc-Based Array Instrumentation*. Insight - Non-Destructive Testing and Condition Monitoring, 2012. **54**(2): p. 86-90.
- [216] P. Jeong, et al., *Performance Evaluation of the Golay Code Pulse Compression Technique*. Research in Nondestructive Evaluation, 1996. **8**(3): p. 125-147.
- [217] G. Hayward and Y. Gorfu, *A Digital Hardware Correlation System for Fast Ultrasonic Data Acquisition in Peak Power Limited Applications*. IEEE Transactions on Ultrasonics, Ferroelectrics and Frequency Control, 1988. **35**(6): p. 800-808.
- [218] F. Hamilton, et al., *Nonlinear Harmonic Distortion of Complementary Golay Codes*. Ultrasonic Imaging, 2023. **45**(1): p. 22-29.
- [219] M. Sutcliffe, et al., *Real-Time Full Matrix Capture for Ultrasonic Non-Destructive Testing with Acceleration of Post-Processing through Graphic Hardware*. NDT & E International, 2012. **51**: p. 16-23.
- [220] M. Njiki, et al. *A Multi-Fpga Implementation of Real-Time Reconstruction Using Total Focusing Method*. in *2013 IEEE International Conference on Cyber Technology in Automation, Control and Intelligent Systems*. 2013.
- [221] J. Vrana, et al., *Handbook of Nondestructive Evaluation 4.0*. 2022: Springer International Publishing.